Stability and Precision Positioning of Piezoelectric Stepper Systems

Scott Wilcox

A dissertation
submitted in partial fulfillment of the
requirements for the degree of

Doctor of Philosophy

University of Washington

2015

Reading Committee:

Santosh Devasia, Chair

Brian Fabien

Joseph Garbini

Kristi Morgansen, GSR

Program Authorized to Offer Degree:
Mechanical Engineering

University of Washington

Abstract

Stability and Precision Positioning of Piezoelectric Stepper Systems

Scott Wilcox

Chair of the Supervisory Committee:
Professor Santosh Devasia
Mechanical Engineering

This research addresses a fundamental problem using stick-slip devices, including steppers, in which the output velocity has oscillations induced by the stepping behavior. Stepper systems allow smaller actuators to achieve large ranges by making multiple steps with each step generating small motions. The main contribution of this research is to develop a new large-range high-precision stepper system capable of constant velocities (i.e., suppressed oscillations).

Towards this, a full analysis of a single actuator stepper system is presented with stability shown using a Poincaré map approach with extension to a discontinuous equation of motion. Further, experimental results show agreement with model predictions, however, it is also shown that the oscillations cannot be suppressed with a single actuator stepper. Thus, a new dual-actuator stepper system is needed.

The new stepper system uses two piezoelectric actuators to drive a motion stage. By creating a phase shift ϕ between the motion of the actuators, the new stepper system is capable of suppressing the oscillations found in the single actuator stepper system. The new stepper system also allows the capability to be driven in a single actuator mode (setting the phase shift $\phi = 0$). From experimental results, driving the actuators in dual mode (out-of-phase, $\phi \neq 0$) trajectories show $\approx 62\%$ suppression in oscillation size can be achieved when compared to the single (in-phase, $\phi = 0$) mode.

TABLE OF CONTENTS

LIST OF FIGURES

ACKNOWLEDGMENTS

The work done for this dissertation would not have been possible without all of the people surrounding me. Many thanks are offered to the staff in the Mechanical Engineering department for all of their help and assistance through all three of my degrees. I have had the opportunity to work with several faculty and staff during my time and would like to thank my committee members Professor Brian Fabien, Professor Joseph Garbini, and Professor Kristi Morgansen for their guidance as well as Professor Martin Berg and Bill Kuykendall for helping me over the years. I would like to thank the Mechanical Engineering Department and the National Science Foundation (CMMI 1000404, CMMI 1301452) for funding my research.

I would like to thank all of my current and previous lab mates over the last five years. This includes Dr. Jeff Yoo, Dr. Jiradech Kongthon, Nathan Banka, Jonathon Realmuto, Arom Boekfah, Brandon Smith, Mahdi Ashrafi, Rahul Warrier and Parker Owan. I would like to give an extra thank you to Arom Boekfah for helping me with the experimental work. Thank you to the undergrads that allowed me to supervise their research Cheryl Tan, Michael Ng, Kurt Stalsburg, and Alex Ching as I think I learned more through the process than they did.

My wife, Callie, has put up with every late night and long weekend in the lab, every assumption made in the research, and every presentation run-through and I can't thank her enough for being a constant motivator through harder times. Thank you to my family and friends for dealing with the busy schedules and supporting me through my work.

Finally, I would like to express how fortunate I have been to have Professor Santosh Devasia as my research advisor over the last six years. He has been a constant source of advice academically, professionally, and personally for which I cannot repay him. I only hope that I can pass on the lessons learned through him such that others can succeed.

DEDICATION

To my wife, Callie

Chapter 1

INTRODUCTION

This research addresses a fundamental problem using stick-slip devices, including steppers, in which the output velocity has oscillations induced by the stepping behavior. Stepper systems allow smaller actuators to achieve large ranges by making multiple steps with each step generating small motions. These systems are used widely in research and industry, but they all suffer from oscillations that occur at each step. The main contribution of this research is to develop a new large-range high-precision stepper system capable of constant velocities, i.e., suppressed oscillations. Development of a system that can achieve both will be a key enabling tool in both research advances and industrial applications.

1.1 Research Goal

The goal of this research is to develop a large-range high-precision stepper system to address a fundamental problem in the application of stepper systems, including stick-slip systems. The stepping behavior used in these systems (examples of these systems shown in Fig. 1.1) has the ability to generate large-range motions by using a sequence of small steps, however, it is this same stepping behavior that leads to unwanted oscillations in the system response at each step. In the case of inertial stick-slip systems, where a mass is quickly moved in one direction and slowly returned, there is a backlash effect that occurs during the rapid deformation [4]. In systems where clamping (such as inchworm mechanisms) and stepping are the motion generation techniques, each clamping and stepping cycle introduces oscillations into the system [3, 5].

To address this fundamental problem, a new stepper system is being designed such that, at steady-state, it can maintain a constant velocity of a motion stage. The stepper system uses a pair of actuators to generate opposing friction forces once the system reaches a steady-state condition.

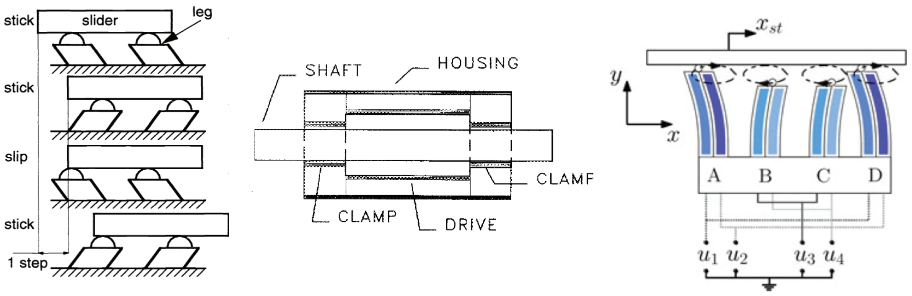

Figure 1.1: Types of stepper systems: (L to R) Inertial Mass Slider [1], Inchworm Actuator [2], PiezoLEGS Walking Actuator [3].

1.2 *What are the challenges?*

The main challenge in this research is to develop a stepper system that can overcome the oscillations found in previous systems.

1.2.1 Why are there oscillations?

In stepper systems, the overall motion is generally comprised of two motions. For example, in inertial mass sliders, the first motion is a slow "sticking" motion that pushes the mass forward and the second motion is a fast "slipping" motion that returns the actuator and ideally doesn't move the mass (See Fig. 1.2).

However, the friction forces are roughly proportional to the acceleration of the mass and therefore the rapid changes in acceleration lead to changes in the velocity leading to positioning errors showing up as oscillations. An example of this can be seen in Fig. 1.3.

1.2.2 How was this challenge is addressed

To address this challenge, a new stepper system was designed and tested. This new system makes use of two piezoelectric actuators to provide friction forces on a motion stage. A schematic of the new system can be seen in Fig. 1.4.

The trajectories that are followed by the actuator tips (where they make contact with

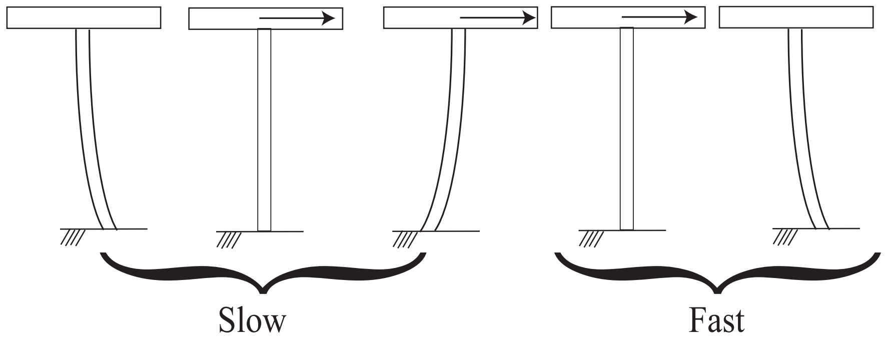

Figure 1.2: The basic operating principle of stick-slip systems. Slow motion pushes the system forward and fast motion returns the actuator to its starting position.

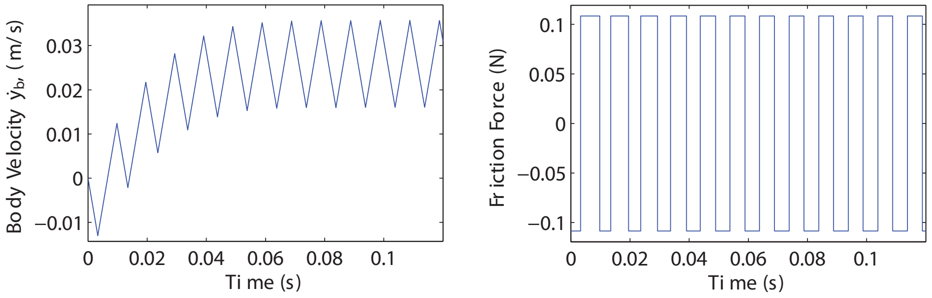

Figure 1.3: Simulation of stepping motion: velocity of stepper (left) friction forces generated (right). Note the oscillatory behavior of the velocity, these oscillations lead to positioning errors and are due to the switching behavior of the friction forces.

the motion stage) need to be designed such that they yield the desired steady state motion (i.e., a constant stage velocity). To achieve this, the friction forces must get the stage to the desired motion, then once at the desired motion, suppress the oscillations. This is done by generating trajectories that yield friction forces at each tip that oppose one another (as in Fig. 1.5).

The knowledge of the friction forces will also influence the design of the trajectories for the actuator tips. The acceleration of the actuator tips will determine whether or not

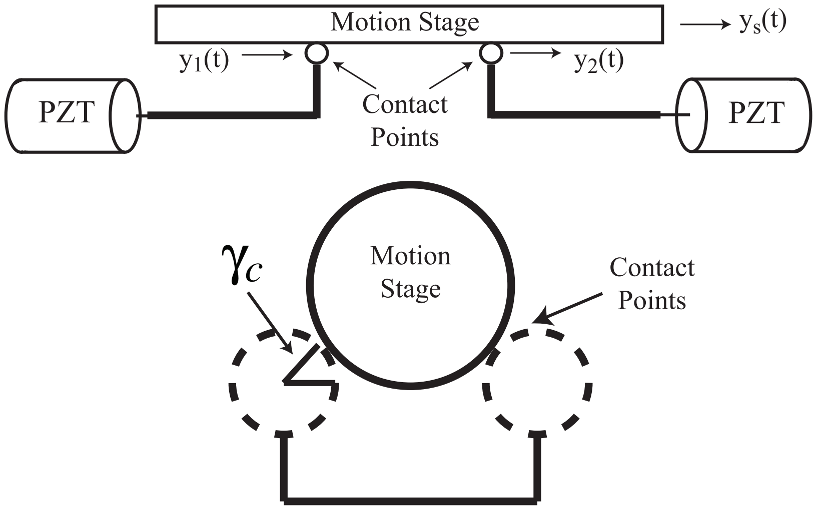

Figure 1.4: Stepper system design: The motion stage is free to move horizontally $y_s(t)$ while the piezoelectric actuators move horizontally $y_i(t)$ $(i = 1, 2)$ providing a friction force at the contact point with contact angle γ_c.

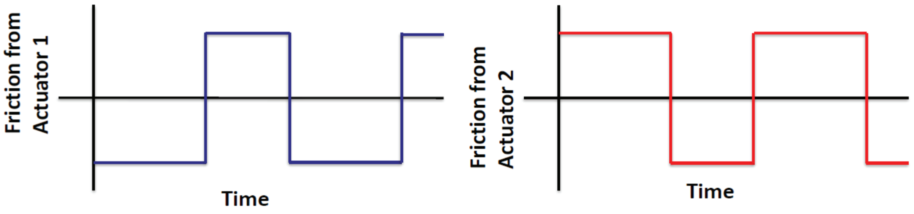

Figure 1.5: Desired friction forces at steady state. Note that they will cancel one another which will allow the oscillations generally found in stepper motion to be suppressed.

the static friction effects will contribute to the stage motion. Therefore, effects from static friction “sticking” can be reduced or removed from influencing the stage depending on the needs of the application.

1.2.3 Stability Issues

The desired motion of the stage can be generated using periodic inputs, so to investigate the stability of the system, a Poincaré map argument is used. However, due to the discontinuity of the friction dynamics, the Lipschitz condition cannot be enforced, which is needed, in general, for application of the Poincaré map [6, 7] to guarantee existence of a solution. To address this, further insight into the dynamics between map returns is needed to guarantee both existence of the solution and convergence to the desired steady state velocity.

1.3 What is the impact?

Stepper systems are used widely in both research and industry for many applications. In research, they are commonly used for positioning samples and tools in microscope applications and linear micro-manipulation [1, 4, 8–12], rotary manipulation [13–15], positioning in cryogenic environments [16, 17], and alignment of optical components [18, 19]. In industrial applications, there is a large market of companies developing stepping systems including Nanomotion, New Focus, Physik Instrumente, and Klocke Nanotechnik. Current technologies can reach sub-micron resolutions [1, 3, 12], but between point-to-point travel, the system has oscillations in the velocity thereby leading to loss of accuracy in the position. These devices are also very costly. According to a sales representative from Physik Instrumente, the NEXLINE® system, which uses periodically driven piezoelectric actuators to obtain nanometer and sub-nanometer resolutions, has a starting price at 15,000 USD as of 2013. Work done in [3] with a PiezoLEGS® system shows tracking errors of less than 200 nanometers when desiring a constant velocity using complicated control methods such as gain-scheduling and $\mathcal{H}_\infty$, but concedes that the stepping behavior induces the repetitive errors seen in experiments.

1.3.1 History and Applications

Beginning with the initial design in [20], steppers, such as those using stick-slip actuation, have been used to achieve high precision motion over a large range by using multiple small steps [13, 15, 21]. This large achievable range is an improvement over using single actuators for motion. For example, the range δ of a piezoelectric bimorph actuator is related to the actuator length L by

$$\delta = 3d_{31}\frac{L^2}{T^2}V \tag{1.1}$$

where d_{31} is a piezoelectric constant, T is the actuator thickness, and V is the voltage applied to the actuator [22]. With this relationship, the achievable range is still quite small. For an actuator of length $L \approx 30mm$, the range is only $\delta \approx 300\mu m$.

To improve upon the range of single actuator motions, in 1964, G.R. Stibitz proposed the incremental feed mechanism [20]. This design used a series of magnetostrictive elements to deform under a magnetic field and clamp on to a motor bar, move the motor bar, and release the motor bar. Since 1964, there have been a large range of designs building on this concept of using smart materials to turn multiple small steps into large motions.

The basic operating principle of these devices is to use two motions; in the case of stick-slip movement, the fast motion ”slips” across a surface follow by a slow motion ”sticking” on the surface. This allows the system to move in the direction of the slow motion. For stepping or inchworm systems, this is an in contact motion and a non-contact motion.

In the 1980’s, as technology increasingly got smaller, there was a need for high precision motion over larger ranges. This lead to a resurgence in stepper applications and research due to the steppers simple, easy, and reliable drive components [8].

In current stepper applications, typical control methods use variations in the amplitude and driving patterns of the actuators to calculate a feedforward input for the desired motion of system components (e.g. motion stages or image samples). Selection of these driving waveforms to achieve motion is an important issue in the wide variety of stepper designs such as inchworm-type steppers [23], walking-type motion [24–26], and underwater insectile steppers [27]. The research efforts on this issue have focused on the selection of these waveforms, which include standard time profiles such as sinusoidal, sawtooth, and square waves [27]. Additionally, the driving waveform can be optimized [26] to minimize the slip between the actuators and the motion stage.

1.3.2 Piezoelectric Actuators

Typical actuators used in stepper and stick-slip systems are made of piezoelectric materials, generally Lead-Zircon-Titanate (PZT). These materials exhibit the piezoelectric effect discovered in 1880 by the Curie brothers, Pierre and Jacques [28]. The direct piezoelectric effect is the resulting electric polarization due to an applied stress. The converse piezoelectric effect (the effect exploited in this research) is the strain produced in the material due to the presence of an electric field.

Piezoelectric actuators come in many configurations. Common actuator types are stacks, bimorphs, plates, and tubes (see Fig. 1.6). For steppers, stacks [1,24] and bimorphs [15,29] are commonly utilized.

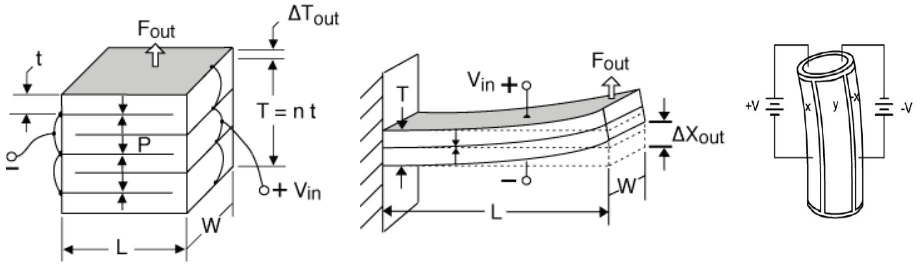

Figure 1.6: Common piezoelectric actuators: (L to R) stack (Piezo Systems Inc.), bimorph (Piezo Systems Inc.), and tube (Park Systems).

1.3.3 Example of need for large-range and high-precision

In scanning probe microscopy (SPM), the ability to achieve high-precision is well known [30]. However, the achievable range is limited by the size of the actuator chosen (commonly piezoelectric tube actuators [31]). To increase the range, longer actuators can be used. However, this leads to lower first-resonance frequencies [30] as the first resonance frequency ω_1 is related to the range R by

$$\omega_1 = 0.8 d_{31} \frac{v_{max}}{hR} \sqrt{\frac{E}{\rho}[1 + (1 - 2h/D)^2]}. \tag{1.2}$$

Therefore, there is a tradeoff between the available scanning range and the scan frequency as these scanners are generally limited to 1/10th or below the first resonance frequency to limit errors. By using a stepper system in place of the piezoelectric tube, the range can be increased (theoretically infinite) while maintaining the high precision motion of smaller actuators.

1.3.4 Broader Impacts

Using vibrations to generate motions is a technique used in many other systems such as hoppers for agriculture [32], sorting operations [33], camera lenses [34], and toys such as the Hex Bug ®. Advances made with the research discussed here have the ability to span these varied applications; from nanopositioning to agriculture to entertainment.

1.4 Research Path and Dissertation Structure

The research discussed here has been broken up into three main parts :

1. Research into the stability and control of a single actuator stepper model. This work showed the modeling of a single actuator stepper system with control inputs generated using feedforward methods. The resulting motion was then shown to be stable by extension of the Poincaré map approach to the discontinuous right hand side of the equation of motion. Experimental results are shown to agree with expected values from simulations. This work was accepted to the IEEE Transactions on Mechatronics to be published in April 2015 [29]. The article is contained in Chapter 2.

2. With the oscillations found in [29], a new system was needed to reduce the oscillations. This led to the two actuator stepper system. The theory for the two actuator stepper model was developed and shown to be stable. Control inputs are generated using feedforward methods and the stability is shown using a Poincaré map argument similar to [29]. This work was published in [35] and was awarded Best Student Paper. The article is contained in Chapter 3.

3. To address the theory from [35], a two-piezo positioning system was designed and experiments were performed using the out-of-phase inputs (as in [35]) as well as in-phase inputs (similar to work in [29]). This work is contained in Chapter 4.

The conclusions of the work presented are in Chapter 5 and the Appendices contain all of the MATLAB code, LabVIEW VI's, design processes for the stepper system, and optimal inverse plots.

Chapter 2

STABILITY AND VELOCITY CONTROL FOR A PIEZOELECTRIC STEPPER

2.1 Introduction

This article studies the velocity-control and stability of a large-range, piezoelectrically-actuated (piezo) stepper. Beginning with the initial design in [20], steppers such as those using stick-slip actuation have been used to achieve high precision over a relatively-large range by making multiple steps [13,15,21] in applications such as scanning probe microscopy [2,36] and alignment of optical components [18, 19]. The main contribution of this article is to extend the Poincaré-map approach (that typically requires the dynamics to be Lipschitz continuous) for evaluating the stability of the stepper dynamics in the presence of Coulomb-friction nonlinearity, which has a jump discontinuity with velocity. Additionally, inversion of the stepper-dynamics model is used to find the piezo input needed to control the stepper velocity, and model-based predictions of the stepper-velocity variations with changes in the driving-waveform amplitude are evaluated using an experimental-stepper system. Such velocity-control methods can be integrated with feedback techniques to achieve position control — although, this is not studied in the current work.

Selection of the piezo motions (driving waveforms) is an important issue in stepper designs such as inchworm-type steppers [23], walking-type motion [24–26], and underwater insectile steppers [27]. Current research efforts have focused on the appropriate selection of these driving waveforms, which include standard time profiles such as sinusoidal, sawtooth, and square waves [27]. Additionally, the driving waveform can be optimized [26] to minimize the slip between the actuators and the motion stage. In contrast, the work presented here aims to use slip to generate the friction force that leads to the stepper motion. (Potential wear is reduced by using nylon spheres between the contact surfaces.) In addition to studying the effect of the driving waveform on the stability of the stepper velocity, the current work finds the piezo inputs to achieve the driving waveform by modeling and inverting the stepper dynamics. The resulting driving waveforms are then applied to an experimental system to evaluate the approach.

Friction nonlinearity makes it challenging to show that a time-periodic actuator-excitation (e.g., with one of the standard driving waveforms such as the sawtooth pattern with periodicity T) leads to a stable, periodic, stepper velocity. In this article, a Poincaré-map approach, e.g. [7], is used to evaluate the stability of the motion resulting from a periodic excitation. Note that the Poincaré-map approach can be used to predict stability of periodic solutions $x_p(t+T) = x_p(t)$ of a continuous-time, differential equation of the form $\dot{x} = f(x,t)$ where f is periodic in time t with period T, i.e., $f(x, t+T) = f(x,t)$. For example, the stability of a periodic solution $x_p(\cdot)$ can be related to the stability of the the initial condition $x_p(0)$ in the discrete-time Poincaré map $P : x(0) \rightarrow x(T)$ generated by the solutions $x(\cdot)$ of the continuous-time, differential equation over one time period $[0, T]$, e.g., see Theorem 71.1 in [7]. Such arguments tend to require the function f to be (Lipschitz) continuous in the state x, e.g. [6, 7]. However, Coulomb friction nonlinearity has a jump discontinuity with velocity and is, therefore, not continuous in the state x. The current article extends the use of the Poincaré-Map approach to evaluate the stability of the steady-state stepper velocity in the presence of such discontinuities in the stepper dynamics. Additionally, the rate of convergence to the steady state is numerically obtained to provide estimates of the stepper's settling-time.

The article begins with model development in Section II. The model is used to develop the control law and to analyze the stability of the stepper velocity in Section III. Section IV presents the experimental results and discussion. Conclusions are in Section V.

2.2 Stepper Model

This section describes the modeling of the system dynamics, and the estimation of the model parameters.

2.2.1 System Description

The stepper body (see Fig. 2.1) is constructed of a T-shaped panel with three (Lead-Zirconate-Titanate (PZT)) piezoelectric (piezo) bimorph actuators (Q220-A4-303YB from Piezo Systems Inc.) acting as legs for the system. In this design three legs were used, which is the minimal number needed to define the contact plane with the ground, and to avoid tipping over when stationary. Additional legs would over-constrain the contact problem between the legs and the ground plane, and therefore, would require substantial additional precision in the system assembly. The bending vibrations of the piezo change the direction of the friction force F at the contact with the ground through nylon spheres attached at the tip of each actuator as shown in Fig. 2.1. Furthermore, the overall stepper motion is constrained to move along a track in a single direction (y_b axis) — the only force along the direction of the stepper's motion is the friction force F, a third of which acts on each piezo as illustrated in Fig. 2.1.

The motion of the center of mass of the stepper, approximated as the position y_b of the T-shaped body where most of the mass is located, is given by

$$M_t \frac{d^2}{dt^2} y_b(t) = F(t). \tag{2.1}$$

The friction force depends on the velocity of the nylon spheres $\dot{y}_{ns}$ with respect to the stationary track. For example, if all the piezos act in the same manner, and if the nylon-sphere velocity $\dot{y}_{ns} \neq 0$, then the friction can be modeled as the standard coulomb friction

$$F(t) \;=\; -\,\mu_k M_t g \; sign\,[\dot{y}_{ns}(t)] \tag{2.2}$$

where μ_k is the kinetic-friction coefficient, and $g = 9.81 m/s^2$ is the gravitational constant.

If the nylon-sphere velocity is zero, $\dot{y}_{ns} = 0$, then the friction force F (2.1) will be the static friction

$$|F(t)| \leq \mu_s M_t g.$$

Note that the magnitude of the static friction force F adjusts to maintain the nylon-sphere velocity $\dot{y}_{ns}$ at zero, until the friction force F saturates at the static-friction limit $\mu_s M_t g$. The nylon-sphere velocity $\dot{y}_{ns}$ depends on both the velocity of the stepper body $\dot{y}_b$ and the rate of piezo-tip deflection $\dot{y}_p$ since the nylon-sphere motion y_{ns} is the sum of the stepper-body motion y_b and the piezo-tip deflection y_p (with respect to the stepper-body motion), i.e.,

$$y_{ns}(t) \;=\; y_b(t) + y_p(t). \tag{2.3}$$

Therefore, for the sticking case, maintaining a zero nylon-sphere velocity $\dot{y}_{ns} = 0$, requires the friction force F to maintain zero nylon-sphere acceleration

$$\frac{d}{dt} \dot{y}_{ns}(t) = 0 \tag{2.4}$$

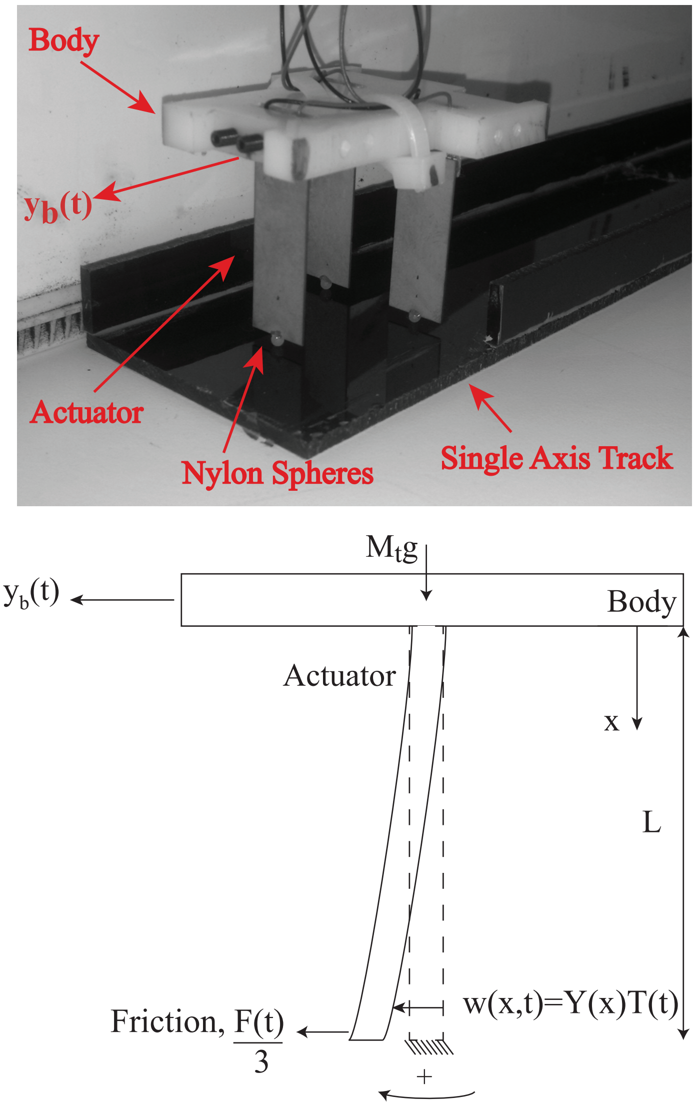

Figure 2.1: (Top) Piezo stepper: the stepper is comprised of three piezo actuators connected to a T-shaped body. The stepper motion is restricted to a single axis y_b along the track. (Bottom) Deflection of each piezo: the only force along the direction of the stepper's motion in the y_b direction is the friction force F, a third of which acts on each piezo.

or from (2.3)

$$\ddot{y}_b(t) = -\ddot{y}_p(t) \tag{2.5}$$

unless the friction force F saturates at $\pm\mu_s M_t g$. This leads to the following stepper-body dynamics (from (2.1, 2.5))

$$\begin{aligned} \frac{d}{dt}\dot{y}_b(t) &= -\mu_k g \; sign\left[\dot{y}_b(t) + \dot{y}_p(t)\right] \quad \text{if} \quad \dot{y}_{ns}(t) \neq 0 && (2.6)\\ &= -\frac{d}{dt}\dot{y}_p(t) \quad \text{if} \quad \left|\frac{d}{dt}\dot{y}_p(t)\right| < \mu_s g; \quad \dot{y}_{ns}(t) = 0 && (2.7)\\ &= -\mu_s g \; sign\left[\frac{d}{dt}\dot{y}_p(t)\right] \quad \text{otherwise.} && (2.8) \end{aligned}$$

where μ_s is the static-friction coefficient. Therefore, the stepper dynamics depends on the piezo-tip motion (y_p), which is modeled next.

2.2.2 Piezo-tip Deflection y_p Model

The piezo deflection is modeled as the bending $w(x,t)$ of a cantilever beam attached to the main body that is considered to be a lumped mass M_b. The net position $\tilde{y}(x,t)$ of a point x on the piezo-actuator (see Fig. 2.1) at time t is given by the sum of the main body motion $y_b(t)$ and the deflection $w(x,t)$ of the piezo-actuator, i.e.,

$$\tilde{y}(x,t) = w(x,t) + y_b(t). \tag{2.9}$$

Euler-Bernoulli beam

The piezo dynamics is modeled by the Euler-Bernoulli beam approach as, [37],

$$\rho A \frac{\partial^2 \tilde{y}}{\partial t^2} + EI \frac{\partial^4 \tilde{y}}{\partial x^4} = f(x,t) \tag{2.10}$$

where $f(x,t)$ represents external forcing. Additionally, the piezo parameters include the density ρ, the cross sectional area A, the elastic modulus E, and the moment of inertia I. The piezo deflection $w(x,t)$ can be separated into spatial $Y(x)$ and temporal $T(t)$ parts

$$w(x,t) = Y(x)T(t),$$

and the beam dynamics (3.4) can be rewritten (using (2.9)) as

$$\begin{aligned} \rho A \ddot{T}(t) Y(x) \; &+ EIT(t)\tfrac{\partial^4 Y}{\partial x^4}(x) \\ &= \; f(x,t) - \rho A \ddot{y}_b(t) \; = r(x,t). \end{aligned} \tag{2.11}$$

The homogeneous form of (2.11), obtained by setting $r(x,t) = 0$, can be separated into independent spatial and temporal equations

$$\frac{EI\frac{\partial^4 Y}{\partial x^4}(x)}{\rho A Y(x)} = \omega_n^2 \quad \text{and} \quad \frac{\ddot{T}(t)}{T(t)} = \ -\omega_n^2, \tag{2.12}$$

with the standard boundary conditions for a cantilever beam:

$$w(0,t) = 0;\ \frac{\partial w}{\partial x}(0,t) = 0;\ \frac{\partial^2 w}{\partial x^2}(L,t) = 0;\ \frac{\partial^3 w}{\partial x^3}(L,t) = 0,$$

where L is the piezo length. The resulting spatial solution of the n^{th} mode Y_n is given by [37]

$$Y_n(x) = sin(\beta_n x) - sinh(\beta_n x) + \sigma_n(cos(\beta_n x) - cosh(\beta_n x)), \tag{2.13}$$

where

$$\beta_n^4 = \frac{\omega_n^2 \rho A}{EI}, \qquad \sigma_n = \frac{sin(\beta_n L) + sinh(\beta_n L)}{cos(\beta_n L) + cosh(\beta_n L)}, \tag{2.14}$$

and for the first vibrational mode ($n = 1$) [37],

$$\beta_1 L = 1.875 \quad \text{and} \quad \sigma_1 = 0.7341.$$

spatial solution Y_n given by [37]. For the non-homogeneous case ($r(x,t) \neq 0$ in (2.11)), the general piezo deflection $w(x,t)$ can be considered to be a linear combination of these mode shapes, i.e.,

$$w(x,t) = \sum_1^\infty Y_n(x) T_n(t). \tag{2.15}$$

Dynamics of the First Vibrational Mode

Using the orthogonality of the mode shapes, the first mode dynamics ($n = 1$) can be extracted from (2.11) by: (i) substituting the piezo displacement $w(x,t)$ from (2.15); (ii) multiplying (2.11) with the first mode shape $Y_1(x)$; and (iii) integrating over the beam length, i.e.,

$$\begin{aligned}\sum_1^\infty \left[\int_0^L Y_1 Y_n \ddot{T}_n dx + \frac{EI}{\rho A}\int_0^L Y_1 \beta_n^4 Y_n T_n dx\right] \\ = \frac{1}{\rho A}\int_0^L Y_1(x) r(x,t) dx\end{aligned} \tag{2.16}$$

to yield

$$\ddot{T}_1 + \omega_1^2 T_1 = \frac{1}{\rho A}\frac{\int_0^L Y_1(x) r(x,t)dx}{\int_0^L Y_1(x) Y_1(x)dx}. \tag{2.17}$$

The external forcing term $f(x,t)$ in $r(x,t)$, (2.11), is given by

$$f(x,t) = M(t)\frac{\partial\delta(x-L)}{\partial x} + \frac{F(t)}{3}\delta(x-L) \tag{2.18}$$

where M is the applied moment due the voltage V acting on the piezo-actuator

$$M(t) \ = \frac{6d_{31}EI}{H^2}V(t) \ = K_{MV}V(t), \tag{2.19}$$

H is the thickness of the piezo-actuator, and d_{31} is a piezoelectric coefficient. Moreover, the external forcing term $f(x,t)$ includes a third of the total friction force F. Carrying out the integration of (2.17) and adding a damping term leads to

$$\ddot{T}_1 + 2\zeta_1\omega_1\dot{T}_1(t) + \omega_1^2 T_1 \ = K_1\ddot{y}_b(t) + K_2\frac{F(t)}{3} + K_3V(t) \tag{2.20}$$

where

$$\begin{aligned} K_1 &= -\frac{\int_0^L Y_1(x)dx}{\int_0^L Y_1^2(x)dx}, \qquad K_2 \ = \frac{Y_1(L)}{\rho A\int_0^L Y_1^2(x)dx}, \\ K_3 &= \frac{K_{MV}}{\rho A\int_0^L Y_1^2(x)dx}\left.\frac{\partial Y_1(x)}{\partial x}\right|_{x=L}, \end{aligned} \tag{2.21}$$

and ζ_1 is the damping ratio. With the one-vibrational-mode model, the piezo-tip deflection $y_p(t) = w(L,t)$ becomes (from 2.15)

$$y_p(t) = Y_1(L)T_1(t), \tag{2.22}$$

which can be substituted into (2.20) to obtain the piezo-tip dynamics

$$\begin{aligned} &\ddot{y}_p(t) + 2\zeta_1\omega_1\dot{y}_p(t) + \omega_1^2 y_p(t) = \\ &\qquad Y_1(L)\left[K_1\ddot{y}_b(t) + K_2\frac{F(t)}{3} + K_3V(t)\right]. \end{aligned} \tag{2.23}$$

The piezo-tip dynamics (2.23) and the stepper-body dynamics (2.6-2.8) represent the overall stepper model.

2.2.3 Model Parameters

The procedure to find parameters of the stepper model is described below, and the values are provided in Table 3.1.

Actuator Parameters

To estimate the parameters $[\ \zeta_1,\ \omega_1,\ Y_1(L),\ K_1,\ K_2,\ K_3]$ associated with vibrational dynamics in (2.23), the stepper was suspended above the track. With the actuators not in contact with the ground, the friction force is zero and the piezo body remains stationary, i.e., $F = 0$ and $\dot{y}_b = 0$. Then, the piezo dynamics reduces to (from (2.23))

$$\ddot{y}_p(t) + 2\zeta_1\omega_1\dot{y}_p(t) + \omega_1^2 y_p(t) = K_3 Y_1(L) V(t) \tag{2.24}$$

and the associated transfer function is

$$\begin{aligned} G(s) = \frac{y_p(s)}{V(s)} &= \frac{K_3 Y_1(L)}{s^2 + 2\zeta_1\omega_1 s + \omega_1^2} && (2.25) \\ &= \frac{K_{DC}\ \ \omega_1^2}{s^2 + 2\zeta_1\omega_1 s + \omega_1^2}, && (2.26) \end{aligned}$$

where K_{DC} is the dc gain of the actuator. A Kalman SMU-9000-15N inductive sensor was used to measure the piezo-tip deflection, for different sinusoidal inputs, generated using a Stanford Research Systems Digital Signal Analyzer. The resulting experimental frequency response is shown in Fig. 2.2. Although piezos have infinite modes of vibration, the frequency response plot in Fig. 2.2 suggests that the experimental frequency response can be modeled with a second order model up to 1kHz. The fitted model parameters ($\omega_1,\ \zeta,\ K_{DC}$) for one of the piezo actuators are shown in Table 3.1; effects of higher-order dynamics and variation of model parameters (between piezos) are not considered here for simplicity. The measured piezo dimensions (length L, width W, and thickness H) are provided in Table 3.1; the length L can be used to find the mode shape $Y_1(x)$ in (2.13) (with $n = 1$), to find parameters K_1 from (3.15) and K_3 from (2.25). Similarly K_2 (in (3.15)) is computed with cross-sectional area $A = HW$ and mass density ρ from [38].

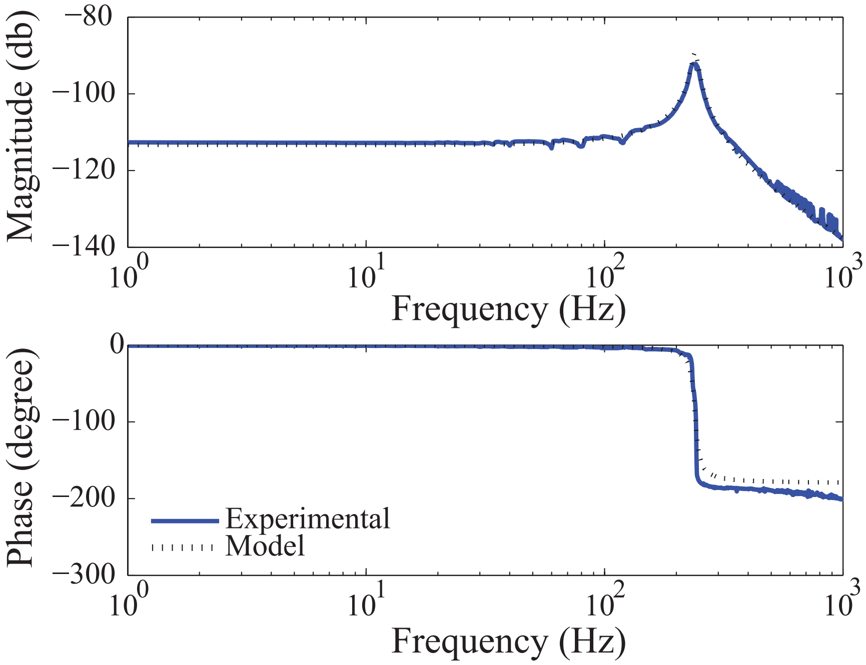

Figure 2.2: Experimental (solid line) and fitted (dotted line) frequency response. The experimental frequency response can be modeled with a second order model up to 1kHz.

Friction Parameters

The coefficients of kinetic friction μ_k and static friction μ_s in the stepper-body dynamics (2.6-2.8) were determined experimentally, and the system was weighed to find the total mass M_t.

To determine the coefficient of kinetic friction μ_k, a mass (rectangular block) with nylon spheres attached to its base was released down the acrylic track tilted at an angle θ as shown in Fig. 2.3. A video-recording was taken to find the position $z(t)$ of the mass along the track as a function of time t given by

$$z(t) = v_0 t + (1/2) a_s t^2 \tag{2.27}$$

where v_0 the initial velocity (at time $t = 0$) and the acceleration a_s along the slope were estimated by minimizing the least-square error between the fitted function (2.27) and the

Table 2.1: Values of Model Parameters

Variable	Value	Units
L	28.6	mm
W	12.7	mm
H	0.51	mm
ω_1	1501	rad/s
ζ	0.45	
K_{DC}	2.32	μm/V
ρ	7600	kg/m^3
K_1	-1.57	m^{-1}
K_2	2.8×10^3	1/Ns^2
K_3	5.2	rad/Vs
M_t	27.6	g
g	9.81	m/s^2
μ_k	0.4	
μ_s	0.62	

recorded motion data, e.g., as shown in Fig. 2.3. Since the acceleration along the slope is given by

$$a_s = g\left[\sin(\theta) - \mu_k \cos(\theta)\right], \tag{2.28}$$

the coefficient of kinetic friction μ_k can be computed from the estimated acceleration a_s as

$$\mu_k = \frac{[\sin(\theta) - a_s/g]}{\cos(\theta)}. \tag{2.29}$$

Similarly, the coefficient of static friction μ_s can be found by determining the largest angle $\theta = \theta^*$ at which the mass (rectangular block) does not slide, and then setting $a_s = 0$ in (2.29) to obtain

$$\mu_s = \tan(\theta^*). \tag{2.30}$$

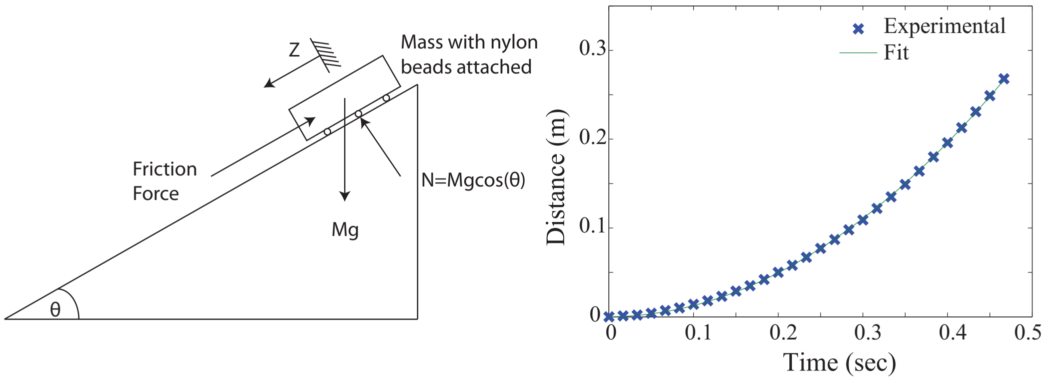

Figure 2.3: (Left) Set-up to estimate the coefficients of friction μ_k and μ_s. The mass (rectangular block) was released from rest at the top of the ramp and the position s along the ramp was measured using a high-speed camera. (Right) Comparison of the fitted mass-position (2.27) and experimental data.

2.3 *Stability of Steady-State Stepper Motion*

The design of the piezo motion (driving waveforms), the piezo input needed to achieve the driving waveform, and the stability of the resulting steady-state stepper motion are studied in this section.

2.3.1 Driving Waveform

The net impulse on the stepper in each period (of a periodic driving waveform) depends on the direction of the friction force. Therefore, modification of the time intervals for which the friction force is positive or negative in each period can be used to adjust the stepper velocity. Note that the piezo-tip velocity $\dot{y}_p$ affects the direction of the friction force F. For example, if the stepper-body velocity is zero ($\dot{y}_b = 0$), then from (2.2,2.3), the friction force F is positive ($F = \mu_k M_t g > 0$) when the piezo-tip velocity is negative ($\dot{y}_p < 0$), and the friction force F is negative ($F = -\mu_k M_t g < 0$) when the piezo-tip velocity $\dot{y}$ is positive ($\dot{y}_p > 0$). Therefore, the lengths of the time intervals during which the piezo-tip velocity $\dot{y}_p$ remains positive or negative (e.g., time-interval lengths t_n and t_p for an example velocity profile in Fig. 2.4) can be adjusted to generate a net impulse to drive the stepper in a specified direction.

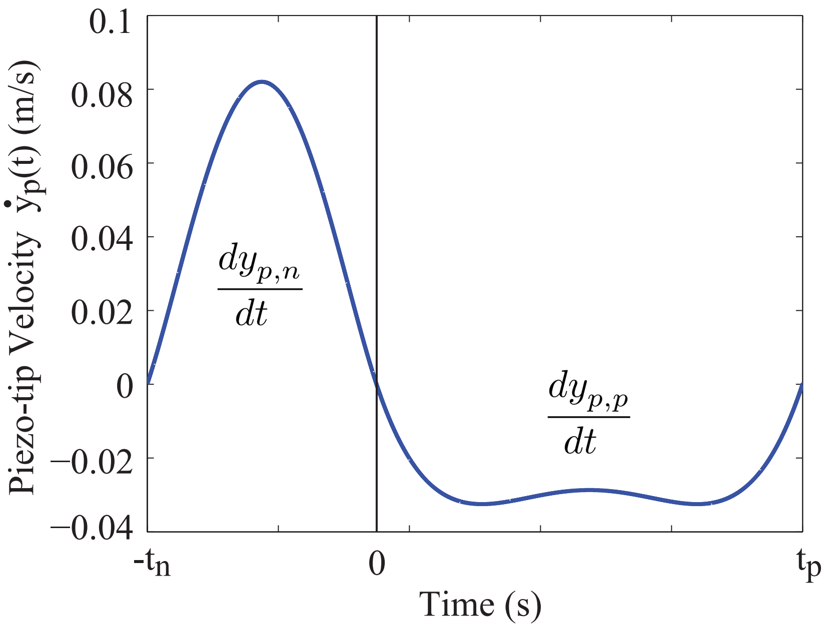

Figure 2.4: Example piezo-tip velocity $\dot{y}_p$, which is positive over the time interval $(-t_n, 0)$ and negative over the time interval $(0, t_p)$.

If the desired piezo-tip deflection y_p is increasing over time interval $(-t_n, 0)$ and decreasing over time interval $(0, t_p)$, then the piezo-tip velocity is positive and negative over these time intervals, which in turn, affects the impulse generated by the friction force over one time period $t_n + t_p$. In this study, the driving waveform (piezo-tip deflection y_p) is chosen as two polynomials

$$\begin{aligned} y_p(t) &= y_{p,p}(t) \quad \forall t \in [0, t_p] \\ y_p(t) &= y_{p,n}(t) \quad \forall t \in [-t_n, 0] \end{aligned}$$

where both are fifth order polynomials to maintain continuity conditions on the position, velocity, acceleration, and jerk, i.e.,

$$\begin{aligned} y_{p,p}(t) &= a_p t^5 + b_p t^4 + c_p t^3 + d_p t^2 + e_p t + f_p \\ y_{p,n}(t) &= a_n t^5 + b_n t^4 + c_n t^3 + d_n t^2 + e_n t + f_n. \end{aligned} \tag{2.31}$$

The coefficients are found by applying the following four continuity conditions on the piezo-tip deflections

$$\begin{aligned} y_{p,n}(-t_n) &= y_{p,p}(t_p) &= -y_{p,max}/2 \\ y_{p,n}(0) &= y_{p,p}(0) &= +y_{p,max}/2 \end{aligned} \tag{2.32}$$

where $y_{p,max}$ is the maximum deflection of the piezo, and the following eight continuity conditions on the velocity, acceleration, and jerk, i.e.,

$$\begin{aligned} \tfrac{dy_{p,n}}{dt}(0) &= \tfrac{dy_{p,p}}{dt}(0) &= 0 \\ \tfrac{dy_{p,n}}{dt}(-t_n) &= \tfrac{dy_{p,p}}{dt}(t_p) &= 0 \\ \tfrac{dy^k_{p,n}}{dt^k}(0) &= \tfrac{dy^k_{p,p}}{dt^k}(0) &\quad k = 2,3 \\ \tfrac{dy^k_{p,n}}{dt^k}(-t_n) &= \tfrac{dy^k_{p,p}}{dt^k}(t_p) &\quad k = 2,3. \end{aligned} \tag{2.33}$$

These twelve equations (3.18,2.33) can be solved to find the parameters of the two fifth-order polynomials (2.31) for the driving waveform.

An example, 100Hz driving waveform y_p is shown in Fig. 2.5, where the positive and negative time-interval lengths t_p, t_n are chosen to be approximately two to one, i.e., $t_p =$ 0.0065s and $t_n = 0.0035$s, and satisfying the condition that the driving frequency f_{dw} is given by

$$f_{dw} = 1/(t_n + t_p) = 100Hz. \tag{2.34}$$

The maximum displacement of the piezo is $y_{p,max} = 200\mu m$ for this example driving waveform. Note that this example driving waveform can be scaled by a constant while retaining the same time interval over which the velocity $\dot{y}_p$ is positive, and similarly maintain the time-interval over which the velocity $\dot{y}_p$ is negative.

2.3.2 Stepper-body Motion

The resulting stepper velocity for a given driving waveform y_p, and the stability of the steady-state stepper velocity are analyzed in this section. For example, the stepper velocity resulting from the driving waveform in Fig. 2.5, obtained by simulating the stepper dynamics (2.6-2.8) with zero initial stepper-body velocity $\dot{y}_b(0) = 0$, is shown in Fig. 2.6. The stepper-body velocity $\dot{y}_b$ tends to oscillate at steady-state with the same frequency $f_{dw} = 100$Hz as that of the driving waveform y_p. An upper bound $\Delta_{max}(\dot{y}_b)$ for the maximum change in

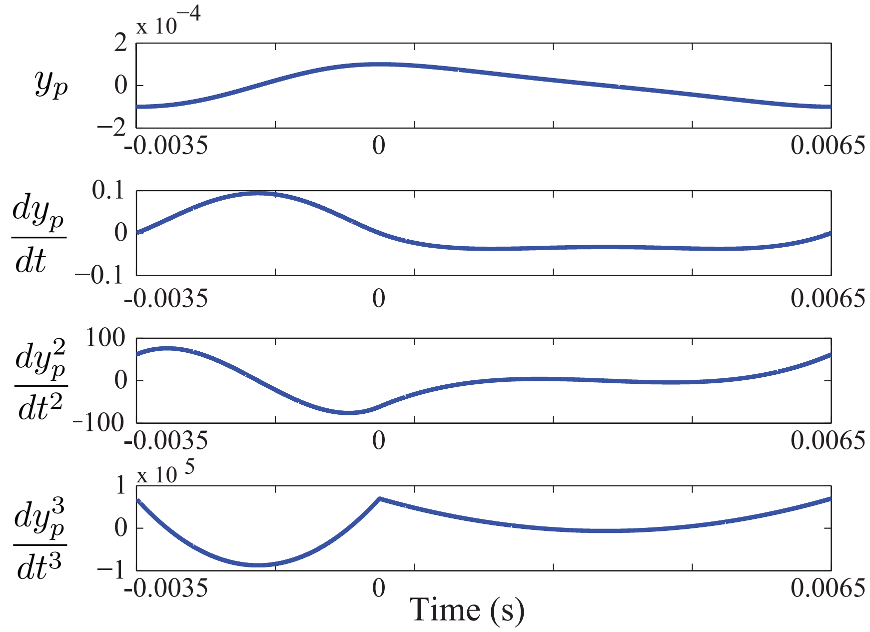

Figure 2.5: Example piezo trajectories: position y_p (driving waveform), velocity dy_p/dt, acceleration dy_p^2/dt^2, and jerk dy_p^3/dt^3 when the maximum actuator displacement is $y_{p,max} = 200\ \mu$m, and the positive and negative time-interval lengths t_p, t_n are chosen to be approximately two to one, i.e., $t_p = 0.0065$s and $t_n = 0.0035$s at frequency $f_{dw} = 100$Hz.

the stepper-body velocity in one period can be found, by equating the momentum change and the maximum impulse in any one direction (i.e., the product of the friction force and one half of the time period), as

$$\Delta_{max}(\dot{y}_b) = \frac{\mu_k g}{2 f_{dw}}. \tag{2.35}$$

2.3.3 Poincaré-Map-based Stability Analysis

To evaluate the stability of the steady-state stepper-body velocity $\dot{y}_b$, consider the Poincaré map P_{y_p} generated for a given piezo driving waveform y_p

$$P_{y_p} \ : X \rightarrow P_{y_p}\left[X\right] \tag{2.36}$$

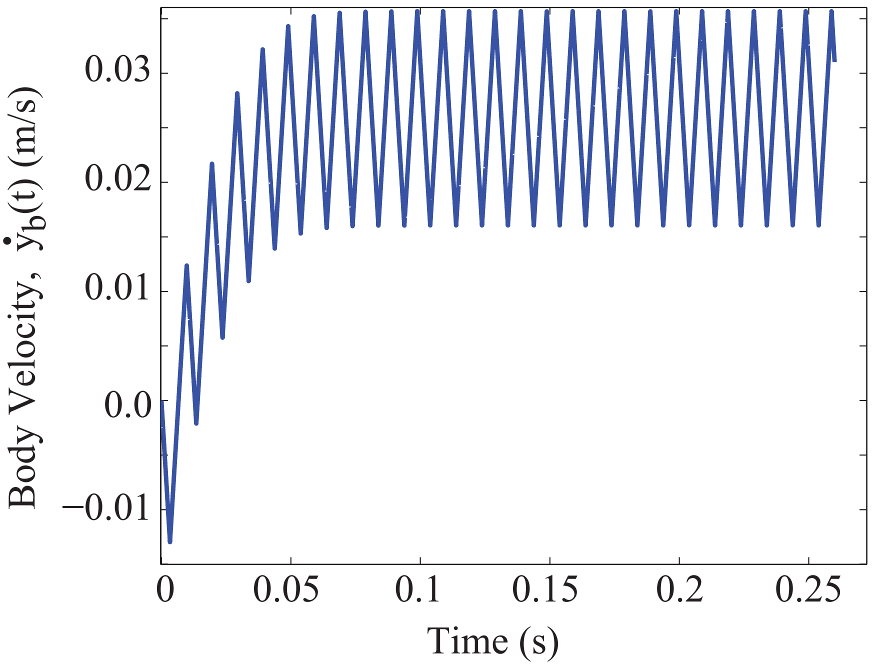

Figure 2.6: Stepper-body velocity $\dot{y}_b$ for the driving waveform y_p in Fig. 2.5 (with maximum actuator displacement $y_{p,max} = 200\ \mu$m) found by simulating the stepper dynamics (2.6-2.8) with zero initial conditions. The stepper-body velocity $\dot{y}_b$ tends to a steady-state oscillation with the same frequency $f_{dw} = 100$Hz as that of the driving waveform y_p.

obtained as the map of the stepper-body dynamics (2.6-2.8) over one time period $[-t_n, t_p]$, i.e.,

$$X = \dot{y}_b(-t_n); \qquad P_{y_p}[X] = \dot{y}_b(t_p), \tag{2.37}$$

as illustrated in Fig. 2.7 using numerical simulations for different initial conditions $\dot{y}_b(-t_n)$.

The resulting Poincaré map P_{y_p} is plotted in Fig. 2.8 — note that it has a fixed point at X^*. This fixed point X^* indicates that the stepper-body dynamics has the same initial and final states

$$X^* = \dot{y}_b(-t_n) = \dot{y}_b(t_p), \tag{2.38}$$

and a corresponding single-period steady-state solution which is shown in green (thick dashed line) in Fig. 2.7.

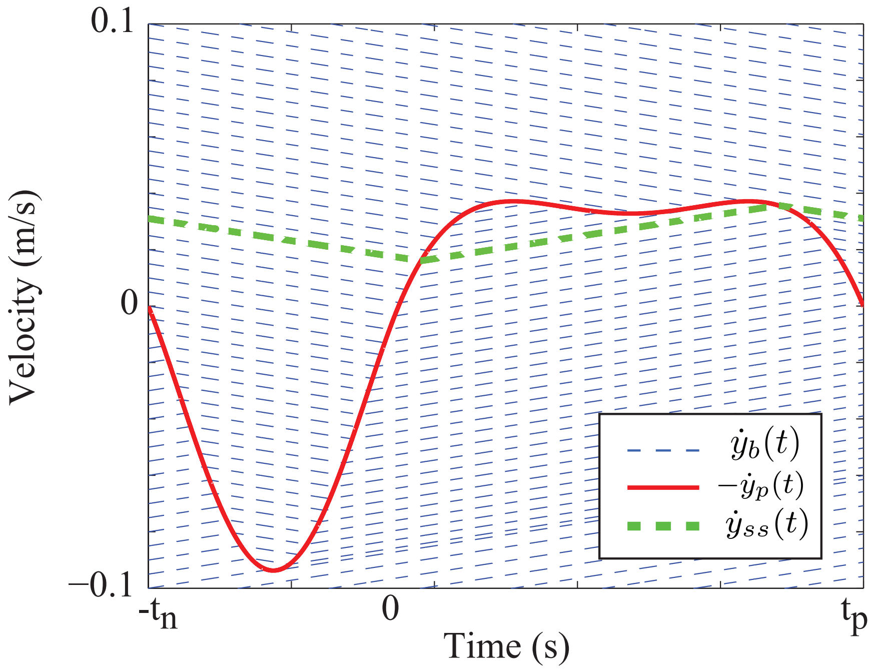

Figure 2.7: (Dashed lines) Stepper-body velocities $\dot{y}_b$ found by simulating the dynamics (2.6-2.8) over one time period $[-t_n, t_p]$ for the driving waveform y_p in Fig. 2.5 (with maximum actuator displacement $y_{p,max} = 200$ μm). The negative of the driving-waveform velocity $(-\dot{y}_p)$ is shown in red (dark solid line) and the steady-state solution of the stepper-body velocity $\dot{y}_{ss}$ with $\dot{y}_{ss}(-t_n) = \dot{y}_{ss}(t_p)$ is shown in green (thick dashed line). When the stepper body velocity $\dot{y}_b$ crosses the driving waveform velocity $(-\dot{y}_p = \dot{y}_b)$ the friction force F changes direction from (2.1), leading to a change in slope of the stepper-body velocity $\dot{y}_b$.

The following lemma shows that the fixed point X^* is stable in the sense that repeated application of the Poincaré map (i.e., application of multiple cycles of the driving waveform) will drive the system state (at the start each time period of the driving waveform) towards the fixed point X^*, i.e.,

$$P_{y_p}^{k}\left[X_1\right] \rightarrow X^* \qquad \text{as} \quad k \rightarrow \infty \tag{2.39}$$

for all initial states X_1 in a given region $[X_{min}, X_{max}]$.

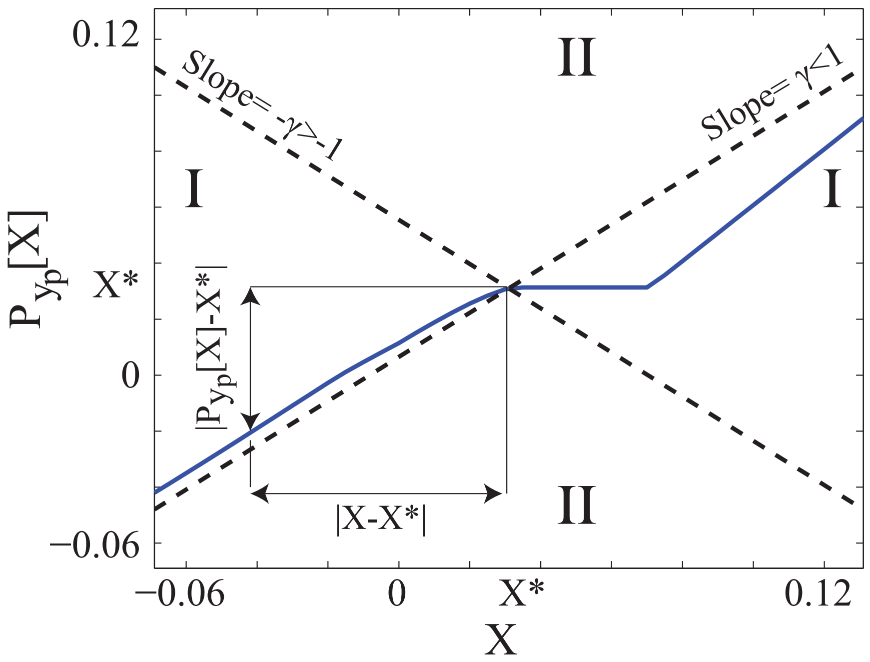

Figure 2.8: Numerical Poincaré map (solid), P_{y_p} associated with stepper-body dynamics (3.24) for the driving waveform y_p in Fig. 2.5 (with maximum actuator displacement $y_{p,max}$ = 200 μm). The dashed lines have slope $\pm\gamma$ (± 0.75) and pass through the fixed point X^*. If the map is contained in Region I, then stability is ensured by lemma 1.

Lemma 1 *The fixed point* X^* *of the Poincaré map* P_{y_p} *is stable if for* $X \in [X_{min}, X_{max}]$

$$\left|P_{y_p}[X] - X^*\right| \leq \gamma \left|X - X^*\right| \quad \textit{with} \;\; 0 \leq \gamma < 1 \tag{2.40}$$

and the fixed point X^* *is contained in the region, i.e.,* $X^* \in [X_{min}, X_{max}]$

Proof 1 *Repeated application of the Poincaré map* P_{y_p}*,*

$$X_{k+1} = P_{y_p}[X_k]$$

from an initial condition $X_1 \in [X_{min}, X_{max}]$ *leads to convergence towards the fixed point* *since*

$$\begin{aligned} |X_{k+1} - X^*| &= \left|P_{y_p}[X_k] - X^*\right| \\ &\leq \gamma\,|X_k - X^*| \\ &\leq \gamma^k\,|X_1 - X^*|\,. \end{aligned} \tag{2.41}$$

■

When the initial state X becomes large (relative to the driving waveform velocity), the stepper-body velocity changes along a straight line as seen in Fig. 2.7. Therefore, the difference between the initial state X and the $P_{y_p}[X]$ is a fixed value even if initial value X increases. Hence the slope of the Poincaré map P_{y_p} tends to a constant value (of one) as the initial value X increases to infinity, as seen in Fig. 2.8.

2.3.4 Convergence Analysis Over the Entire Time Period

Convergence to the fixed point X^* in the Poincaré map P_{y_p} implies that repeated application of the driving waveform will lead to convergence of the stepper-body velocity $\dot{y}_b$ at the beginning of each time period (of the nominal time interval $\mathcal{I} = [-t_n, t_p]$) to the equilibrium point X^*. In the following, it is shown that convergence at the beginning of each time period leads to convergence over the entire time interval. The analysis is split into two cases: (i) without sustained sticking; (ii) with sustained sticking.

Sustained Sticking Region

We begin by clarifying the region when sustained sticking (i.e., sticking over a non-zero-length time interval) can potentially occur for a given driving waveform. Sustained sticking occurs at time t if: (i) the nylon-sphere velocity $\dot{y}_{ns} = 0$ resulting in (from (2.3))

$$\dot{y}_b(t) = -\dot{y}_p(t), \qquad \ddot{y}_b(t) = -\ddot{y}_p(t); \tag{2.42}$$

and (ii) the static friction force is not saturated, i.e., (from (2.7))

$$|\ddot{y}_b(t)| \;=\; |\ddot{y}_p(t)| \;<\; \mu_s g. \tag{2.43}$$

Note that the first condition (2.42) depends on both, the stepper-body velocity $\dot{y}_b$ and the velocity of the driving waveform $\dot{y}_p$. However, the second saturation condition (2.43) only depends on the driving waveform velocity $\dot{y}_p$, and it can be used to define a set S (dependent on the driving waveform velocity $\dot{y}_p$ alone) where sustained sticking can potentially happen

$$S = \{t \in [-t_n, t_p] : |\ddot{y}_p(t)| < \mu_s g\}. \tag{2.44}$$

The set of such points is shown in Fig. 2.9 (bottom) for the driving waveform y_p with maximum piezo displacement $y_{p,max} = 125\mu m$. If the stepper-body velocity $\dot{y}_b$ intersects the negative of the driving-waveform velocity $-\dot{y}_p$ at a time instant t in the region S, then sustained sticking will occur (over a non-zero-length, time interval around the time instant t) since these velocities and accelerations are continuous functions in time and S is an open set. Therefore, the conditions for the sticking will be valid for a potentially small, but non-zero-length, time interval around the time instant t. A similar definition of the actual region for sustained sticking S^* that depends on both conditions is

$$S^* = \{t \in [-t_n, t_p] : |\ddot{y}_p(t)| < \mu_s g \;\text{ and }\; \dot{y}_b(t) = -\dot{y}_p(t)\} \tag{2.45}$$

and hence depends on the specific stepper-body velocity $\dot{y}_b$ (from the condition in (2.42)). The actual region of sustained sticking can be smaller than the potential set of sustained sticking S. For example, the actual sticking region S^* (for the steady-state stepper-body velocity $\dot{y}_{ss}$ corresponding to the driving waveform y_p with maximum piezo displacement $y_{p,max} = 125\mu m$) shown in Fig. 2.9 (top) is substantially smaller than the potential sticking region S.

If the maximum piezo displacement $y_{p,max}$ is large enough, the steady-state stepper body velocity $\dot{y}_{ss}$ never sticks during a time period $[-t_n, t_p]$. For example, if the maximum piezo displacement $y_{p,max} = 200\mu$m, then the steady-state stepper body velocity does not stick during each time period as shown in Fig. 2.10.

Convergence without Sustained Sticking

From the Poincaré map P_{y_p}, if the distance between a perturbed solution $\hat{\dot{y}}_b(\cdot)$ and the corresponding steady-state solution $\dot{y}_{ss}(\cdot)$ at time $-t_n$ (at the start of each time period) gets smaller over repeated applications of the driving waveform y_p, then the following analysis shows that the distance between the two nearby solutions gets smaller over the entire time

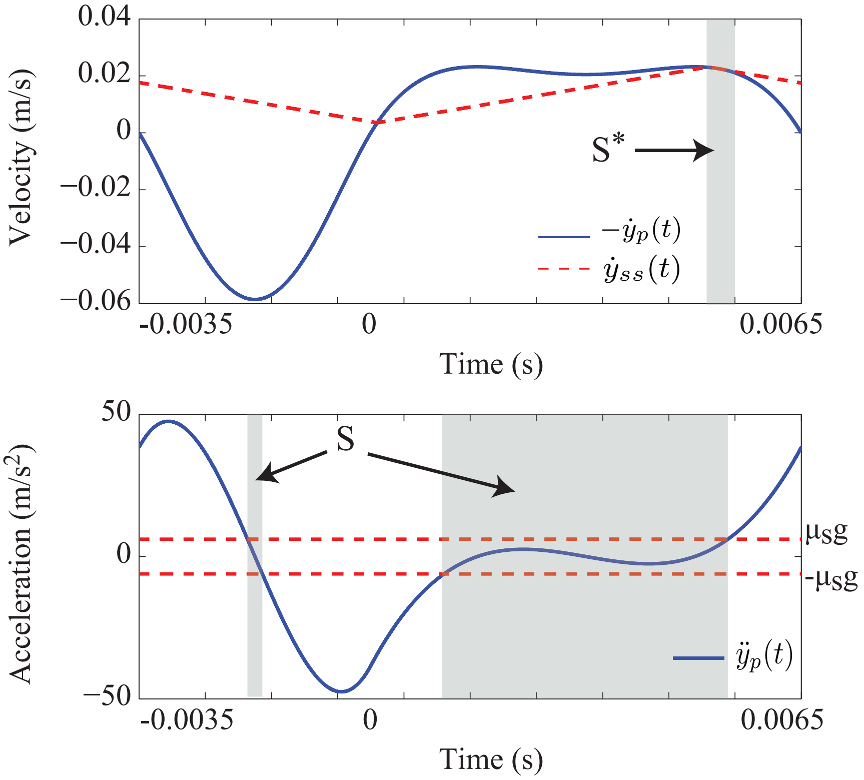

Figure 2.9: The potential S (2.44) and actual S^* (2.45) sustained sticking regions for the driving waveform y_p with maximum piezo displacement $y_{p,max} = 125\mu m$. If the velocity of the stepper-body velocity $\dot{y}_b$ intersects $-\dot{y}_p$ (shown in top plot) while the driving-waveform acceleration, $\ddot{y}_p$ (bottom plot) is less than $\mu_s g$, then the piezo stepper will have sustained sticking.

period $\mathcal{I} = [-t_n, t_p]$. This implies stability of the steady-state solution $\dot{y}_{ss}(\cdot)$ with repeated application of the driving waveform y_p.

Lemma 2 *Let the sticking points associated with the steady-state stepper-body velocity* $\dot{y}_{ss}$ *be finite in number,* N_i*,*

$$\{t_i\}_{i=1}^{i=N_i}, \quad t_i < t_{i+1}, \quad t_i \in (-t_n, t_p), \tag{2.46}$$

satisfying, from (2.3),

$$\dot{y}_{ss}(t_i) = -\dot{y}_p(t_i),$$

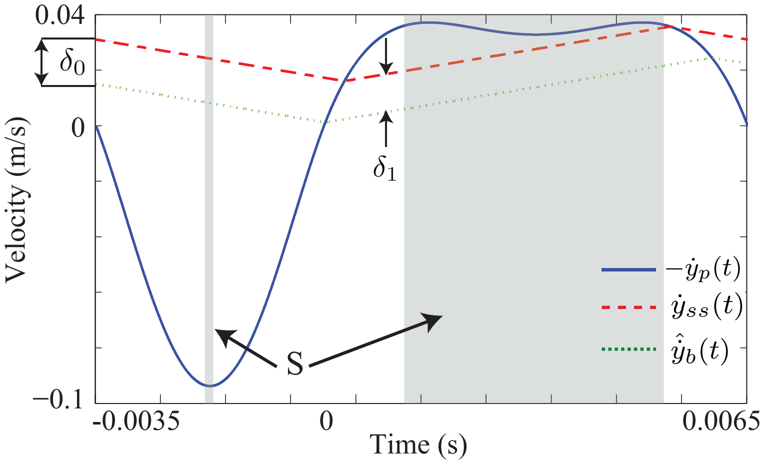

Figure 2.10: The distance δ_i between the perturbed stepper-body velocity $\hat{\dot{y}}_b$ and the steady-state solution $\dot{y}_{ss}$ reduces over the time period $\mathcal{I} = [-t_n, t_p]$ for the case without sustained sticking, and the driving waveform y_p in Fig. 2.5 (with maximum actuator displacement $y_{p,max} = 200$ μm).

and lie outside the closure $\bar{S}^*$ *of the actual sustained-sticking region* S^* *(2.45), i.e.,*

$$\{t_i\} \quad \notin \quad \bar{S}^* \tag{2.47}$$

where

$$\bar{S}^* = \{t \in [-t_n, t_p] \ : \ |\ddot{y}_p(t)| \leq \mu_s g, \quad \dot{y}_b(t) = -\dot{y}_p(t)\}. \tag{2.48}$$

Additionally, let the static friction coefficient μ_s *be larger than the kinetic friction coefficient* μ_k*, i.e.,* $\mu_s > \mu_k$*. Then, for each sticking-point* t_i *associated with the steady-state solution* $\dot{y}_{ss}$*, there exists a neighborhood* $\mathcal{N}_i(t_i, \Delta_i)$ *wherein perturbed solutions* $\hat{\dot{y}}_b(\cdot)$ *to the stepper-body velocity also have a unique non-sustained sticking point. Here, a neighborhood* $\mathcal{N}_i(\cdot, \cdot)$ *is defined as*

$$\mathcal{N}_i(a_1, a_2) = (a_1 - a_2, a_1 + a_2), \quad a_2 > 0. \tag{2.49}$$

Proof 2 *If sustained sticking is avoided at time instants* t_i*, then from the definition of sustained sticking point (2.45) and condition (2.47) of the lemma*

$$|\ddot{y}_p(t_i)| > \mu_s g. \tag{2.50}$$

Due to continuity of the driving waveform's acceleration $\ddot{y}_p$*, the above inequality condition (2.50) will be met in some local neighborhood* $\mathcal{N}_{i,1}(t_i, \Delta_{i,1})$ *of the time instant* t_i*.*

Away from a sticking point, the derivatives of the stepper-body velocity $\dot{y}_{ss}$ *can be determined from (2.2) as*

$$\ddot{y}_{ss}(t) = \begin{cases} \mu_k g & -\dot{y}_p(t) \ > \ \dot{y}_{ss}(t) \\ -\mu_k g & -\dot{y}_p(t) \ < \ \dot{y}_{ss}(t) \end{cases} \tag{2.51}$$

resulting in a linear equation in time (in a local neighborhood $\mathcal{N}_{i,2}(t_i, \Delta_{i,2})$*)*

$$\begin{aligned} \dot{y}_{ss}(t) &= [\ddot{y}_{ss}(t)]\,(t - t_i) + \dot{y}_{ss}(t_i) \\ &= [\ddot{y}_{ss}(t)]\,(t - t_i) - \dot{y}_p(t_i) \end{aligned} \tag{2.52}$$

where the sign of the acceleration $\ddot{y}_{ss}$ *can change only after a sticking point, e.g., as illustrated in Fig. 2.11 (left). Then the functions (representing the difference between the negative of the driving waveform velocity* $-\dot{y}_p$ *and the stepper-body velocity* $\dot{y}_{ss}$*)*

$$\begin{aligned} f_{i,p}(t) &= -\dot{y}_p(t) - \dot{y}_{ss}(t) \\ &= -\dot{y}_p(t) - \{[\ddot{y}_{ss}(t)]\,(t - t_i) - \dot{y}_p(t_i)\} \\ &= -\dot{y}_p(t) - \{[\mu_k g]\,(t - t_i) - \dot{y}_p(t_i)\} \\ \\ f_{i,n}(t) &= -\dot{y}_p(t) - \{[\ddot{y}_{ss}(t)]\,(t - t_i) - \dot{y}_p(t_i)\} \\ &= -\dot{y}_p(t) - \{[-\mu_k g]\,(t - t_i) - \dot{y}_p(t_i)\} \end{aligned} \tag{2.53}$$

with

$$f_{i,p}(t_i) = 0, \quad f_{i,n}(t_i) = 0 \tag{2.54}$$

are continuously differentiable in local neighborhoods $\mathcal{N}_{i,2}(t_i, \Delta_{i,p}), \mathcal{N}_{i,2}(t_i, \Delta_{i,n})$ *with nonzero time derivative at time* $t = t_i$

$$\begin{aligned} \tfrac{d}{dt} f_{i,p}(t_i) &= -\ddot{y}_p(t_i) - \mu_k g &\neq 0 \\ \tfrac{d}{dt} f_{i,n}(t_i) &= -\ddot{y}_p(t_i) + \mu_k g &\neq 0 \end{aligned} \tag{2.55}$$

from (2.50) since the static friction coefficient μ_s *is larger than the kinetic friction coefficient* μ_k*. Then, from the inverse function theorem (e.g., [39], Theorem 7.8), there exists a neighborhood*

$$\mathcal{N}_i(t_i, \Delta_i) \ \in \ \mathcal{N}_{i,1} \cap \mathcal{N}_{i,2} \tag{2.56}$$

as in (2.49), such that the functions $f_{i,p}, f_{i,n}$ *have unique inverse functions. In other words, for sufficiently small* δ *there are unique time instants* $t_p(\delta), t_n(\delta)$ *in the neighborhood* $\mathcal{N}_i(t_i, \Delta_i)$ *that satisfy*

$$f_{i,p}(t_p(\delta)) = \delta, \quad f_{i,n}(t_n(\delta)) = \delta. \tag{2.57}$$

This implies that there are unique intersections (in the neighborhood $\mathcal{N}_i(t_i, \Delta_i)$*) between the negative of the driving-waveform velocity* $-\dot{y}_p$ *and the straight lines that are offset by perpendicular distance* δ *from the steady-state stepper-body velocity* $\dot{y}_{ss}$ *given by (similar to (2.52))*

$$\begin{aligned} \dot{y}_{ss,i,p}(t) &= [\mu_k g]\,(t - t_i) + \dot{y}_{ss}(t_i) + \delta \\ \dot{y}_{ss,i,n}(t) &= [-\mu_k g]\,(t - t_i) + \dot{y}_{ss}(t_i) + \delta. \end{aligned} \tag{2.58}$$

The lemma follows since solutions to the stepper-body velocity (in the neighborhood $\mathcal{N}_i(t_i, \Delta_i)$*) are along one of these straight lines before intersecting (and similarly for the case after intersecting) with* $-\dot{y}_p$*, the negative of the driving-waveform velocity.* ■

Lemma 3 *Let conditions of lemma 2 be satisfied. Furthermore, let nearby solutions to the stepper-body dynamics not have sticking points other than in the neighborhood* $\mathcal{N}_i(t_i, \Delta_i)$ *around* t_i *(2.46) as in lemma 2. Formally, let the negative of the driving-wavefrom velocity* $-\dot{y}_p$ *be separated from the steady-state stepper-body velocity* $\dot{y}_{ss}$ *at time instants* t *that are away from the sticking points, i.e.,*

$$|-\dot{y}_p(t) - \dot{y}_{ss}(t)| \quad > \delta_{p,ss} \quad > 0 \tag{2.59}$$

for all time t *outside the neighborhoods* $\mathcal{N}_i(t_i, \Delta_i)$ *in lemma 2, i.e.,*

$$t \quad \in \mathcal{I}^* = [-t_n, t_p] \; - \bigcup_{i=1}^{N_i} \mathcal{N}_i(t_i, \Delta_i) \tag{2.60}$$

where without loss of generality, it is assumed that there is no sticking at the initial time $-t_n \in \mathcal{I}^*$ *since the initial time can be redefined to be a point without sticking. Moreover, let* $\hat{\dot{y}}_b(\cdot)$ *be a solution to the stepper-body velocity that is nearby the steady-state solution* $\dot{y}_{ss}(\cdot)$ *with an initial perturbation* δ_0 *at the beginning of the time interval (*$t = -t_n$*)*

$$\hat{\dot{y}}_b(-t_n) = \dot{y}_{ss}(-t_n) + \delta_0. \tag{2.61}$$

Then, the difference between the perturbed solution $\hat{\dot{y}}_b$ *and steady-state body velocity* $\dot{y}_{ss}$ *cannot increase with time, i.e., for all* $t_a, t_b \in \mathcal{I}$,

$$|\dot{y}_{ss}(t_a) - \hat{\dot{y}}_b(t_a)| \leq |\dot{y}_{ss}(t_b) - \hat{\dot{y}}_b(t_b)| \quad \textit{if} \;\; t_b < t_a \tag{2.62}$$

provided the initial perturbation δ_0 *is sufficiently small.*

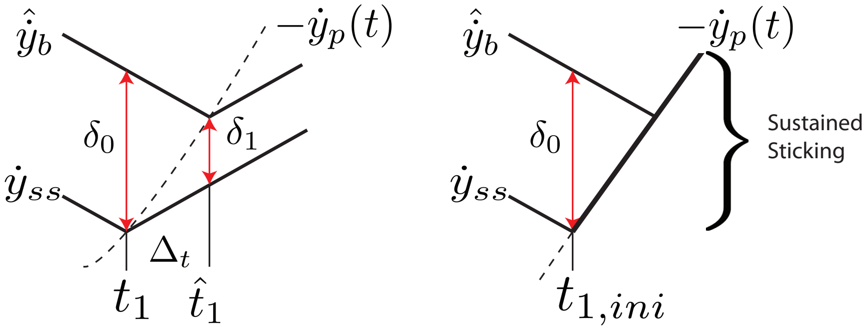

Figure 2.11: Left: Reduction of distance between a perturbed velocity, $\hat{\dot{y}}_b$, and the steady-state solution, $\dot{y}_{ss}$ after the first sticking point t_i. The intersection with the negative driving-waveform velocity $-\dot{y}_p$ and the stepper-body velocities ($\dot{y}_{ss}$ or $\hat{\dot{y}}_b$) causes a sign change in their derivatives following (2.51) and (2.63). Right: Sustained sticking occurs at the first sticking point $t_{1,ini} \in S$.

Proof 3 *For sufficiently small initial perturbation* $\delta_0 < \delta$ *as in (2.57), from lemma 2 there is a unique non-sustained sticking point* $\hat{t}_i$ *for the perturbed velocity* $\hat{\dot{y}}_b$ *in each neighborhood* $\mathcal{N}_i(t_i, \Delta_i)$ *around the sticking points* t_i *of the steady-state solution,* $\dot{y}_{ss}$. *Furthermore, the perturbed velocity* $\hat{\dot{y}}_b$ *and the steady-state velocity* $\dot{y}_{ss}$ *are parallel while they are on the same side (above or below) the negative of the driving-waveform velocity* $-\dot{y}_p$ *as illustrated in Fig. 2.11. Due to the dynamics in (2.2), the perturbed velocity* $\hat{\dot{y}}_b$ *dynamics are similar to the steady-state velocity* $\dot{y}_{ss}$ *dynamics (2.51)*

$$\hat{\ddot{y}}_b(t) = \begin{cases} \mu_k g & -\dot{y}_p(t) \;>\; \hat{\dot{y}}_b(t) \\ -\mu_k g & -\dot{y}_p(t) \;<\; \hat{\dot{y}}_b(t). \end{cases} \tag{2.63}$$

Consider the first intersection t_1 *with* $\delta_0 > 0$*, where* $t_1, \hat{t}_1$ *satisfy (due to sticking condition (2.42))*

$$\begin{aligned} -\dot{y}_p(t_1) &= \dot{y}_{ss}(t_1) \\ -\dot{y}_p(\hat{t}_1) &= \dot{\hat{y}}_b(\hat{t}_1) \end{aligned} \tag{2.64}$$

and

$$\Delta_t = \hat{t}_1 - t_1.$$

Furthermore, consider the case when stepper-body velocities ($\dot{y}_{ss}$, $\dot{\hat{y}}_b$) *are above the negative of the driving-waveform velocity* $-\dot{y}_p(t)$ *before the first sticking point*

$$\begin{aligned} -\dot{y}_p(t) &< \dot{y}_{ss}(t) \quad \mathit{for} \;\; t < t_1 \\ -\dot{y}_p(t) &< \dot{\hat{y}}_b(t) \quad \mathit{for} \;\; t < \hat{t}_1. \end{aligned} \tag{2.65}$$

Note that the condition in (2.65) implies that the stepper-body accelerations ($\ddot{y}_{ss}$, $\ddot{\hat{y}}_b$) *are negative from (2.51, 2.63). Moreover, the positive initial perturbation* $\delta_0 > 0$ *implies that the sticking point of the perturbed solution occurs later, i.e.,* $\Delta_t > 0$ *or* $\hat{t}_1 > t_1$*. The difference between the two solutions can be found as, from (2.61, 2.64)*

$$\begin{aligned} \delta_0 &= \dot{\hat{y}}_b(t_1) - \dot{y}_{ss}(t_1) \\ \delta_1 &= \dot{\hat{y}}_b(\hat{t}_1) - \dot{y}_{ss}(\hat{t}_1). \end{aligned} \tag{2.66}$$

From linearity of the stepper-body velocities with time (due to constant accelerations (2.51,2.63)) the velocities $\dot{\hat{y}}_b(t_1)$ *and* $\dot{y}_{ss}(t_2)$ *can be obtained as*

$$\begin{aligned} \dot{\hat{y}}_b(t_1) &= -\dot{y}_p(\hat{t}_1) + \mu_k g \Delta_t \\ \dot{y}_{ss}(\hat{t}_1) &= -\dot{y}_p(t_1) + \mu_k g \Delta_t \end{aligned} \tag{2.67}$$

Substituting (2.67) into (2.66) and using (2.64) yields

$$\begin{aligned} \delta_0 &= -\dot{y}_p(\hat{t}_1) + \dot{y}_p(t_1) + \mu_k g \Delta_t \\ \delta_1 &= -\dot{y}_p(\hat{t}_1) + \dot{y}_p(t_1) - \mu_k g \Delta_t, \end{aligned} \tag{2.68}$$

which then yields

$$\delta_0 - \delta_1 = 2\mu_k g \Delta_t > 0. \tag{2.69}$$

Thus, the separation between the perturbed solution and the steady-state solution decreases after passing through non-sustained sticking points. Mainly, this occurs since the steady-state *velocity $\dot{y}_{ss}$ has a positive slope while the perturbed velocity $\dot{\hat{y}}_b$ has a negative slope between the sticking points t_1 and $\hat{t}_1$, i.e., the distance between the two velocities is decreasing during the time interval $(t_1, \hat{t}_1)$ such that for any $t_1 < t^* < \hat{t}_1$*

$$\dot{\hat{y}}_b(\hat{t}_1) - \dot{y}_{ss}(\hat{t}_1) < \dot{\hat{y}}_b(t^*) - \dot{y}_{ss}(t^*) < \dot{\hat{y}}_b(t_1) - \dot{y}_{ss}(t_1). \tag{2.70}$$

The lemma's claim for negative initial perturbation $\delta_0 < 0$ follows by switching the two velocities $\dot{\hat{y}}_b$ and $\dot{y}_{ss}$ in the above arguments. The argument for the case when the stepper-body velocities ($\dot{\hat{y}}_b$ and $\dot{y}_{ss}$) are below the negative of the driving-waveform velocity $-\dot{y}_p$ also follows from similar arguments. Additionally, the argument can be repeated at other sticking points $t_i, \hat{t}_i$.

Note that there are no other sticking points (other than $\hat{t}_i \in S$) for the perturbed velocity $\dot{\hat{y}}_b$ if the initial difference δ_0 is sufficiently small, i.e., from (2.50)

$$\delta_0 < \delta_{p,ss},$$

which ensures that the the perturbed velocity $\dot{\hat{y}}_b$ will remain sufficiently close to the steady-state velocity $\dot{y}_{ss}$ to avoid the necessary condition for sticking, i.e.,

$$\dot{\hat{y}}_b(t) = -\dot{y}_p(t)$$

for any time $t \in \mathcal{I}^*$ (2.60). ■

Convergence with Sustained Sticking

For the sustained sticking case, a similar result can be shown (as in lemma 3) since sustained sticking to the same (negative) driving-waveform velocity profile $-\dot{y}_p$ ensures convergence after sticking, as shown below.

Lemma 4 *Let the closure $\bar{S}^*$ (2.48) of actual sustained-sticking region S^* (2.45) be a union of ordered, disjoint time intervals, i.e.,*

$$\mathcal{I}_{S^*} = \bigcup_{i}^{N_{i,s}} [t_{i,ini}, t_{i,fin}], \quad t_{i,ini} < t_{i,fin} < t_{i+1,ini}. \tag{2.71}$$

Moreover, let the initial points $t_{i,ini}$ *of each time interval in* $\mathcal{I}_{S^*}$ *lie inside the open set of potential sticking points* S *(2.44)*

$$t_{i,ini} \in S. \tag{2.72}$$

Finally, let the absolute value of the time derivative of the driving-waveform velocity satisfy in some local neighborhood of $t_{i,ini}$

$$|\ddot{y}_p(t_{i,ini})| \quad \neq \quad \mu_k g \quad . \tag{2.73}$$

Then, for each initial sustained-sticking-point $t_{i,ini}$ *associated with the steady-state solution* $\dot{y}_{ss}$*, there exists a neighborhood* $\mathcal{N}_i(t_{i,ini}, \Delta_{i,ini})$ *wherein a perturbed solutions* $\hat{\dot{y}}_b(\cdot)$ *(as in lemma 2) to the steady-state stepper-body velocity will have a unique sustained sticking point.*

Proof 4 *This follows from the inverse-function theorem with arguments similar to the proof of lemma 2 since the time derivatives (2.55) of the difference functions (2.53), with* t_i *replaced by* $t_{i,ini}$*, will be non-zero at the initial points* $t_{i,ini}$*. The details are not repeated for brevity.* ■

Lemma 5 *Let conditions of lemma 2 apply to all non-sustained sticking points of the steady-state stepper-body velocity* $\dot{y}_{ss}$*. Furthermore, as in lemma 3, let the negative of the driving-wavefrom velocity* $-\dot{y}_p$ *be separated from the steady-state stepper-body velocity* $\dot{y}_{ss}$ *at time instants* t *that are away from the non-sustained sticking points and initial time instants of the sustained-sticking instants (2.72), i.e.,*

$$| - \dot{y}_p(t) - \dot{y}_{ss}(t)| > \delta^*_{p,ss} > 0 \tag{2.74}$$

for all time t *outside the neighborhoods* $\mathcal{N}_i(t_i, \Delta_i)$*, in lemma 2 and* $\mathcal{N}_i(t_{i,ini}, \Delta_{i,ini})$ *in lemma 4, i.e.,*

$$t \quad \in \mathcal{I}^*_{ini} \quad = \mathcal{I}^* - \bigcup_{i=1}^{N_{i,s}} \mathcal{N}_i(t_{i,ini}, \Delta_{i,ini}), \tag{2.75}$$

where $\mathcal{I}^*$ *is defined in (2.60), and furthermore, it is assumed that there is no sticking at the initial time, i.e.,* $-t_n \in \mathcal{I}^*_{ini}$*. Additionally, let* $\hat{\dot{y}}_b(\cdot)$ *be a solution to the stepper-body velocity that is nearby the steady-state solution* $\dot{y}_{ss}(\cdot)$ *with an initial perturbation* δ_0 *at the* *beginning of the time interval ($t = -t_n$) as in (2.61). Then, the difference between the perturbed velocity $\hat{\dot{y}}_b$ and steady-state velocity $\dot{y}_{ss}$ cannot increase with time (as in (2.62)), for all $t_a, t_b \in \mathcal{I}$, provided the initial perturbation δ_0 is sufficiently small.*

Proof 5 *The proof is similar to that of lemma 3 — for the case without sustained-sticking. The main difference is for the case with sustained sticking — a perturbed solution $\hat{\dot{y}}_b$ sufficiently near the initiation of a sustained-sticking region will also have sustained sticking, and the perturbed velocity $\hat{\dot{y}}_b$ will have converged to the steady-state velocity $\dot{y}_{ss}$. For example, if sustained sticking occurs at time t_i, then a perturbed stepper-body velocity $\hat{\dot{y}}_b$, sufficiently close to the steady-state velocity $\dot{y}_{ss}$ will also lead to sustained sticking from lemma 4. Therefore, both the steady-state velocity $\dot{y}_{ss}$ and the perturbed velocity $\hat{\dot{y}}_b$ will be the same at the end (time $t_{i,fin}$) of the corresponding sustained-sticking neighborhood defined in (2.71), i.e.,*

$$\dot{y}_{ss}(t_{i,fin}) = \hat{\dot{y}}_b(t_{i,fin}),$$

leading to convergence to the steady-state solution after time $t_{i,fin}$. ■

Convergence at the initial time $-t_n$ of the periodic interval ensures convergence over the entire time interval $[-t_n, t_p]$ from lemma 3 and lemma 5 , even in the presence of Coulomb friction nonlinearity, which has a jump discontinuity with velocity. Then, standard Poincaré theory arguments [6,7] can be used to show that repeated application of the driving waveform leads to convergence to the periodic steady-state solution.

2.3.5 Rate of Convergence

The convergence rate for the entire time period can be estimated by evaluating the Poincaré map at different time-instants inside the time period $\mathcal{I} = [-t_n, t_p]$. Here the steady-state solution $\dot{y}_{ss}(\cdot)$ of the stepper dynamics (2.6)-(2.8) is found with the initial condition chosen to be the fixed point of the Poincaré map P_{y_p}, i.e., $\dot{y}_{ss}(-t_n) = X^*$. To determine the convergence rate over an entire time period $[-t_n, t_p]$, similar Poincaré maps $P_{y_p,\tau_{s,i}}$ are defined using solutions to the stepper-body dynamics over the time interval $[-t_n + \tau_{s,i}, t_p + \tau_{s,i}]$, where the time-shifts $\tau_{s,i}$ are inside the time period $[-t_n, t_p]$. Note that if solutions to the stepper dynamics converges over the entire time period $[-t_n, t_p]$ to the steady steady solution $\dot{y}_{ss}(\cdot)$, then the fixed points of each shifted Poincaré maps $P_{y_p,\tau_{s,i}}$ is the value of the steady state solution $\dot{y}_{ss}(-t_n + \tau_{s,i})$ at the shifted time $-t_n + \tau_{s,i}$ with an associated convergence rate $\gamma_{\tau_{s,i}}$ as in Lemma 1. Let γ^* be the largest value of these convergence rates,

$$\gamma^* = \sup_{\tau_{s,i} \in [-t_n, t_p]} \gamma_{\tau_{s,i}} \tag{2.76}$$

which represents the slowest convergence rate to the fixed points $\dot{y}_{ss}(\tau_{s,i})$ of the shifted Poincaré maps $P_{y_p,\tau_{s,i}}$.

Consider repeated application of the driving waveform where the first solution $\dot{y}_{b,1}(\cdot)$ of the stepper dynamics (2.6)-(2.8) is subject to the initial condition $\dot{y}_{b,1}(-t_n) = 0$ and later solutions $\dot{y}_{b,\kappa+1}(\cdot)$ are subject to the initial condition that is the final state of the previous solution, i.e.,

$$\dot{y}_{b,\kappa+1}(-t_n) = \dot{y}_{b,\kappa}(t_p). \tag{2.77}$$

Then, as in (2.40) a uniform bound on the entire time period $[-t_n, t_p]$ can be found as

$$\|\dot{y}_{b,\kappa+1}(\cdot) - \dot{y}_{ss}(\cdot)\| \leq (\gamma^*)^{\kappa} \|\dot{y}_{b,1}(\cdot) - \dot{y}_{ss}(\cdot)\|. \tag{2.78}$$

where κ is the number of applications of the driving waveform, and the distance between two solutions is defined as

$$\|\dot{y}_{b,k}(\cdot) - \dot{y}_{ss}(\cdot)\| = \max_{t \in [-t_n, t_p]} |\dot{y}_{b,k}(t) - \dot{y}_{ss}(t)|. \tag{2.79}$$

Numerically, with a finite number of shifted Poincaré maps (ten for this example), the convergence rate γ^* over the entire period can be estimated as maximum of the corresponding convergence rate as in (2.76). Then, the settling time is defined as the number of cycles κ needed to reduce the distance from the κ^{th} solution $\dot{y}_{b,\kappa}(\cdot)$ to the steady state solution $\dot{y}_{ss}(\cdot)$ to be less than 2% when compared to the distance from the initial solution $\dot{y}_{b,1}(\cdot)$ to the steady state solution $\dot{y}_{ss}(\cdot)$

$$(\gamma^*)^{\kappa} \leq 0.02. \tag{2.80}$$

An estimated settling time κ_{est} can be obtained as, from (3.28),

$$(\gamma^*_{est})^{\kappa_{est}} \leq 0.02 \tag{2.81}$$

where γ^*_{est} is the estimate of the slowest convergence rate γ^* found using a finite number of Poincaré maps (ten for the results shown here) in the time period $[-t_n, t_p]$. The settling time κ is found through simulations and the estimated settling time κ_{est} are compared in Table 2.2. The convergence is faster than the (somewhat conservative) estimate of the setting time.

Table 2.2: Estimated convergence factor γ^*_{est}, estimated settling time κ_{set} (2.81), and settling time κ (2.80) found from simulation. The settling time in seconds is given by $t_{set} = \kappa / f_{dw}$, with the driving waveform frequency $f_{dw} = 100$Hz.

Actuator Displacement (μm)	γ^*_{est}	κ_{est}	κ	$t_{set}(s)$
125	0.78	16	4	0.04
150	0.78	16	5	0.05
175	0.78	16	6	0.06
200	0.79	17	7	0.07
225	0.80	18	8	0.08
250	0.80	20	9	0.09

2.3.6 Control Law

The input (voltage V) needed to achieve the desired waveform (piezo deflection y_p) can be obtained from (2.23) as

$$\begin{aligned} V(t) = \frac{1}{K_3 Y_1(L)} (&\ddot{y}_p(t) + 2\zeta_1 \omega_1 \dot{y}_p(t) + \omega_1^2 y_p(t) \\ &- K_1 Y_1(L) \ddot{y}_b(t) - K_2 Y_1(L) \frac{F(t)}{3}). \end{aligned} \tag{2.82}$$

The input V can be partitioned into two parts: one part, V_{piezo}, is the inverse input that compensates for the piezo dynamics and the other part, $V_{friction}$, is the part that compensates for the friction, as

$$V(t) = V_{piezo} + V_{friction} \tag{2.83}$$

with

$$V_{piezo}(t) = \frac{1}{K_3 Y_1(L)} \left[\ddot{y_p}(t) + 2\zeta_1\omega_1\dot{y_p}(t) + \omega_1^2 y_p(t)\right] \tag{2.84}$$

$$V_{friction}(t) = \frac{-1}{K_3 Y_1(L)} \left[K_1 Y_1(L)\ddot{y_b}(t) + K_2 Y_1(L)\frac{F(t)}{3}\right]. \tag{2.85}$$

The components of the input $V(t)$ are shown in Fig. 2.12 for an example driving waveform with amplitude $y_{p,max} = 200\mu$m and frequency $f_{dw} = 100$Hz. Note that the dynamics of the piezo changes the shape of the input component V_{piezo} when compared to the DC-gain input V_{DC} without dynamics compensation, where

$$V_{DC}(t) = \frac{y_p(t)}{K_{DC}}. \tag{2.86}$$

The addition of the friction compensation $V_{friction}$ leads to sharp changes in the input associated with the changes in friction direction when compared to the input without the friction compensation, i.e., V_{piezo}.

2.4 Experimental Results and Discussion

This section compares the predicted and experimental observations, followed by a discussion of results.

2.4.1 Experimental Setup

The experimental system is shown in Fig. 2.13. The input signal V (2.82) was generated using Matlab and then sent through a LabView script and a National Instruments (myDAQ) digital to analog convertor. The signal was filtered to avoid exciting higher unmodeled frequencies of the piezo using two low pass filters (cutoff at 8kHz) and amplified before being applied to the stepper, which was confined to a single-axis acrylic track. A camera (60 frames per second) was used to record the overall motion of the stepper.

2.4.2 Results and Discussion

The input V (2.83) was applied to all three piezos, repetitively as in common practice for such steppers [1,15,40,41], and the distance d_i travelled by the stepper over time interval τ_i

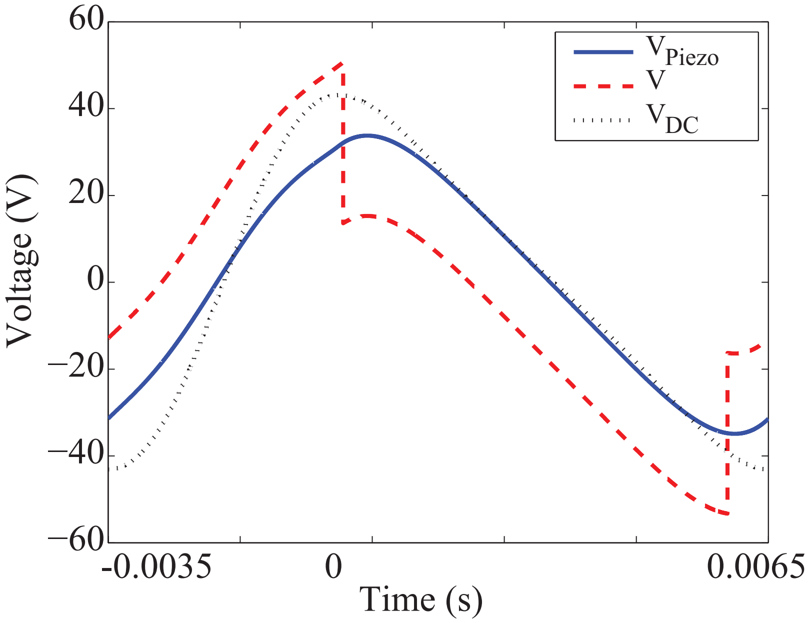

Figure 2.12: Components of the input voltage V to generate the driving waveform y_p in Fig. 2.5 with maximum actuator displacement $y_{p,max} = 200$ μm. DC-gain input V_{DC} without dynamics compensation, input component V_{piezo} with dynamics compensation, and total input V with the addition of $V_{friction}$ to the dynamics compensation V_{piezo}.

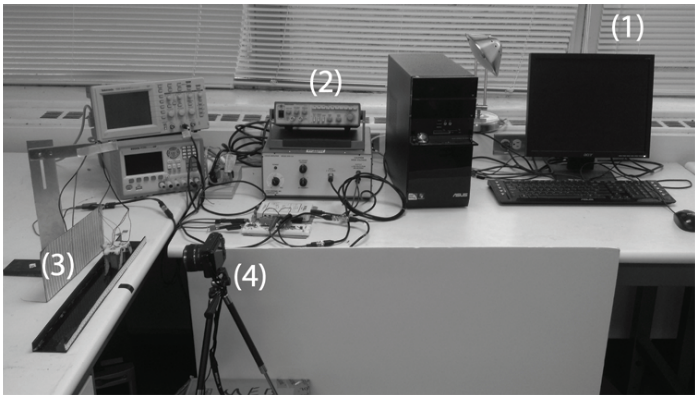

Figure 2.13: Experimental setup: (1) computer and DAQ, (2) analog circuit (amplifier and filters), (3) stepper and track, and (4) camera.

was measured using recorded video to find the average velocity $\overline{v}$ and the standard deviation $\sigma_{\overline{v}}$

$$\overline{v} = \frac{1}{n}\sum_{i=1}^{n}\left\{\frac{d_i}{\tau_i}\right\}, \quad \sigma_{\overline{v}} = \sqrt{\frac{1}{n}\sum_{i=1}^{n}(v_i - \overline{v})}. \tag{2.87}$$

The average velocity $\overline{v}$ was compared to the estimated steady-state velocity $\overline{v}_{est}$ found using the steady-state velocity $\dot{y}_{ss}$ (found through simulations)

$$\overline{v}_{est} = \frac{1}{t_p + t_n}\int_{-t_n}^{t_p} \dot{y}_{ss}(\tau)d\tau \tag{2.88}$$

and the percent error e_{avg} in the average velocity was calculated as

$$e_{avg} = \frac{|\overline{v} - \overline{v}_{est}|}{\overline{v}_{est}} \times 100. \tag{2.89}$$

The same section of the track was used for all of the experiments for consistency and the experiments were performed for different amplitudes of piezo displacements $y_{p,max}$ — $125\mu\text{m}, 150\mu\text{m}, 175\mu\text{m}, 200\mu\text{m}, 225\mu\text{m}, 250\mu\text{m}$ with seven runs at each piezo-displacement amplitude, and the results are shown in Fig. 2.14 and numerical values are provided in Table 2.3. Maximum actuator deflections $y_{p,max}$ were limited to this range, as below 125μm displacement yield negative steady-state velocities $\dot{y}_{ss}$ and deflections above 250μm began to yield inputs that are close to the breakdown voltage of the piezos. The experimental average velocities $\overline{v}$ are close to the estimated values of the average velocities $\overline{v}_{est}$ for piezo-deflections below 250μm. Deviations from estimated values become large at piezo-deflection of 250μm when substantial nonlinearities are expected as the piezo amplitude increases.

Table 2.3: Average velocity $\overline{v}$ for different maximum piezo displacement $y_{p,max}$ (μm)

	125	150	175	200	225	250
$\overline{v}_{est}$(m/s)	0.0133	0.0175	0.0217	0.0259	0.0299	0.0339
$\overline{v}$ (m/s)	0.016	0.020	0.024	0.0268	0.028	0.028
e_{avg}	17.0	10.8	11.4	3.5	5.9	17.2
$\sigma_{\overline{v}}$ (m/s)	0.0013	0.0018	0.0008	0.0020	0.0012	0.0026

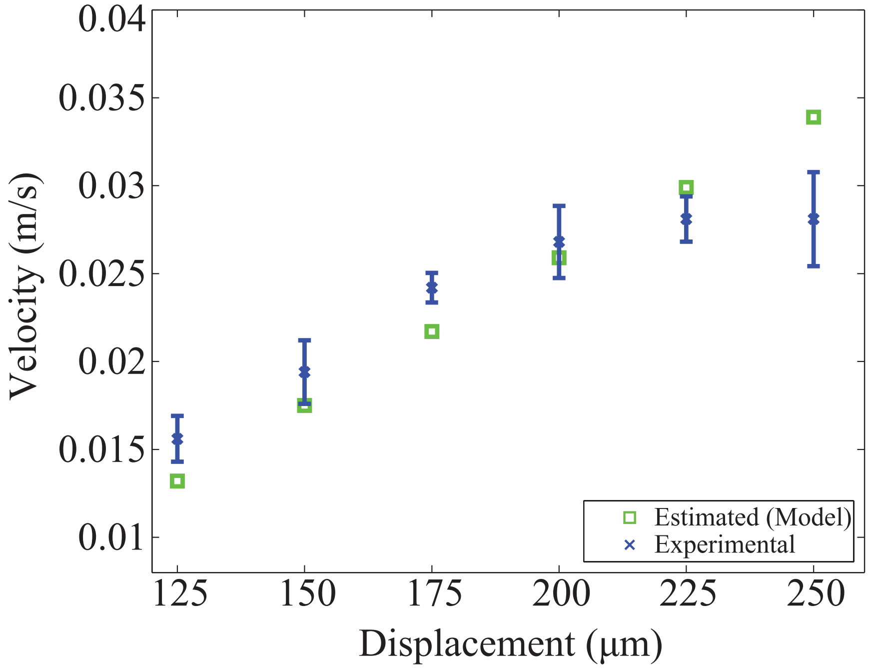

Figure 2.14: Comparison of the experimental average velocity $\overline{v}$ (2.87) with the estimated average velocity $\overline{v}_{est}$ (2.88) found from the simulation. The error bars on the experimental data represent ± one standard deviation.

2.4.3 Parameter Sensitivity

The open-loop approach proposed here will lead to errors in the achieved velocity in the presence of disturbances and modeling errors. To determine the effect of parameters errors, simulations were performed (of (2.6)-(2.8) and (2.23)) when using the input V (from 2.83) computed using the original parameter values. The steady-state percent error e_{ss} is defined as

$$e_{ss} = \frac{\overline{v}_{per} - \overline{v}_{est}}{\overline{v}_{est}} \times 100 \tag{2.90}$$

where $\overline{v}_{per}$ is the average of the steady-state velocity $\dot{y}_{ss,per}$ of the system with parameter error defined as

$$\overline{v}_{per} = \frac{1}{t_p + t_n} \int_{-t_n}^{t_p} \dot{y}_{ss,per}(\tau) d\tau. \tag{2.91}$$

The errors e_{ss} for different parameter variations are shown in Fig. 2.15 for a 100Hz waveform with maximum piezo displacement $y_{p,max} = 200\mu m$ when simulating errors in the natural frequency ω_1, damping ratio ζ_1, system mass M_t, and coefficient of kinetic friction μ_k, one parameter at a time. Note that the error e_{ss} is more sensitive to natural frequency variations when compared to the changes in the other parameters. This is because, with a sharp peak in the frequency response, a small change in the location of peak (due to changes in the natural frequency ω_1) can cause a larger error in the model (frequency response) when compared to, say, a small change in the shape of the frequency response due to change in the damping ratio ζ_1, as illustrated in Fig. 2.16. Nevertheless, as seen in Fig. 2.15, the system error tends to be small if the parameter error is small. Therefore, careful estimation of system parameters can lead to small errors. For example, the experimental results in Fig. 2.14 are close to the predicted results — even with the use of an approximate model and potential errors in estimation of parameters.

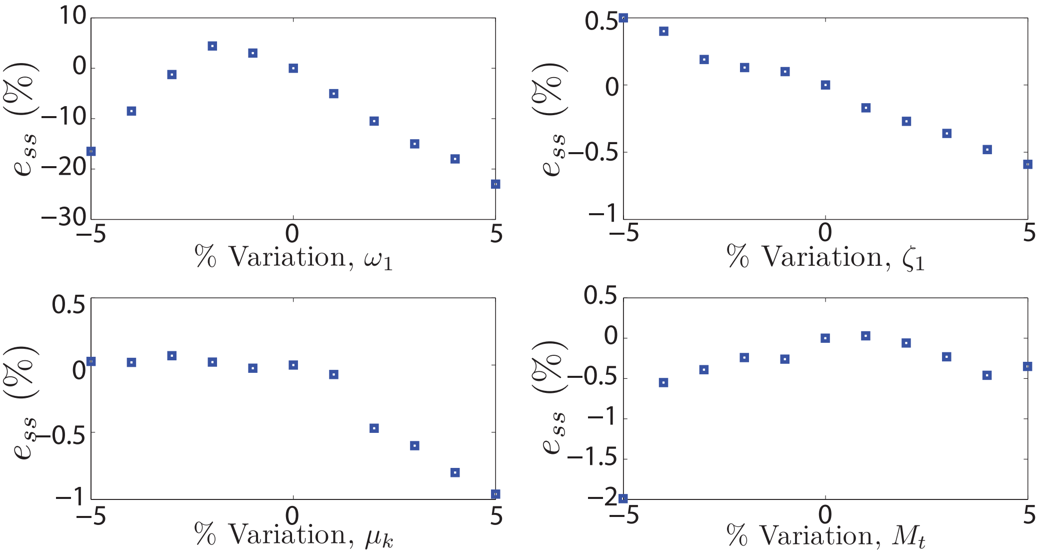

Figure 2.15: Simulation results: error e_{ss} (2.90) in the steady-state velocity with error in model parameters such as the natural frequency ω_1, damping ratio ζ_1, system mass M_t, and coefficient of kinetic friction μ_k. The error in the steady-state velocity is small if the parameter-estimation error is small.

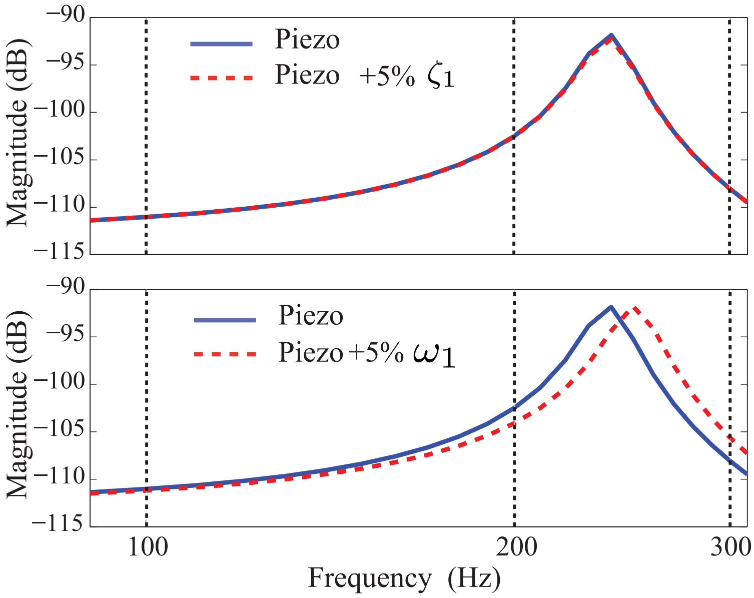

Figure 2.16: Frequency response of the modeled piezo (2.25) (Solid) and the piezo with a 5% perturbation in the damping ratio ζ_1 (dashed, top) and 5% perturbation in the natural frequency ω_1 (dashed, bottom).

2.4.4 Performance for Position Scanning

The preceding stability analysis, also provides estimates of the stepper performance, which can be used in design. For example, for velocity control, the settling time with a step change in stepper-body velocity was quantified in Table 2.2, and the size of the steady-state oscillation in the stepper-body velocity $\dot{y}_b$ seen in Fig. 2.6 was quantified in (2.35). These can be used to quantify performance of stepper-body, position control during scanning operation.

To illustrate quantification of positioning performance, consider a triangular, position scanning operation achieved by using velocity switching as shown in Fig. 2.17. The driving waveform is initially chosen as y_p (with maximum piezo deflection $y_{p,max} = 200$ μm as in Fig. 2.5) and switched to driving waveform $-y_p$ when the stepper-body position y_b reaches $y_b = y_{trans}$, then switched back to driving waveform y_p at stepper-body position $y_b =$

$-y_{trans}$, and so on. The effective scanning region (where the stepper-body velocity $\dot{y}_b$ is at steady state) is approximately 85% of the total position trajectory, and the velocity-transition region, indicated by the shaded region in Fig. 2.17, represents an "overscan" region, which is common in typical scanning applications, e.g., [42, 43].

Oscillations in the position are to be expected during the scanning region due to the triangular oscillations of the steady-state, stepper-body velocity as shown in Fig. 2.18. The positioning performance can be quantified in terms of size of the position oscillations (about the nominal triangular trajectory), which can be estimated from the size of velocity oscillations $\Delta_{max}(\dot{y}_b)$ in (2.35) as

$$\Delta_{max}(y_b) = \frac{1}{2}\left(\frac{1}{2f_{dw}}\right)\left(\frac{\Delta_{max}(\dot{y}_b)}{2}\right) = \frac{\mu_k g}{16 f_{dw}^2}. \tag{2.92}$$

The number of driving waveform cycles needed to reach steady-state position scanning at time $t_{scan,1}$ after the transition time $t_{trans,1}$ (in Fig. 2.17) can be estimated from Table 2.2 for a maximum piezo displacement $y_{p,max} = 200\mu m$ as $\kappa_{est} = 17$ cycles — the actual settling time from simulations was found to be 10 cycles, which falls within this estimate.

Note that the oscillations (in position and velocity seen in Fig. 2.18) are fundamental to this design of the stepper. Approaches to reduce these steady state oscillations include: (i) decreasing the coefficient of friction μ_k; and (ii) increasing the driving frequency f_{dw} as seen from (2.35) and (2.92).

2.4.5 Future Work

Future work will aim to design the piezo-system to reduce the oscillations in the stepper velocity. Alternate approaches, such as the use of multiple waveforms to reduce these oscillations [35] are also being investigated. Closed-loop methods can lead to additional reduction of the steady-state errors. Although feedback is not the focus of the present article, the current approach enables closed-loop schemes where the velocity (and the position) can be adjusted by changing the maximum piezo displacement to change the average velocity, e.g., as in Fig. 2.14. However, additional theoretical and experimental efforts are needed to evaluate potential feedback schemes, and their stability and robustness.

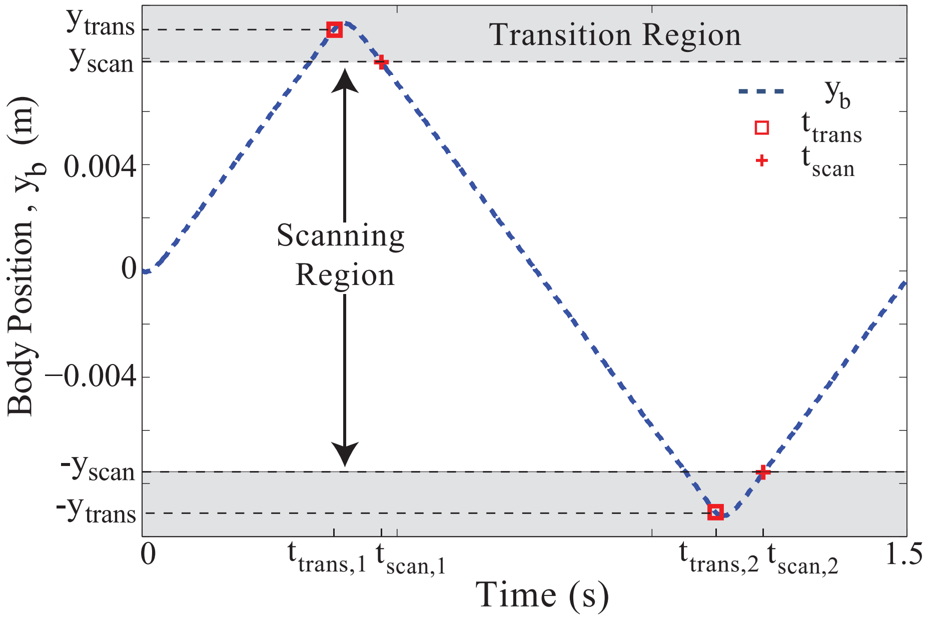

Figure 2.17: Simulation results. The stepper position y_b follows a triangular shaped scan trajectory by switching the driving waveform y_p at specified stepper positions $y_b = \pm y_{trans}$. The $\square$ at time t_{trans} denotes the beginning of the stepper-velocity transition and $+$ at time t_{scan} indicates that the stepper-velocity has reached steady state.

2.5 *Conclusion*

The control and stability of a large-range, piezoelectrically-actuated (piezo) stepper was investigated theoretically and experimentally. The analysis presented here developed conditions for the driving waveform to enable stable steady-state motion of the stepper even in the presence of Coulomb friction nonlinearity that has a jump discontinuity with velocity. Towards this, the Poincaré-Map approach was extended to evaluate the stability of the steady-state stepper velocity in the presence of discontinuities in the stepper dynamics. Moreover, experimental results show that piezo-input to achieve the driving waveform can be found by inversion of the stepper-dynamics model.

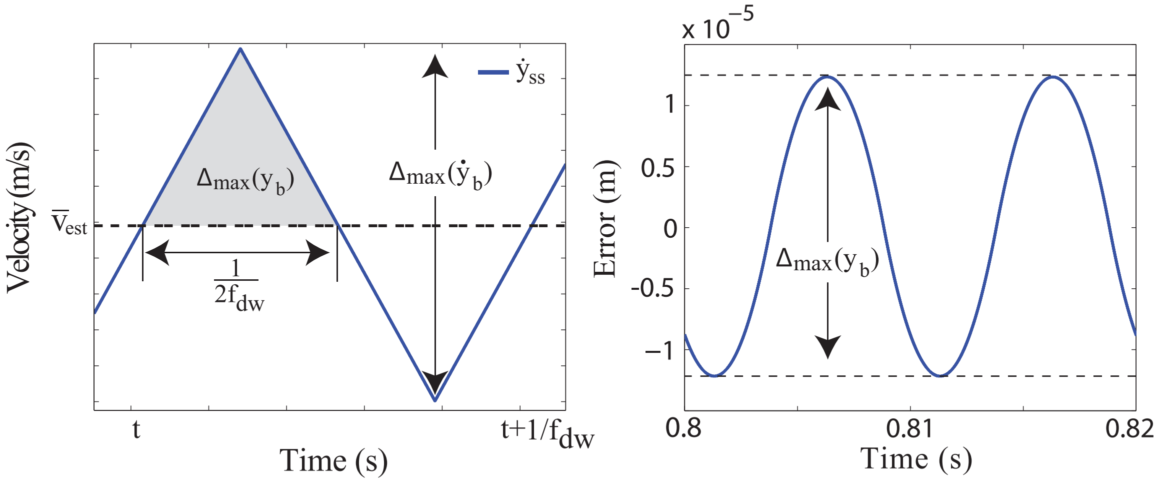

Figure 2.18: Oscillations in the stepper velocity $\dot{y}_b$ at steady state(left). The shaded region in the steady-state stepper velocity corresponds to the size of oscillations in the position y_b during scanning (right).

Chapter 3

PRECISION CONTROL THROUGH VIBRATION SUPPRESSION IN PIEZOELECTRIC-STEPPER RESPONSE

3.1 INTRODUCTION

The main contribution of this article is to show that, when compared to single actuator steppers, the response of multi-actuator steppers can be significantly less oscillatory and these reduced oscillations allow for higher precision velocity control of a motion stage. The oscillations found in the positioning response of steppers are due to the individual steps being used to generate overall large displacements. Beginning with the initial design in [20], steppers, such as those using stick-slip actuation, have been used to achieve high precision motion over a large range by using multiple small steps [13, 15, 21] in applications such as scanning probe microscopy [2, 36], and alignment of optical components [18, 19].

In current stepper applications, typical control methods use variations in the amplitude and driving patterns of the actuators to calculate a feedforward input for the desired motion of system components (e.g. motion stages or image samples). Selection of these driving waveforms to achieve motion is an important issue in the wide variety of stepper designs such as inchworm-type steppers [23], walking-type motion [24–26], and underwater insectile steppers [27]. The research efforts on this issue have focused on the selection of these waveforms, which include standard time profiles such as sinusoidal, sawtooth, and square waves [27]. Additionally, the driving waveforms can be optimized to minimize deviations between the desired and achieved motion [26].

With the application of multiple actuators, we can reduce the oscillations in the output velocity by shifting the relative phase between these waveforms. The current research shows that this approach can achieve a constant velocity for a motion stage. The ability to achieve a constant velocity will in turn lead to improvements in the positioning capabilities of stepper systems. The forces needed to achieve this constant velocity are induced by the impulse generated by the friction at the interface of the motion stage and the actuator tips. Therefore, controlling the actuator dynamics becomes a critical issue regarding the performance of the stepper system. This work develops a feedforward input that accounts for the actuator dynamics using the desired waveforms which have been shown by previous works to improve the stepper's performance [15,25]. Additionally, the stability of the stepper motion is evaluated using a Poincaré map approach, e.g. [7].

3.2 SYSTEM MODEL

This section will describe the system, the modeling of its components, and the parameters used for analysis.

3.2.1 System Description

The stepper system is designed with a motion stage supported by a bearing system and two piezoelectric bimorph actuators located below, but in contact with the motion stage as shown in Fig. 3.1. The stage is free to move horizontally and the motion of the stage, $y_s(t)$, is governed by the tip motion of the actuators, $y_p(t)$ where $p = 1, 2$, and the friction, $F_p(t)$, at the contact point between the actuators and the stage.

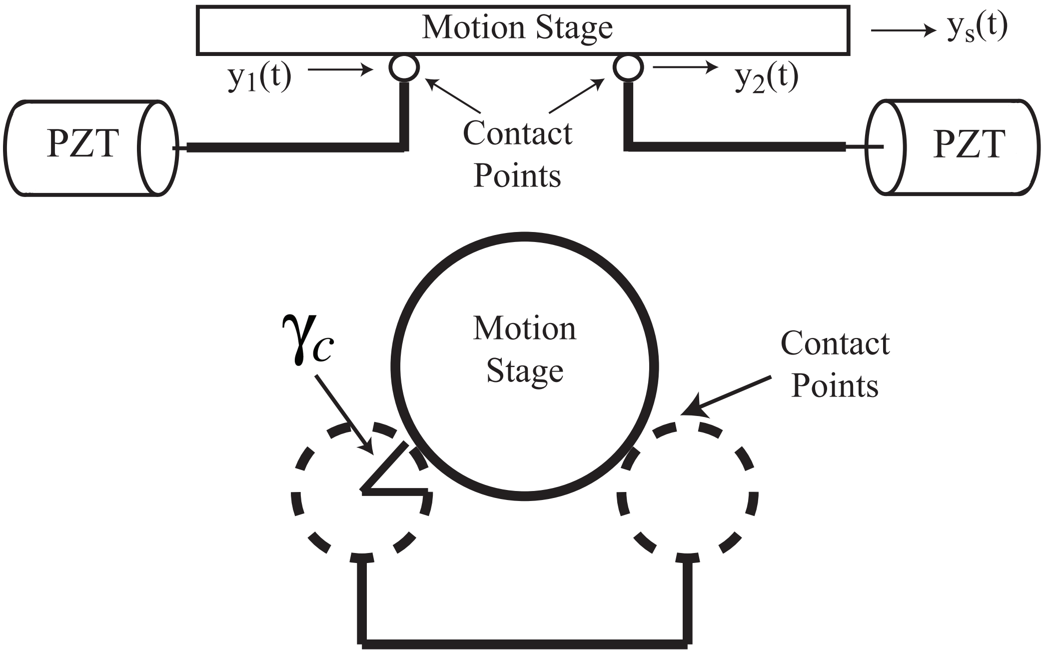

Figure 3.1: Stepper system design: The motion stage is free to move horizontally while the piezoelectric actuators bend in a cantilever fashion providing a friction force at the contact point.

The normal force acting at the actuator-stage interface can be adjusted by adjusting the forces P$_1$ and P$_2$. Adjusting these forces will influence the friction forces generated at the contact points between the stage and the actuators.

3.2.2 Stage Model

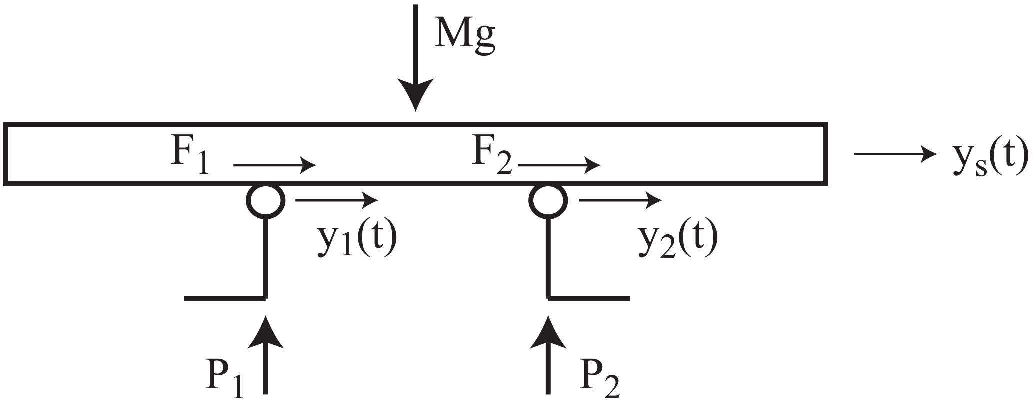

Figure 3.2: Free body diagram of the multi-actuator system. The friction forces generated at the contact points between each actuator and the stage allow the stage to move horizontally. The low friction bearings support the vertical load while their horizontal contribution is assumed to be small.

From the free body diagram, Fig. 3.2, the equation of motion of the stage in the horizontal direction is

$$\ddot{y}_s(t) = -\mu_k \frac{P_1}{M}\; sign\left[\dot{y}_s(t) - \dot{y}_1(t)\right] - \mu_k \frac{P_2}{M}\; sign\left[\dot{y}_s(t) - \dot{y}_2(t)\right] \tag{3.1}$$

where M is the mass of the stage, μ_k is the coefficient of kinetic friction, P$_p$ (with $p = 1, 2$) is the vertical force on the actuator and $y_p(t)$ (with $p = 1, 2$) is the tip trajectory of each actuator. The bearing friction is assumed to be small and is therefore neglected in the model. Defining the friction force $F_p(t)$ (with $p = 1, 2$) as

$$F_p(t) = -\mu_k \frac{P_p}{M}\; sign\left[\dot{y}_s(t) - \dot{y}_p(t)\right] \tag{3.2}$$

then the equation of motion reduces to

$$\ddot{y}_s(t) = F_1(t) + F_2(t). \tag{3.3}$$

3.2.3 Piezo-tip Deflection y_p Model

The piezo deflection for a single actuator, $y_p(t)$, is modeled as the bending of a cantilever beam.

Euler-Bernoulli beam

The net position of a point x on the piezo (see Fig. 3.2) at time t is given by the deflection $\hat{y}(x,t)$ of the piezo. The dynamics of the piezo is modeled by the Euler-Bernoulli beam approach as, e.g., [37],

$$\rho A \frac{\partial^2 \hat{y}}{\partial t^2} + EI \frac{\partial^4 \hat{y}}{\partial x^4} = f(x,t) \tag{3.4}$$

where ρ is the density, A is the cross sectional area, E is the elastic modulus, I is the moment of inertia of the piezo, and $f(x,t)$ represents external forcing. The piezo deflection $\hat{y}$ can be separated into spatial $Y(x)$ and temporal $T(t)$ parts

$$\hat{y}(x,t) = Y(x)T(t),$$

and the beam dynamics (3.4) can be rewritten as

$$\rho A \ddot{T}(t) Y(x) \ + EIT(t) \frac{\partial^4 Y}{\partial x^4}(x) = f(x,t). \tag{3.5}$$

The homogeneous form of Eq. (3.5), obtained by setting the right hand side $f(x,t) = 0$, can separated into independent spatial and temporal equations

$$\frac{EI \frac{\partial^4 Y}{\partial x^4}(x)}{\rho A Y(x)} = \ \omega_n^2 \quad \text{and} \quad \frac{\ddot{T}(t)}{T(t)} = \ -\omega_n^2, \tag{3.6}$$

with the standard boundary conditions for a cantilever beam:

$$\hat{y}(0,t) = 0; \ \frac{\partial \hat{y}}{\partial x}(0,t) = 0; \ \frac{\partial^2 \hat{y}}{\partial x^2}(L,t) = 0; \ \frac{\partial^3 \hat{y}}{\partial x^3}(L,t) = 0,$$

where L is the piezo length. The resulting spatial solution of the n^{th} mode Y_n is given by [37]

$$Y_n(x) = sin(\beta_n x) - sinh(\beta_n x) + \sigma_n(cos(\beta_n x) - cosh(\beta_n x)), \tag{3.7}$$

where

$$\beta_n^4 = \frac{\omega_n^2 \rho A}{EI}, \qquad \sigma_n = \frac{sin(\beta_n L) + sinh(\beta_n L)}{cos(\beta_n L) + cosh(\beta_n L)}, \tag{3.8}$$

and for the first ($n = 1$) vibrational mode [37],

$$\beta_1 L = 1.875 \quad \text{and} \quad \sigma_1 = 0.7341.$$

spatial solution Y_n given by [37]. For the non-homogeneous case ($f(x,t) \neq 0$ in Eq. (3.5), the general piezo deflection piezo deflection w can be considered to be a linear combination of these mode shapes, i.e.,

$$\hat{y}(x,t) = \sum_{1}^{\infty} Y_n(x) T_n(t). \tag{3.9}$$

Dynamics of the First Vibrational Mode

Using the orthogonality of the mode shapes, the first mode dynamics ($n = 1$) can be extracted from Eq. (3.5) by: (i) substituting the piezo displacement $\hat{y}(x,t)$ from Eq. (3.9); (ii) multiplying Eq. (3.5) with the first mode shape $Y_1(x)$; and (iii) integrating over the beam length, i.e.,

$$\begin{aligned} \sum_{1}^{\infty} \left[\int_0^L Y_1 Y_n \ddot{T}_n dx + \frac{EI}{\rho A} \int_0^L Y_1 \beta_n^4 Y_n T_n dx \right] \\ = \frac{1}{\rho A} \int_0^L Y_1(x) f(x,t) dx \end{aligned} \tag{3.10}$$

to yield

$$\ddot{T}_1 + \omega_1^2 T_1 = \frac{1}{\rho A} \frac{\int_0^L Y_1(x) f(x,t) dx}{\int_0^L Y_1(x) Y_1(x) dx}. \tag{3.11}$$

The external forcing term $f(x,t)$, see Eq. (3.5), is given by

$$f(x,t) = M(t) \frac{\partial \delta(x-L)}{\partial x} + F_p(t) \delta(x-L) \tag{3.12}$$

where $M(t)$ is the applied moment due the voltage V acting on the piezo

$$M(t) \ = \frac{6 d_{31} EI}{H^2} V(t) \ = K_{MV} V(t), \tag{3.13}$$

H is the thickness of the piezo and d_{31} is a piezoelectric coefficient. Moreover, external forcing term $f(x,t)$ includes friction force $F_p(t)$ for each actuator. Integration of Eq. (3.11) and the addition of a damping term leads to

$$\ddot{T}_1 + 2\zeta_1 \omega_1 \dot{T}_1(t) + \omega_1^2 T_1 \ = K_1 F_p(t) + K_2 V(t) \tag{3.14}$$

where

$$K_1 = \frac{Y_1(L)}{\rho A \int_0^L Y_1^2(x)dx}; \quad K_2 = \frac{K_{MV}}{\rho A \int_0^L Y_1^2(x)dx} \left. \frac{\partial Y_1(x)}{\partial x} \right|_{x=L} \tag{3.15}$$

and ζ_1 is the damping ratio. With the one-vibrational-mode model, the piezo-tip deflection $y_p(t) = \hat{y}(L,t)$ (where $p = 1, 2$) becomes (from Eq. 3.9)

$$y_p(t) = Y_1(L)T_1(t), \tag{3.16}$$

which can be substituted into Eq. (3.14) to obtain the piezo-tip dynamics

$$\ddot{y}_p(t) + 2\zeta_1\omega_1\dot{y}_p(t) + \omega_1^2 y_p(t) = Y_1(L)\left[K_1F_p(t) + K_2V(t)\right]. \tag{3.17}$$

Values from experimental results (frequency response in Fig.3.3) shown in Table 3.1 are used in the simulations.

Table 3.1: Values of Model Parameters

Variable	Value	Units
L	28.6	mm
W	12.7	mm
H	0.51	mm
ω_1	1501	rad/s
ζ	0.45	
K_{DC}	2.32	μm/V
ρ	7600	kg/m^3
K_1	2.8 $\times 10^3$	1/Ns^2
K_2	5.2	rad/Vs
g	9.81	m/s^2
μ_k	0.4	

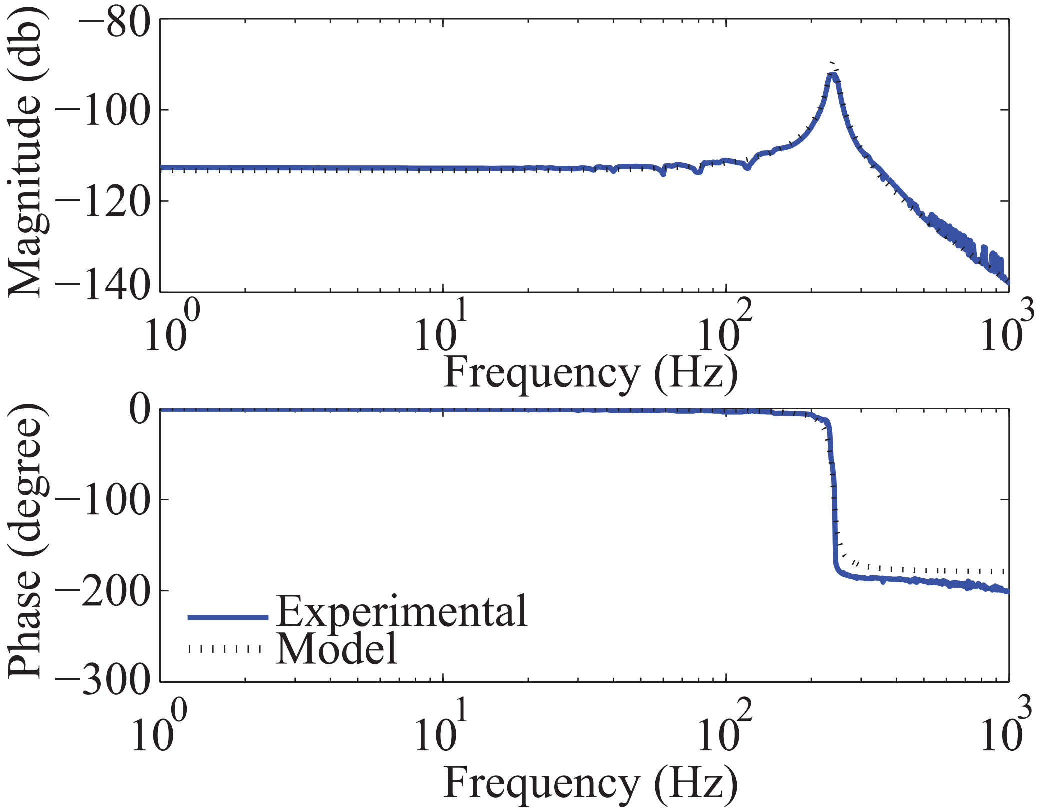

Figure 3.3: Experimental (solid line) and fitted (dotted line) frequency response. The experimental frequency response can be modeled with a second order model upto 1kHz.

3.3 CONTROL AND STABILITY ANALYSIS

The generation of the driving waveforms, the stability of the resulting motion from these waveforms, and the feedforward input to achieve these waveforms are presented in this section.

3.3.1 Driving Waveform

The piezo-deflection velocity, $\dot{y}_p(t)$, of each piezo $(p = 1, 2)$ affects the friction forces $F_p(t)$, which in turn, affect the stage dynamics $y_s(t)$. For example, if the stage velocity $\dot{y}_s = 0$, then from Eq. 3.1, the friction forces $F_p(t) > 0$ if both $y_1(t) < 0$ and $y_2(t) < 0$ and similarly, $F_p(t) < 0$ if both $y_1(t) > 0$ and $y_2(t) > 0$. Therefore, the time intervals during which the piezo-deflection velocity $\dot{y}_p(t)$ remains positive or negative (e.g., t_n and t_p as in Fig. 3.4) can be adjusted to generate a net impulse to drive the stage motion.

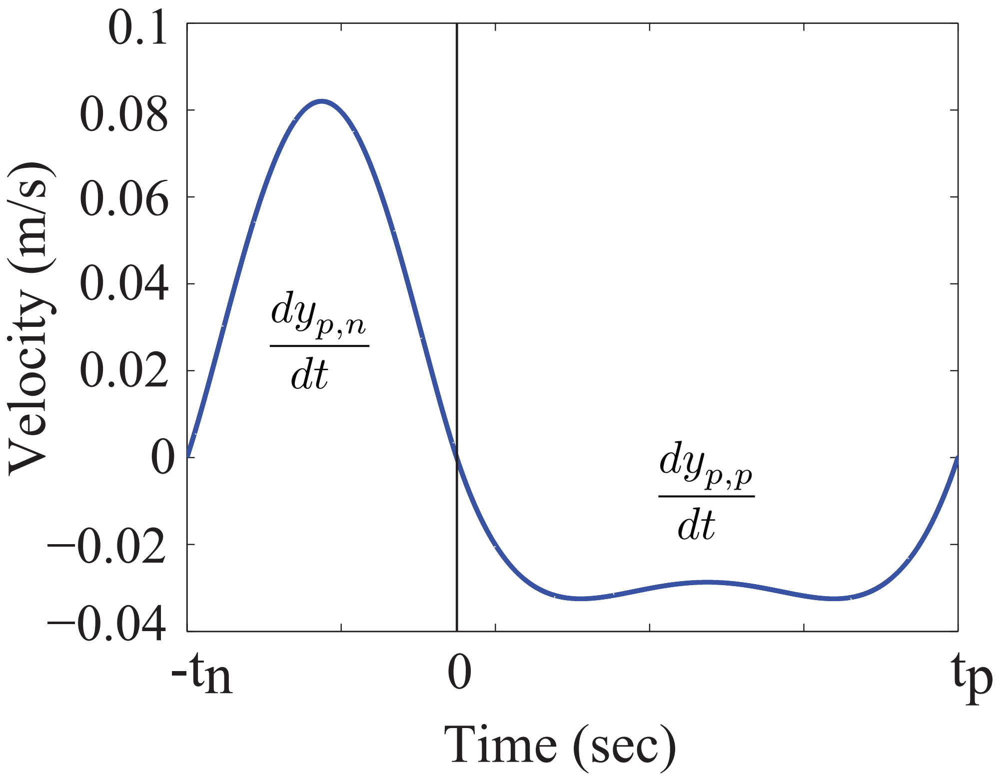

Figure 3.4: Example piezo-deflection velocity, which is positive over the time interval $(-t_n, 0)$ and negative over the time interval $(0, t_p)$.

To generate the piezo-deflection profile, $y_p(t)$, two polynomials are generated with a total time period of $t_p + t_n$ as

$$\begin{aligned} y_p(t) &= y_{p,p}(t) \quad \forall t \in [0, t_p] \\ y_p(t) &= y_{p,n}(t) \quad \forall t \in [-t_n, 0] \end{aligned}$$

where

$$\begin{aligned} y_{p,p}(t) &= a_p t^5 + b_p t^4 + c_p t^3 + d_p t^2 + e_p t + f_p \\ y_{p,n}(t) &= a_n t^5 + b_n t^4 + c_n t^3 + d_n t^2 + e_n t + f_n, \end{aligned}$$

the coefficients are found by the following continuity conditions on the piezo-deflection polynomials $y_{p,p}, y_{p,n}$

$$\begin{aligned} y_{p,n}(-t_n) &= y_{p,p}(t_p) &&= -y_{p,max}/2 \\ y_{p,n}(0) &= y_{p,p}(0) &&= +y_{p,max}/2 \end{aligned} \tag{3.18}$$

and their first to third time-derivatives i.e.,

$$\begin{aligned} \frac{dy_{p,n}}{dt}(0) &= \frac{dy_{p,p}}{dt}(0) = 0 \\ \frac{dy_{p,n}}{dt}(-t_n) &= \frac{dy_{p,p}}{dt}(t_p) = 0 \\ \frac{d^k y_{p,n}}{dt^k}(0) &= \frac{d^k y_{p,p}}{dt^k}(0) \ for \ k = 2, 3 \\ \frac{d^k y_{p,n}}{dt^k}(-t_n) &= \frac{d^k y_{p,p}}{dt^k}(t_p) \ for \ k = 2, 3 \end{aligned} \tag{3.19}$$

where $y_{p,max}$ is the maximum piezo deflection.

3.3.2 Stage Motion for Given Driving Waveform

The same waveforms are used for both piezos, where their phase with respect to one another can be adjusted by a phase shift ratio, i.e., the velocity of the first piezo, $\dot{y}_1(t)$, and the velocity of the second piezo, $\dot{y}_2(t)$, are related by

$$\dot{y}_2(t) = \dot{y}_1(t + \phi(t_n + t_p)). \tag{3.20}$$

Here the phase-shift ratio $0 \leq \phi \leq 1$ is a fraction of the time period $(t_n + t_p)$. For example, the driving waveform for the first piezo $y_1(t)$ such that $t_n = 0.0035\ s$, $t_p = 0.0075\ s$, and $y_{p,max} = 200\mu m$ is shown in Fig. 3.5. This driving waveform is periodic with frequency

$$f_{dw} = 1/(t_n + t_p)$$

chosen as 100 Hz, and with $y_{p,n}$ defined for $t \in [0, 0.0035]$ and $y_{p,p}$ defined for $t \in [0.0035, 0.01]$. With a phase-shift of $(t_n + t_p)/2$ ($i.e.\ \phi = 1/2$), $\dot{y}_2(t)$ is then defined (see Fig. 3.6)

From the model of the friction forces, $F_p(t)$, in Eq. 3.1, it can be shown that the stage velocity, $\dot{y}_s$ is bounded. For example, if the stage velocity is sufficiently large, i.e.

$$\dot{y}_s(t) \ > \ \max_{\tau}\{\dot{y}_1(\tau), \dot{y}_2(\tau)\} \ > \ 0 \tag{3.21}$$

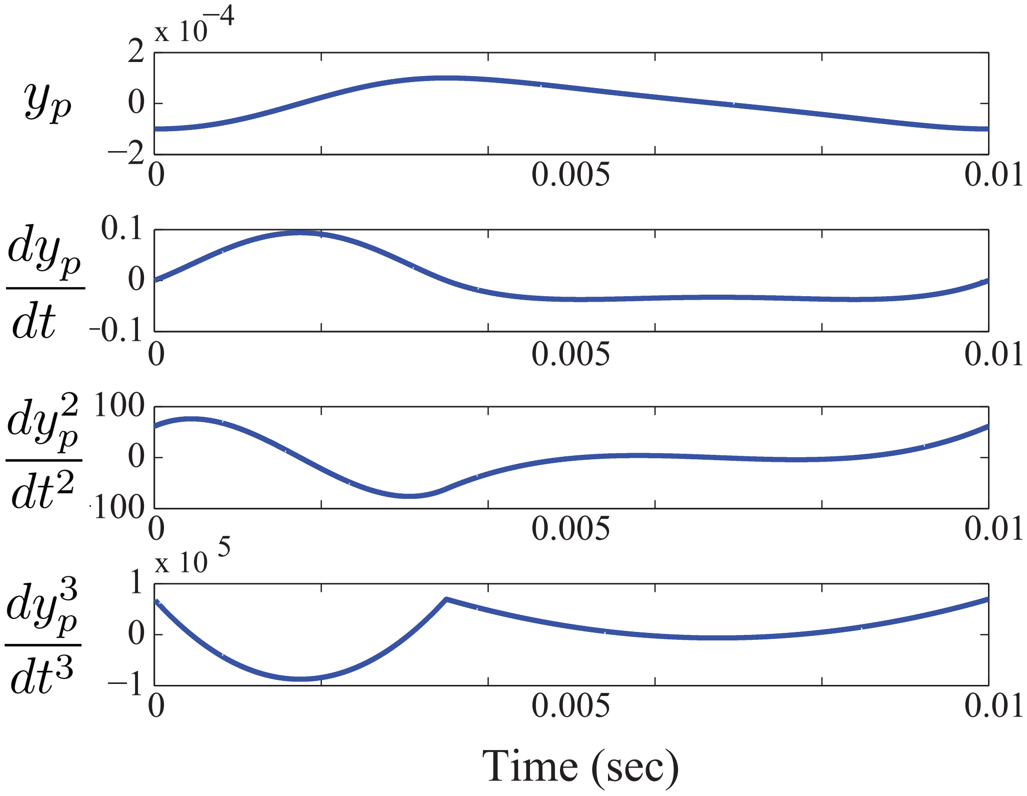

Figure 3.5: Example trajectories of the piezo : position y_p, velocity dy_p/dt, acceleration dy_p^2/dt^2, and jerk dy_p^3/dt^2. These trajectories represent a 100 Hz trajectory with a 200 μm piezo-tip displacement with the negative time polynomial $y_{p,n}$ and the positive time polynomial $y_{p,p}$ comprising 35% and 65% of the total period, respectively.

then the acceleration of the stage, $\ddot{y}_s(t)$, is guaranteed to be negative and therefore the stage velocity, $\dot{y}_s(t)$, will decrease. A similar argument can be made for the minimum stage velocity. Similarly, if

$$\dot{y}_s(t) \;<\; \min_{\tau}\{\dot{y}_1(\tau), \dot{y}_2(\tau)\} \;<\; 0 \tag{3.22}$$

then the stage velocity, $\dot{y}_s(t)$, will increase. Thus, the stage velocity, $\dot{y}_s(t)$ will converge to the following region of attraction

$$\min_{\tau}\{\dot{y}_1(\tau), \dot{y}_2(\tau)\} \leq \dot{y}_s(t) \leq \max_{\tau}\{\dot{y}_1(\tau), \dot{y}_2(\tau)\}. \tag{3.23}$$

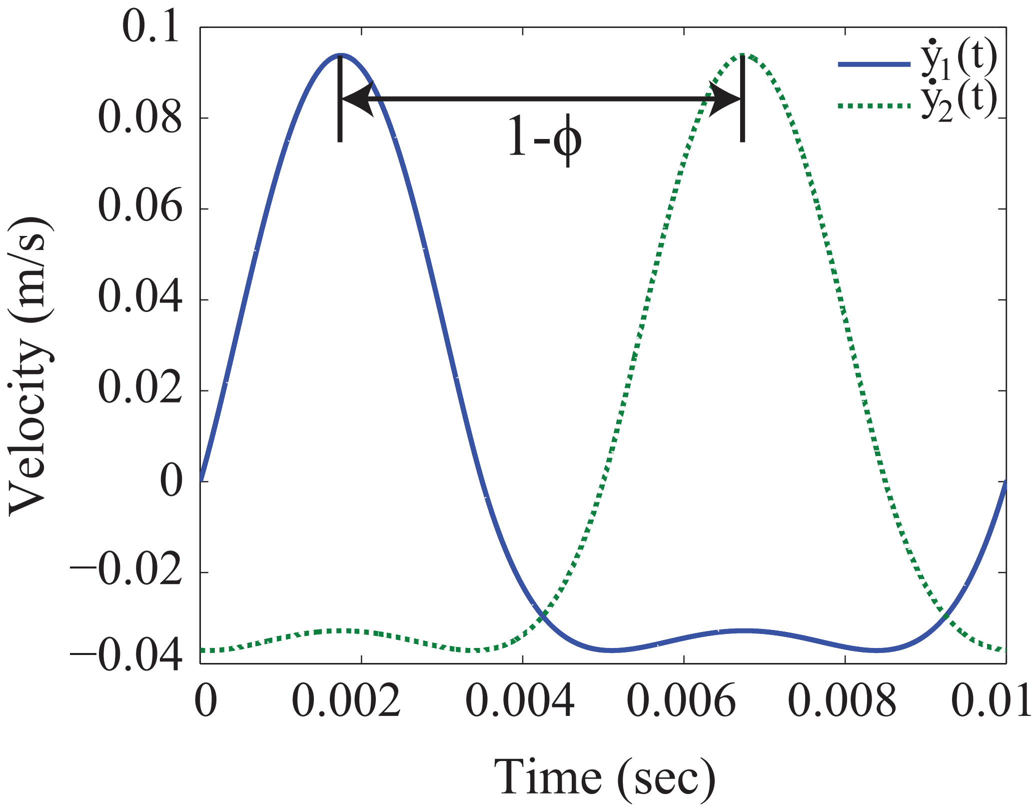

Figure 3.6: Example of phase shifted trajectories: The motion of the second actuator, $\dot{y}_2(t)$, is shifted away from the motion of the first actuator, $\dot{y}_1(t)$ by ϕ as in Eq. 3.20

With any responses outside the region being attracted towards it, the stability inside this region needs to be determined.

3.3.3 Stability in the Region of Attraction

To evaluate the potential stability of the steady-state stage motion, generate the Poincaré map, P_y, for the given set of piezo driving waveforms $y_1(t)$ and $y_2(t)$.

$$P_y \ : X \to P_y\left[X\right] \tag{3.24}$$

obtained as the solution of the stage motion dynamics over one time period $[-t_n, t_p]$, i.e.

$$X = \dot{y}_s(-t_n); \qquad P_y\left[X\right] = \dot{y}_s(t_p) \tag{3.25}$$

as illustrated in Fig. 3.7 and Fig. 3.8 for different initial conditions $\dot{y}_s(-t_n)$. The steady-state solution with the same initial and final states

$$X^* = \dot{y}_s(-t_n) = \dot{y}_s(t_p) \tag{3.26}$$

is shown in green. The resulting Poincaré map, P_y, is plotted as a function in Fig. 3.9, with a fixed point at X^*. The Poincaré map is inside the region bounded by straight lines of slope γ and $-\gamma$ passing through the the steady state solution X^*, i.e.,

$$|P_y[X] - X^*| \leq \gamma |X - X^*| \tag{3.27}$$

where γ was found through numerical solutions as 0.9.

Repeated application of the Poincaré map (as illustrated in Fig. 3.9), i.e.,

$$X_{k+1} = P_y[X_k]$$

starting with any X_1 leads to convergence of X_k to the fixed point X^*, i.e.,

$$\lim_{k\to\infty} X_k \to X^*$$

because

$$\begin{aligned} |X_{k+1} - X^*| &= |P_y[X_k] - X^*| \\ &\leq \gamma\,|X_k - X^*| \\ &\leq \gamma^k\,|X_1 - X^*| \end{aligned} \tag{3.28}$$

and

$$\lim_{k\to\infty} \gamma^k \to 0 \qquad \text{if } 0 \leq \gamma < 1.$$

3.3.4 Feedforward Control

The feedforward input voltages, $V_p(t)$, needed for each piezo to achieve both the desired waveforms, $y_p(t)$, and the steady-state response, $y_s(t)$, can be obtained by rearranging Eq. 3.17 using a standard second order model inverse for the piezo dynamics, V_{piezo}, as

$$V_p(t) = V_{piezo} + V_{friction} \tag{3.29}$$

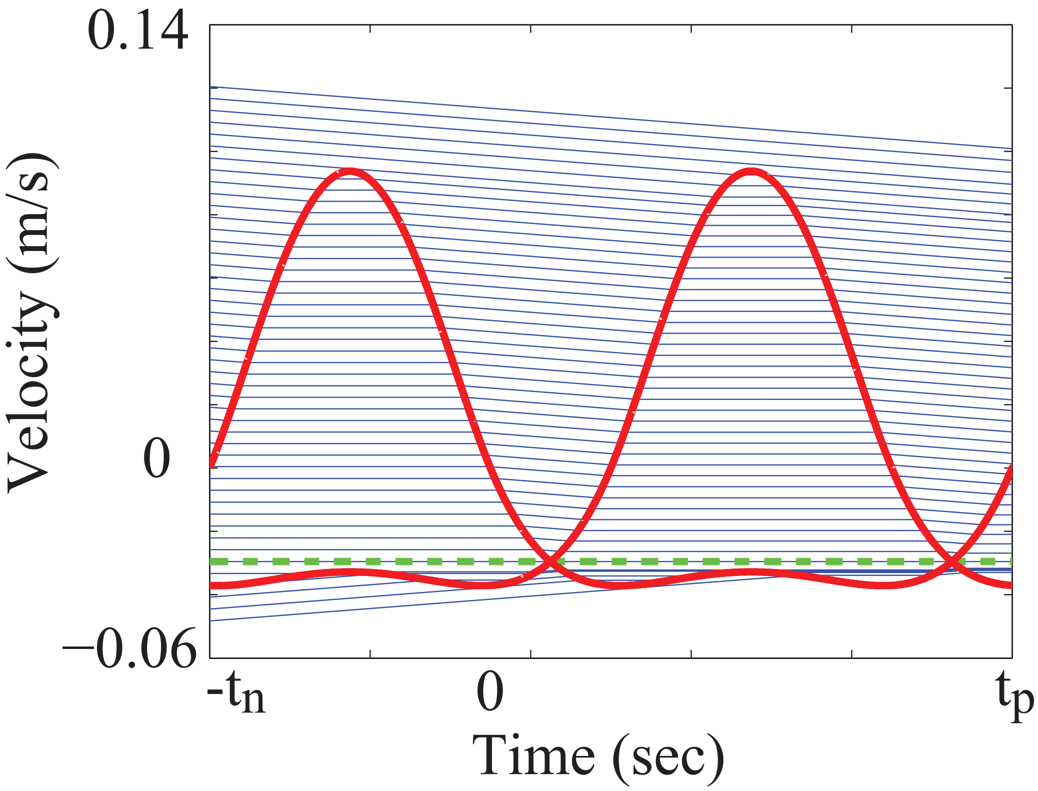

Figure 3.7: Motion stage velocity, $\dot{y}_s$, over one time period $[-t_n, t_p]$ for the driving waveforms in Fig. 3.6 with phase-shift ratio $\phi = 1/2$. The driving waveforms velocities ($\dot{y}_1(t)$, $\dot{y}_2(t)$) are shown in red and the resulting steady-state solution shown in green (dashed line) is constant with $\dot{y}_s(-t_n) = \dot{y}_s(t_p)$.

where

$$V_{piezo} = \frac{1}{K_2 Y_1(L)}(\ddot{y}_p(t) + 2\zeta_1\omega_1\dot{y}_p(t) + \omega_1^2 y_p(t)) \tag{3.30}$$

$$V_{friction} = \frac{-1}{K_2 Y_1(L)}(Y_1(L) K_1 F_p(t)) \tag{3.31}$$

where $p = 1, 2$ and $V_{friction}$ containing the friction dynamics. Computing the feedforward input requires: (i) the desired motion of the piezo ($y_p(t)$, $\dot{y}_p(t)$, $\ddot{y}_p(t)$); and (ii) the friction force $F_p(t)$ which is a function of the piezo motion as well as the steady-state motion of the motion stage, $\dot{y}_s(t)$, found via simulation. The piezo response with this input will generate

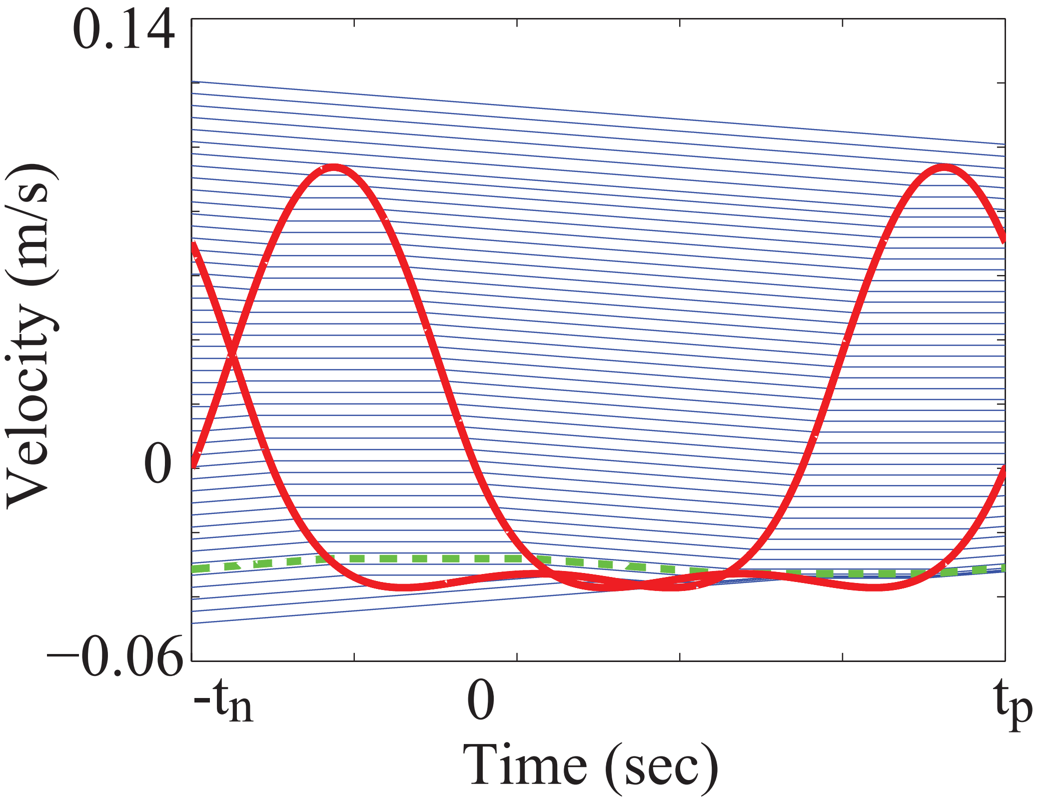

Figure 3.8: Motion stage velocity, $\dot{y}_s$, over one time period $[-t_n, t_p]$ for the driving waveforms in Fig. 3.6 with phase-shift ratio $\phi = 1/4$. The driving waveforms velocities ($\dot{y}_1(t)$, $\dot{y}_2(t)$) are shown in red and the resulting steady-state solution shown in green (dashed line) with $\dot{y}_s(-t_n) = \dot{y}_s(t_p)$. With $\phi = 1/4$, the resulting steady-state solution is not constant over the time period $[-t_n, t_p]$.

the correct friction at each piezo-tip such that the motion stage will achieve the constant velocity represented by the fixed point X^* in Fig. 3.9.

3.4 Results and Discussion

The effect of the phase shift ratio on the steady-state velocity response of the motion stage and controlling this steady state velocity by changing the driving waveform are investigated below.

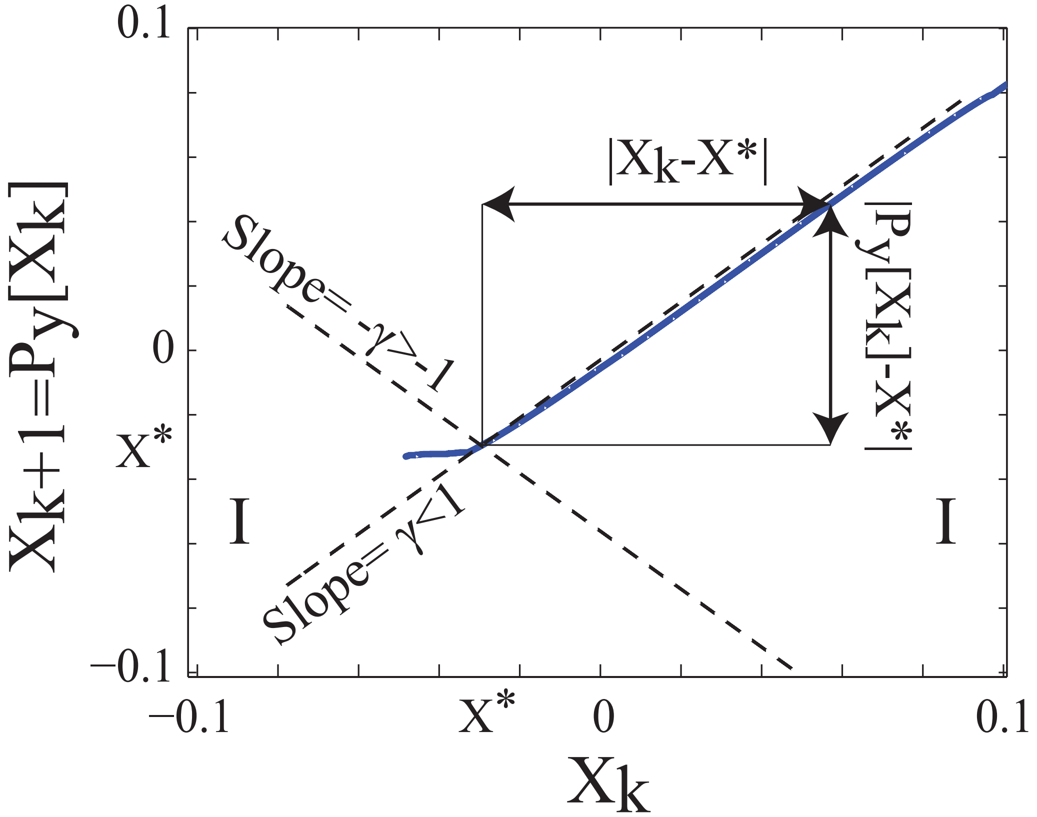

Figure 3.9: Poincaré map (solid line), P_y, associated with the piezo dynamics shown in Fig. 3.6. The dashed lines have slope $\pm\gamma = 0.9$ and pass through the fixed point X^*. Region I, bounded by the dashed lines, guarantees that $|P_y[X_k] - X^*|$ is always less than $\gamma|X_k - X^*|$.

3.4.1 Minimizing Steady-State Velocity Oscillations

The magnitude of the oscillations in the steady-state velocity of the motion stage $\dot{y}_s(t)$ depend on the phase-shift ratio ϕ, which is shown in Fig. 3.10. From Fig. 3.10, it can be seen that, as the two actuation signals become more out of phase, the magnitude of oscillation decreases. When the two piezos are one half period out of phase (phase-shift ratio $\phi = 1/2$), the magnitude of the oscillations reaches a minimum where the vibrations are suppressed and the stage velocity is constant.

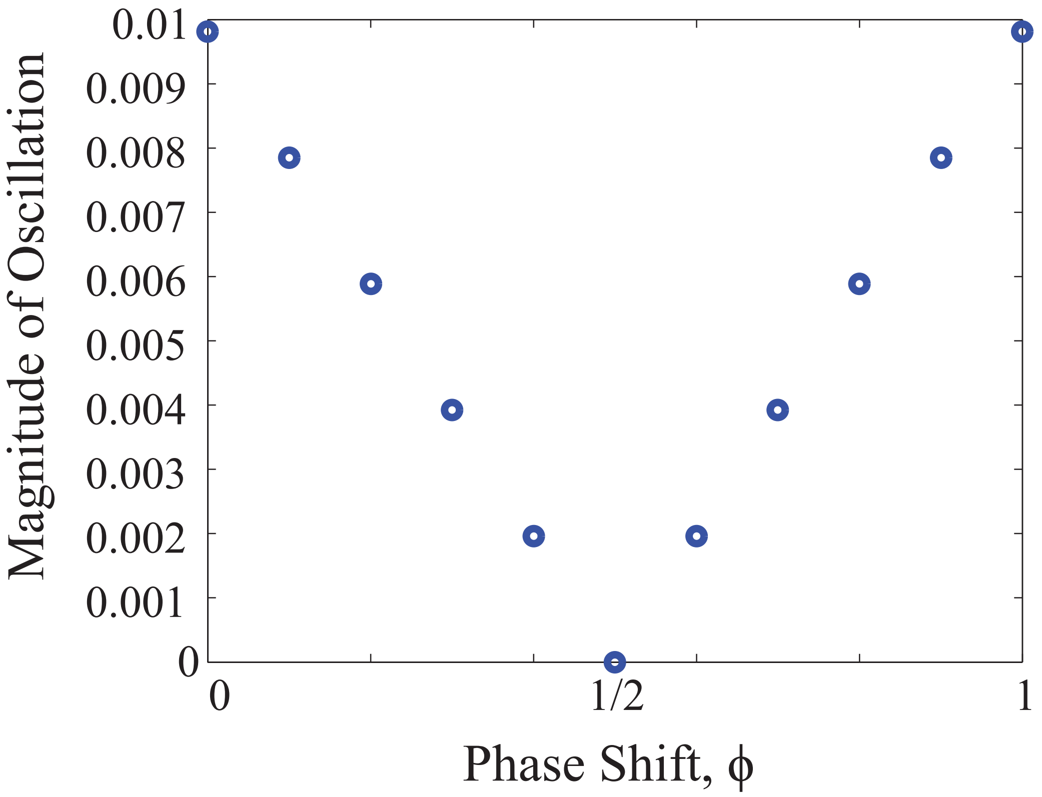

Figure 3.10: The magnitude of oscillations for the steady-state response of $\dot{y}_s(t)$ changes as the motion of the piezos, $(\dot{y}_1(t),\ \dot{y}_2(t))$ become out of phase with one another. The oscillations are suppressed when the piezos are one half period out of phase ($\phi = 1/2$).

3.4.2 Why is the Oscillation Zero?

A constant stage velocity $\dot{y}_s(t) = \dot{Y}_S$ can only be achieved if the acceleration of the stage, $\ddot{y}_s(t)$, is zero, i.e., from the stage dynamics Eq. 3.1,

$$sign\left[\dot{y}_1(t) - \dot{Y}_S\right] = -sign\left[\dot{y}_2(t) - \dot{Y}_S\right] \tag{3.32}$$

at all time instants.

Lemma 6 *Let $\dot{y}_1(\cdot)$ be a continuous velocity profile with period $\tau_p = t_p + t_n$, e.g., as shown in Fig. 3.11. If there exists a constant $\dot{Y}_S$ such that the shifted velocity-profile $\dot{y}_1(\cdot) - \dot{Y}_S$ is* *negative over a time interval,* I_{neg}*,*

$$I_{neg} = (\tau_1, \tau_2) \tag{3.33}$$

of length $\tau_2 - \tau_1 = \tau_p/2$ *and positive for the rest of the period* $[0, \tau_p]$ *(except for* τ_1 *and* τ_2*), i.e., time interval,* I_{pos}*, is*

$$I_{pos} = [0, \tau_p] - I_{neg} \tag{3.34}$$

then

$$sign\left[\dot{y}_1(t) - \dot{Y}_S\right] = -sign\left[\dot{y}_1(t + \phi\tau_p) - \dot{Y}_S\right] \quad \forall\ t \tag{3.35}$$

if the phase-shift ratio is $\phi = 1/2$*.*

Proof 6 *For any given time* t_1 *in the interval* (τ_1, τ_2)*, the addition of half the time period, i.e.,* $t_2 = t_1 + \tau_p/2$ *modulo the time period* τ_p *leads to a point outside the interval* (τ_1, τ_2)*, i.e.,*

$$[t + \tau_p/2 \mod \tau_p] \qquad \notin (\tau_1, \tau_2) \tag{3.36}$$

because

$$\begin{aligned} t_2 &= t_1 + \tau_p/2 \\ &> [\tau_1] + \tau_p/2 \\ &> [\tau_2 - \tau_p/2] + \tau_p/2 = \tau_2 + \tau_p/2 \\ &> \tau_2 \end{aligned} \tag{3.37}$$

or $t_2 > \tau_2$ *and* $t_2 = t_1 + \tau_p/2 < \tau_2 + \tau_p/2$*, hence*

$$t_2 \quad \in \quad (\tau_2, \tau_2 + \tau_p/2) = (\tau_2, \tau_1 + \tau_p)\,.$$

Therefore, from Eq. (3.36)

$$sign(\dot{y}_1(t + \tau_p/2) - \dot{Y}_S) = \begin{cases} 1 & if\ t \in I_{neg} \\ -1 & if\ t \in I_{pos} \end{cases}$$

and Eq. 3.35 of the Lemma follows.

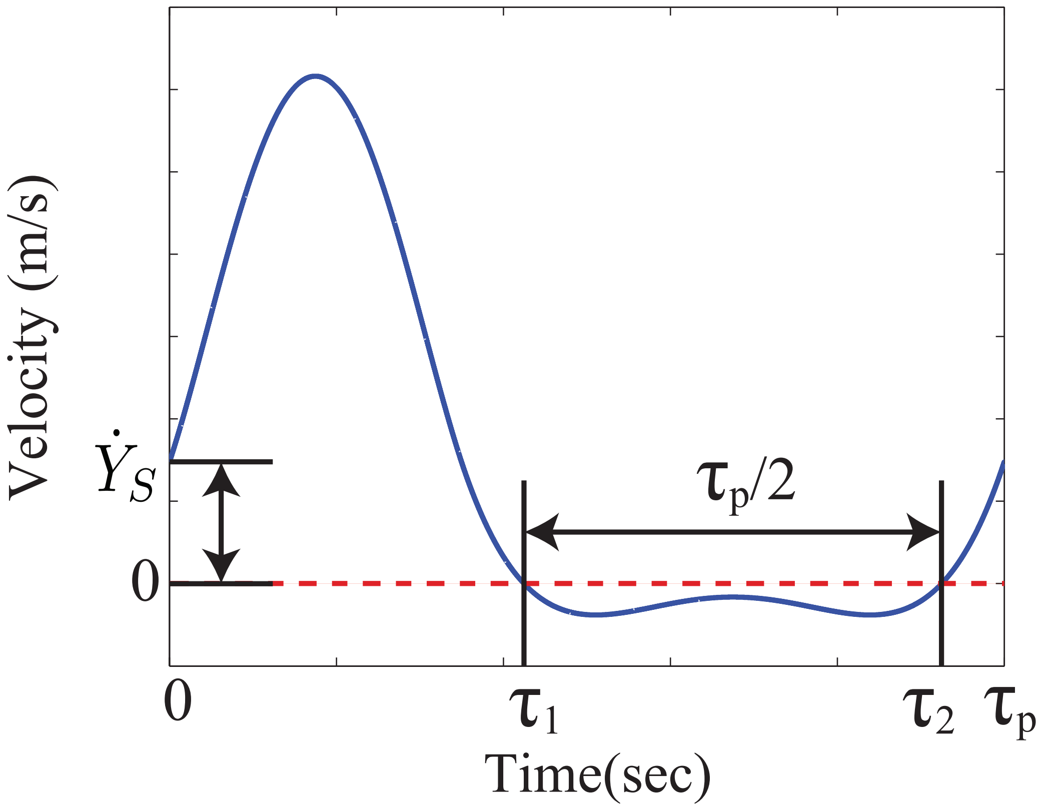

Figure 3.11: Plot of $\dot{y}_1(t) - \dot{Y}_S$, the argument of the $sign(\cdot)$ function for the left hand side of Eq. 3.32. The time interval where $\dot{y}_1(t) - \dot{Y}_S$ is positive is $t \in \{[0, \tau_1] \cup [\tau_2, t_n + t_p]\}$ and is the same duration as the time interval that $\dot{y}_1(t) - \dot{Y}_S$ is negative as $t \in [\tau_1, \tau_2]$.

■

The above Lemma implies that the acceleration of the stage is zero when the phase-shift ratio is one half and the stage velocity is $\dot{y}_s = \dot{Y}_S$ because Eq 3.35 of the lemma implies Eq. 3.32, which is illustrated in Fig. 3.12 for the waveforms defined in Fig. 3.6. Note that the time interval where $\dot{y}_2(t) - \dot{Y}_S$ is negative is $t \in \{[0, \tau_1] \cup [\tau_2, t_n + t_p]\}$ and is the same duration as the time interval that $\dot{y}_2(t) - \dot{Y}_S$ is positive as $t \in [\tau_1, \tau_2]$.

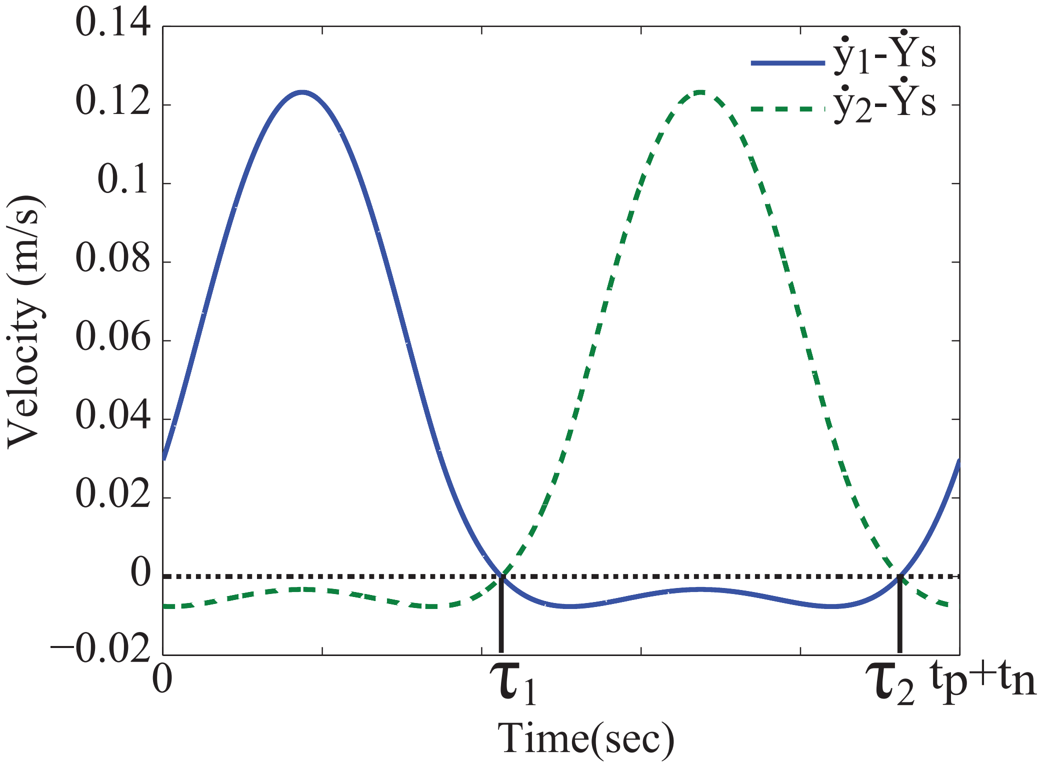

Figure 3.12: Plot of $\dot{y}_1(t) - \dot{Y}_S$ and $\dot{y}_2(t) - \dot{Y}_S$ in Eq. 3.32. The time interval where $\dot{y}_2(t) - \dot{Y}_S$ is negative is $t \in \{[0, \tau_1] \cup [\tau_2, t_n + t_p]\}$ and is the same duration as the time interval that $\dot{y}_2(t) - \dot{Y}_S$ is positive as $t \in [\tau_1, \tau_2]$.

3.4.3 Comparison of Single and Two-Actuator Steppers

The single-actuator case, with twice the friction force as the two-actuator case, is equivalent to the two-actuator case with a phase-shift ratio of zero, $\phi = 0$. The response of the two-actuator system is compared to the single actuator case in Fig. 3.13, which shows the oscillations for the single actuator case, and the suppression of oscillations in the two-actuator case once the transients decay.

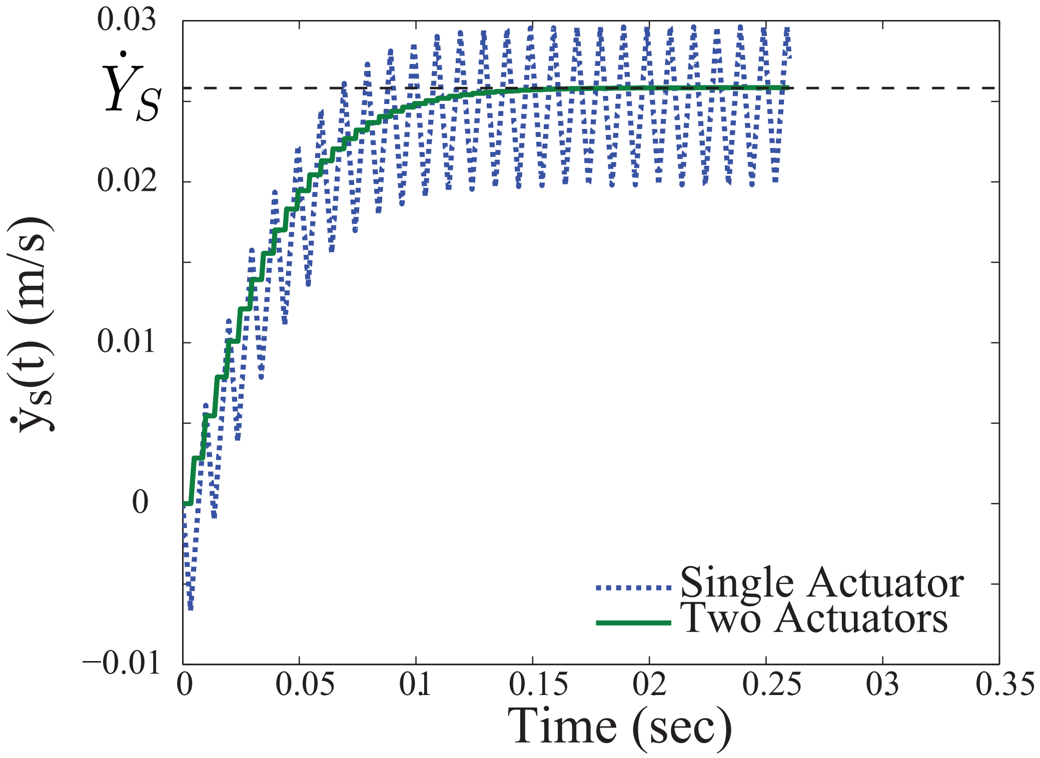

Figure 3.13: The stage velocity, $\dot{y}_s(t)$, of a single actuator system (dotted) has oscillations around a steady-state value while the oscillations in the stage velocity of the two actuator system are suppressed. The system reaches a constant stage velocity of $\dot{Y}_S$.

3.4.4 Control of the Stage Velocity

For the non-oscillatory steady-state case, i.e., when the phase-shift ratio $\phi = 1/2$, the amplitude of the piezo-tip displacement, $y_{p,max}$, was varied over the range (125μm $-$ 250μm) while keeping the frequency fixed at 100 Hz. The resulting steady-state velocities are shown in Fig. 3.14. Similarly, for a fixed piezo-displacement amplitude of 200μm the waveform frequencies were varied up to the first resonance frequency, ω_1, and the resulting steady-state velocities are shown in Fig. 3.14. From Fig. 3.14(left), it can be seen that varying the amplitude of the piezo-tip displacement allows a range of velocities to be obtained with the maximum velocity being only limited by the maximum voltage that can be applied to the piezoelectric actuator. Moreover, the stage velocity, $\dot{y}_s(t)$, increases with increasing frequency. These variations can be used, in future studies, to develop closed loop control strategies for the stepper.

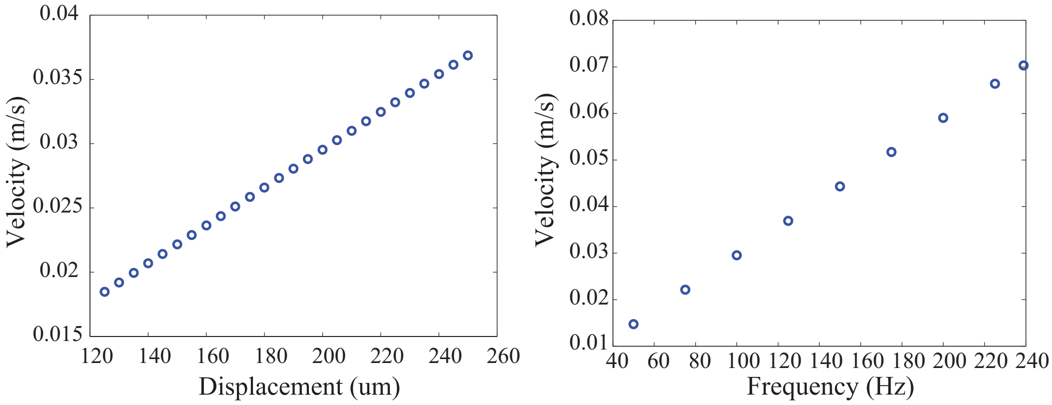

Figure 3.14: A range of velocities for the motion stage can be achieved by varying the piezo amplitude (left), $y_{p,max}$ and the frequency of the piezo motion (right), $1/f_{dw}$.

3.4.5 Future Work

The inputs generated, $V_p(t)$, are created under steady-state conditions. If the initial condition is different from that of the steady-state, then the friction forces will be different and therefore the pre-computed input (with steady-state initial condition) will not lead to exact compensation for the friction forces. The error generated due to this deviation in the input needs to be investigated further.

Further, the Poincaré map presented is generated numerically, therefore, some small oscillations may be found around the fixed point that are not represented due to computational limitations. Therefore, an analytical approach is needed to investigate the potential existence and size of chaotic or periodic motion about the fixed point.

3.5 Conclusions

The main contribution of this article was to show that, when compared to single actuator stepper system, the response of multi-actuator stepper systems can be significantly less oscillatory and these reduced oscillations allow for higher precision velocity control of a motion stage. The simulation results presented here show that a range of steady-state velocities are achievable by changing both the amplitude and frequency of the piezo motion and that the resulting steady-state responses are stable.

Chapter 4

EXPERIMENTAL SETUP AND RESULTS

4.1 Introduction

With the vibration suppression modeled in Chapter 3, an experimental setup was designed and tested to look into the modeling and control of stepper systems and how the vibrations are introduced into the system.

4.2 Experimental Setup

The experimental setup is made up of 3 parts: (i) a structure to hold the two piezos as well as sensors, (ii) the hardware used to drive the system as well as support the sensor system, and (iii) the software used to generate the inputs to the piezos and collect data from the sensors.

4.2.1 Structure

The base of the stepper system was designed as a compact structure with several design requirements. The first requirement is that the stage is fully supported by the actuator system, thus removing the need for a bearing system. The addition of even the best mechanical bearing system introduces a small amount of external friction ($\mu_k \approx 0.001$) which causes oscillations in the steady-state velocity.

The second requirement is that the structure can hold two piezoelectric actuators and multiple sensor configurations. This will allow measurements of the piezo-tip displacements y_i $(i = 1, 2)$ as well as the motion stage displacement y_s depending on the the locations of the sensors during the current measurement.

The third requirement is that the structure is rigid enough to withstand the high frequency motion of the actuators. This is critical as the sensors are mounted in the same structure as the actuators so any motion of the structure will lead to measurement errors. (See Appendix C for a design that this became an issue in.)

The current design of the structure is shown in in Fig. 4.1. The design allows the stage to move above the actuators without a bearing system, can hold sensors for actuator and stage measurement, and is relatively flat to prevent vibrations due to a cantilevered structure.

To minimize the effect of external (i.e. ground) vibrations on the system, the structure

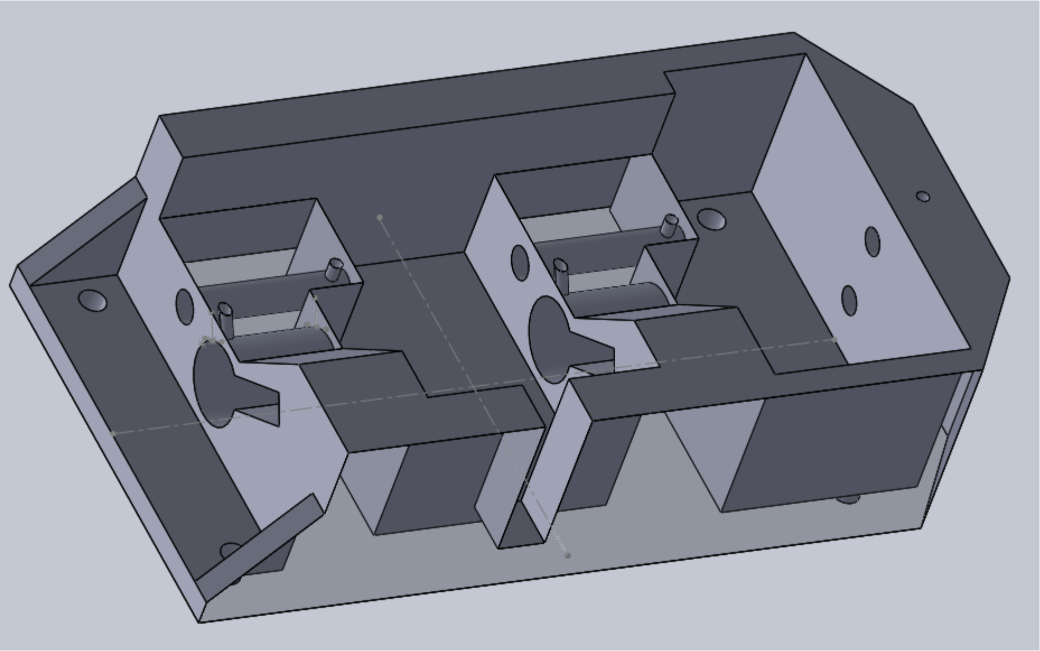

Figure 4.1: CAD representation of the stepper structure to hold both the actuators and the sensors while allowing the stage to move freely.

was placed on an isolation platform constructed of rubber tubing and iron plates and then placed on a heavy lab bench. The actual experimental setup is shown in Fig. 4.2 and was milled out of 6061 aluminum.

Piezoelectric Actuators

The piezos used in the stepper are PA 16/14 SG actuators from Piezosystem Jena. These are pre-loaded stack actuators and have an operating range of $0\mu m$ to $17\mu m$ with an input voltage range of $-20V$ to $130V$.

Sensors

The sensors used are Kaman SMU-9000 Inductive sensors with a calibrated measurement range of $50\mu m$. These are non-contact sensors such that they will not interfere with the

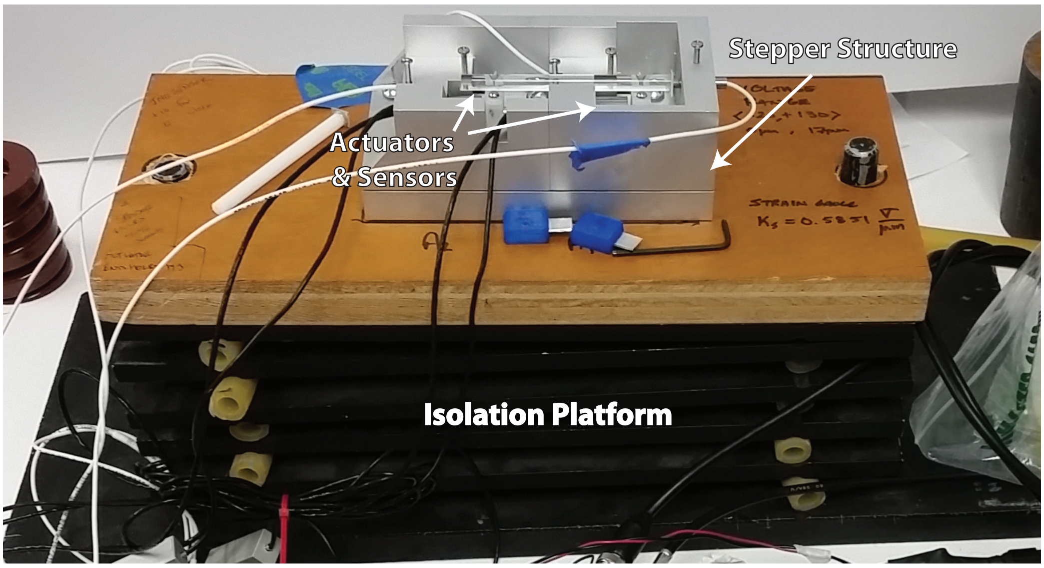

Figure 4.2: Experimental setup with the stepper structure on an isolation platform. The isolation platform was used to reduce any effects on the system due to ground vibrations and is comprised of rubber tubing and iron plates. The stepper system was milled out of aluminum for a more rigid structure.

motion of the piezos or the stage. They are used simultaneously on both piezos and the stage.

To measure the piezo motion, a target plate is attached to the piezo-tip and the sensor is mounted parallel to the actuator approximately $25\mu m$ from the target plate. To measure the stage motion, the sensor is mounted inline with the stage. As the stage moves towards the sensor, it enters the measurement range until it makes contact with the sensor (see Fig. 4.3).

4.2.2 Hardware

To obtain measurements from the stepper system and generate input signals to the piezos, a NI-6211 Multifunction USB Data Acquisition (DAQ) block (from National Instruments) passed through a signal conditioning circuit (for measurment) and a HP-6825A amplifier

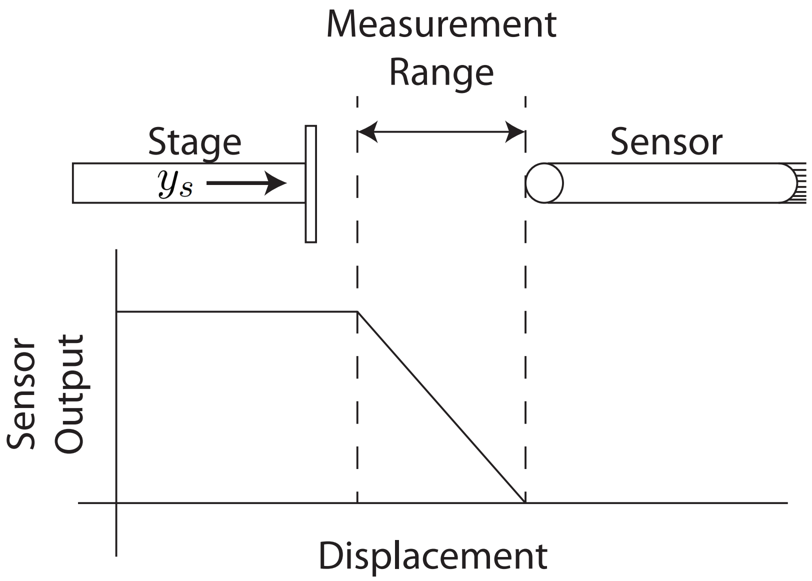

Figure 4.3: An inductive sensor was used to measure the displacement of the motion stage y_s. The sensor gave a maximum reading until the stage moved into the measurement range. As the stage approaches the sensor, a linear decrease in the sensor reading occurs until the stage makes contact with the sensor and produces the minimum reading.

(for input signals, $\pm 20V$). The DAQ allowed two analog outputs to be generated at 200khz and four channels of analog input at 50khz to be measured (up to 16 channels, 250khz aggregate sampling). This configuration allowed both driving signals for the piezos to be generated while the measurements of the piezo and stage displacements from the inductive sensors are collected. The trajectories used in Chapters 3 and 4 are sufficiently smooth to ensure the power system (DAQ/amplifier/power supply) are not strained which will allow the correct inputs to be sent to the piezos.

Measurement

To ensure clean measurements from the inductive sensors, a amplifier and bias circuit were used (diagram in Fig. 4.4) when measuring the piezo motion. When measuring the stage motion, the raw sensor signal was used. This allowed the full range of the ADC in the DAQ to be used to provide better resolution of the measurements.

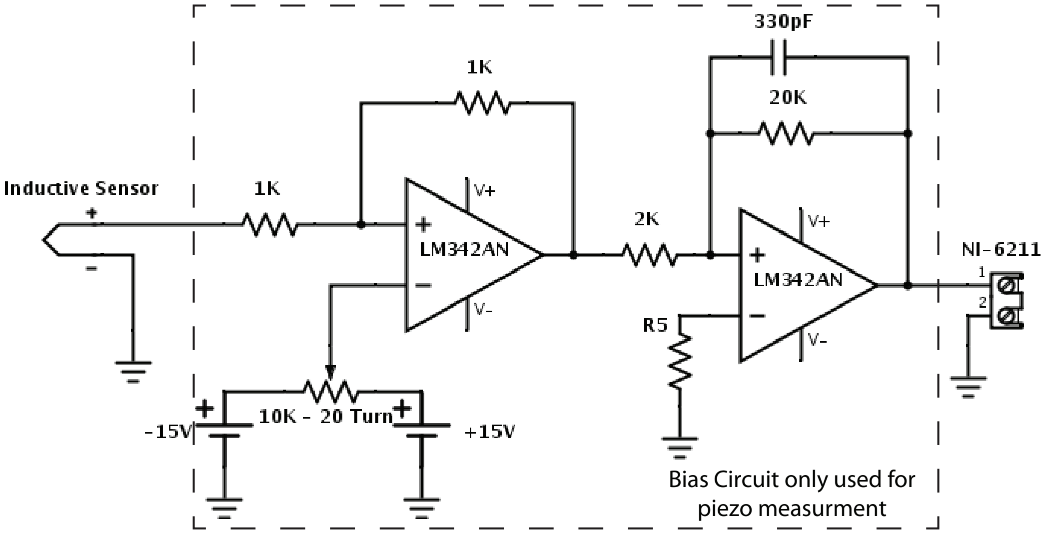

Figure 4.4: Bias and amplifier circuit for inductive sensor measurements. The circuit was bypassed when the sensor was measuring the stage motion.

To prevent noise and ground loop issues, a buffer circuit was used in the measurement of the inputs which is shown in Fig. 4.5.

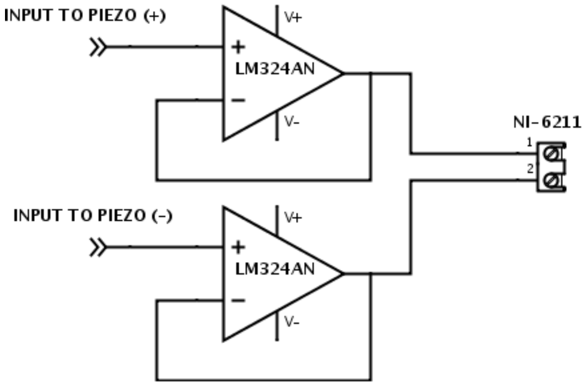

Figure 4.5: Buffer circuit to reduce ground loop issues in the measurement of the inputs.

4.2.3 Software

Measurements and signal generation were done using LabVIEW 2013 along with the NI-6211 DAQ. The analog input signals were generated at 200khz sampling and were read from text files generated in MATLAB then repeated periodically. MATLAB was used to write the text files containing the inputs for each piezo. This allowed the measurements to be taken without having to do signal computation simultaneously. The MATLAB and LabVIEW code can be seen in Appendix A and Appendix B, respectively.

4.3 Optimal Inversion for Piezo Tracking

To determine the correct input signals for the piezos, feedforward methods were used. Previously, model-based feedforward techniques were performed with good results [29]. However, the dynamics of the current piezos are more complex so optimal inversion (as developed in [44]) was implemented.

4.3.1 Piezo Models

To determine the optimal inverse for each piezo, the dynamics of the piezos needs to be determined. Towards this, frequency responses of each actuator were found using a Stanford Research Systems Dynamic Signal Analyzer. The output of the piezos due to a swept sinusoidal waveform input for frequencies from 500hz to 10khz were collected. The frequency responses for each actuator are shown in Fig 4.6 where $G_{11}(\omega)$ is the response of the first piezo and $G_{22}(\omega)$ is the response of the second piezo.

4.3.2 Coupling Effect Due to Structural Vibrations

With both actuators in the same structure, as the driving frequency f_{dw} increases, there is some mechanical coupling between the piezos and the structure that begins to influence the dynamics of the piezos therefore influencing the stage motion. The coupling responses $G_{12}(\omega)$ and $G_{21}(\omega)$ are shown in Fig. 4.7 where $G_{ij}(\omega)$ $(i \neq j)$ is the response of the i^{th} piezo due to an input to the j^{th} piezo.

With the frequency responses for both the piezo dynamics ($G_{11}(\omega)$ and $G_{22}(\omega)$) as well

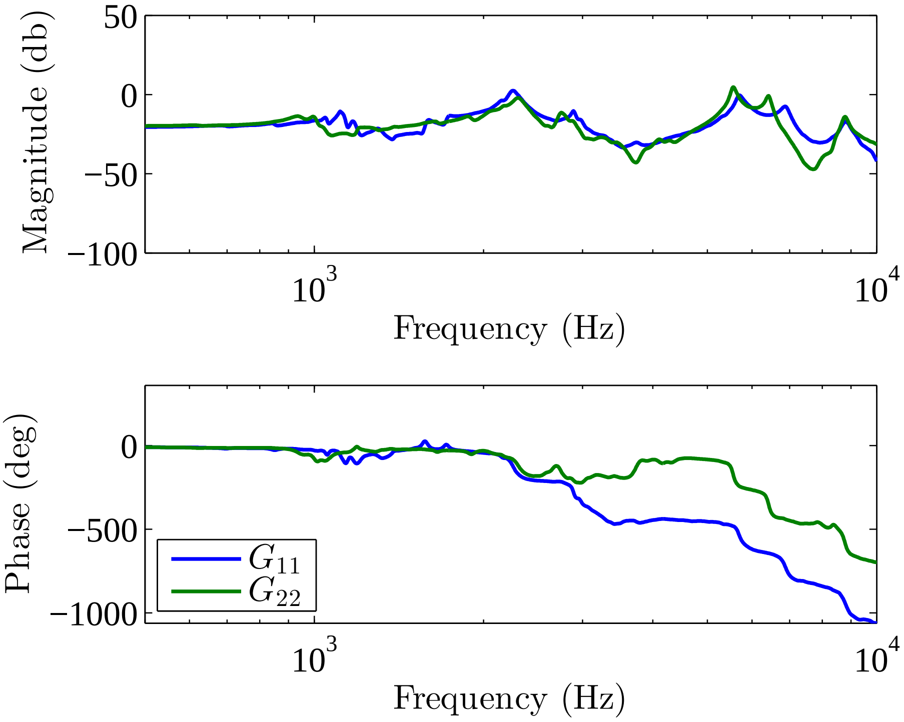

Figure 4.6: Frequency response of the piezos G_{11} and G_{22} with inputs u_1 and u_2, respectively.

as the coupling dynamics ($G_{12}(\omega)$ and $G_{21}(\omega)$), the optimal inverse inputs $u_{opt,i}(\omega)$ $(i = 1, 2)$ can be generated. Following the optimal inversion methods in [30], the optimal inverse for the i^{th} actuator $u_{opt,i}(\omega)$ is

$$u_{opt,i}(\omega) = G^{-1}_{opt,ii}(\omega)y_i(\omega) + G^{-1}_{opt,ij}(\omega)y_j(\omega) \tag{4.1}$$

where $i \neq j$, $y_i(\omega)$ is the Fourier transform of the desired piezo-tip displacement $y_i(t)$, and $G^{-1}_{opt,ij}(\omega)$ is the optimal inverse frequency response defined as

$$G^{-1}_{opt,ij}(\omega) = \frac{G^*_{ij}(\omega)Q((\omega)}{R(\omega) + G^*_{ij}(\omega)Q((\omega)G_{ij}(\omega)}. \tag{4.2}$$

The weights, $Q(\omega)$ and $R(\omega)$, are from the quadratic cost function J (minimized by the

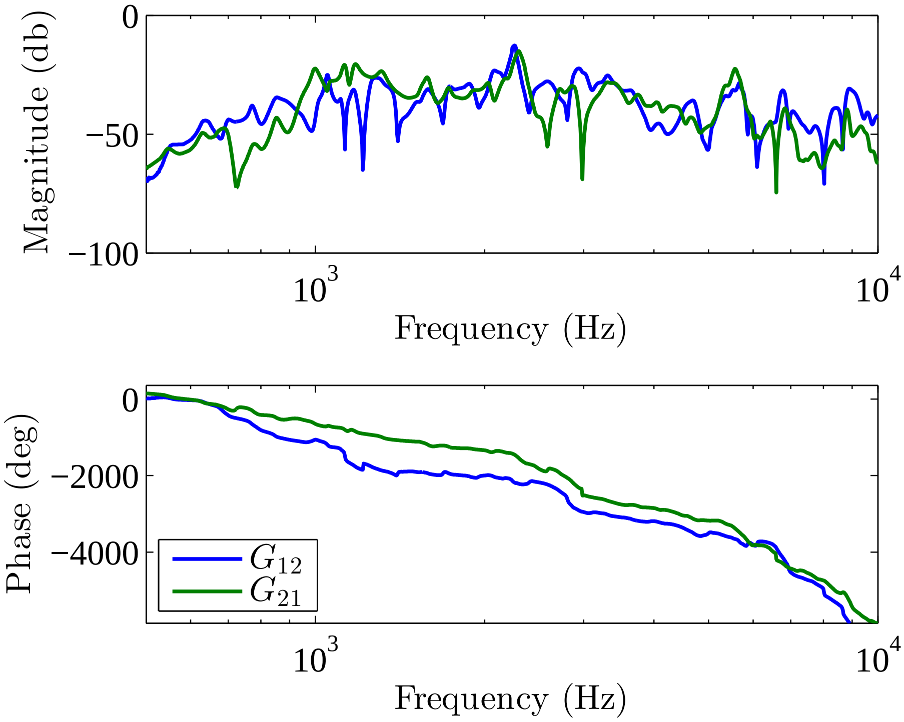

Figure 4.7: Frequency response of the coupling dynamics G_{12} and G_{21} with inputs u_2 and u_1, respectively.

optimal input $u_{opt,i}(\omega)$, similar to linear-quadratic-regulator problems) defined as

$$J = \int_{-\infty}^{\infty} u^*_{opt,i}(\omega)R(\omega)u_{opt,i}(\omega) + e^*_i(\omega)Q(\omega)e_i(\omega)\ d\omega \tag{4.3}$$

where $e_i(\omega)$ is the Fourier Transform of the tracking error $e_i(t) = y_i(t) - y_{meas}(t)$ of the i^{th} piezo.

By adjusting the weights, $Q(\omega)$ and $R(\omega)$, the optimal inverse can be used to penalize specific frequencies ω. For example, when tracking a lower frequency trajectory, a common approach is to use $Q(\omega) > R(\omega)$ for low frequencies to penalize tracking errors on low frequency components and $R(\omega) > Q(\omega)$ for high frequencies to penalize high frequency inputs.

Comparing the frequency responses in Fig. 4.6 and Fig. 4.7, as the frequency becomes larger, the coupling between the piezos gets stronger and the phase difference between the piezos starts to change, therefore the weights $Q(\omega)$ and $R(\omega)$ were used to reduce the effect of frequencies $\omega > 3kHz$ to minimize the excitation of these frequencies.

4.4 Experimental Results

Two types of experiments were performed: (i) single input mode where the driving waveforms $\dot{y}_i$ $(i = 1, 2)$ were the same (i.e. $\dot{y}_1(t) = \dot{y}_2(t)$) and (ii) dual input mode where a half period phase shift $\phi = 1/2$ was introduced between the driving waveforms $\dot{y}_i$ $(i = 1, 2)$ such that $\dot{y}_2(t) = \dot{y}_1(t + \phi\tau_p)$ where τ_p is the period of the driving waveforms $\dot{y}_i$ $(i = 1, 2)$. The experimental results shown here are related to a driving frequency $f_{dw} = 500\ Hz$ and a maximum deflection of the piezo $y_{p,max} = 3\mu m$. These were chosen to ensure that the stage would move while staying away from large voltages that could damage the piezos.

4.4.1 Dual Input: $\dot{y}_2(t) = \dot{y}_1(t + \phi\tau_p)$

The dual input mode uses the phase-shifted driving waveforms $\dot{y}_i$ $(i = 1, 2)$ developed in [35]. These inputs are designed to suppress the oscillations found in stepper systems (discussed in Chapter 3).

The input $u_{opt,i}(t)$ for each piezo $(i = 1, 2)$ is generated by taking the inverse Fourier transform of the frequency domain inputs in (4.1). To ensure that no transient behavior was included in the inputs $u_{opt,i}(t)$, pre and post actuation time was used to build a larger input of which a subset was taken out and used in the experimental system. The inputs sent to the piezos are in Fig. 4.8. The full optimal inverse with pre and post actuation is in Appendix D.

With the inputs from Fig. 4.8, experiments were conducted measuring both of the piezo-tip displacements y_i $(i = 1, 2)$ as well as the motion of the stage y_s. An example set of experimental results is shown in Fig. 4.9.

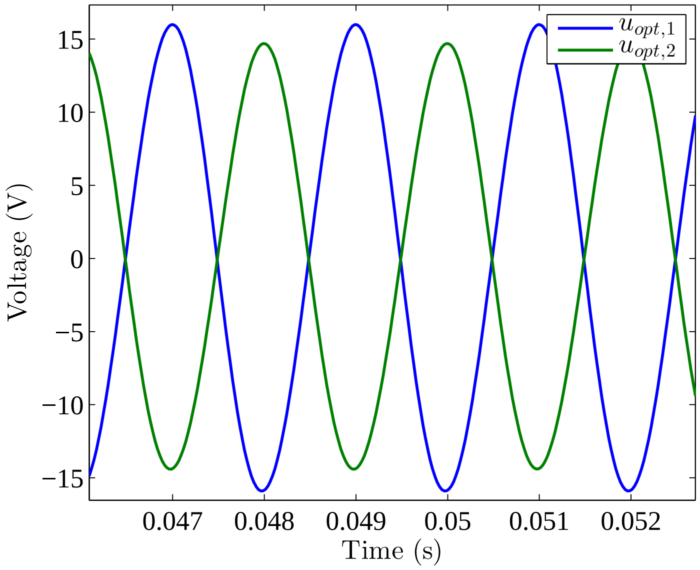

Figure 4.8: Inputs generated using the optimal inverse (4.1) for the dual input mode. The piezo-tip displacement of the second piezo y_2 is shifted by half a period $\phi = 1/2$ from the piezo-tip displacement of the first actuator y_1.

4.4.2 Single Input: $\dot{y}_1(t) = \dot{y}_2(t)$

With the work discussed in Chapter 2 concerning a single actuator system, a set of experiments were performed that re-create a similar stepper system. This was done by allowing the phase shift $\phi = 0$ between the piezo-tip displacements y_i $(i = 1, 2)$ such that $\dot{y}_1(t) = \dot{y}_2(t)$.

Using the optimal inverse (from (4.1)) to generate the inputs $u_{opt,i}$ $(i = 1, 2)$ for each piezo (see Fig. 4.10), experiments were performed with the stepper operating in single mode. An example set of experimental results for the single mode inputs is shown in Fig. 4.11.

As expected, the magnitude of the oscillations in the position is larger when the stepper system is operating in single mode when compared to dual mode. The velocities ($\dot{y}_i$ $(i = 1, 2)$ and $\dot{y}_s$) are found by differentiating the measurements shown in Fig. 4.9 and Fig. 4.11. The velocities are shown in Fig. 4.12.

The oscillations with the stepper in single mode have a peak to peak magnitude of

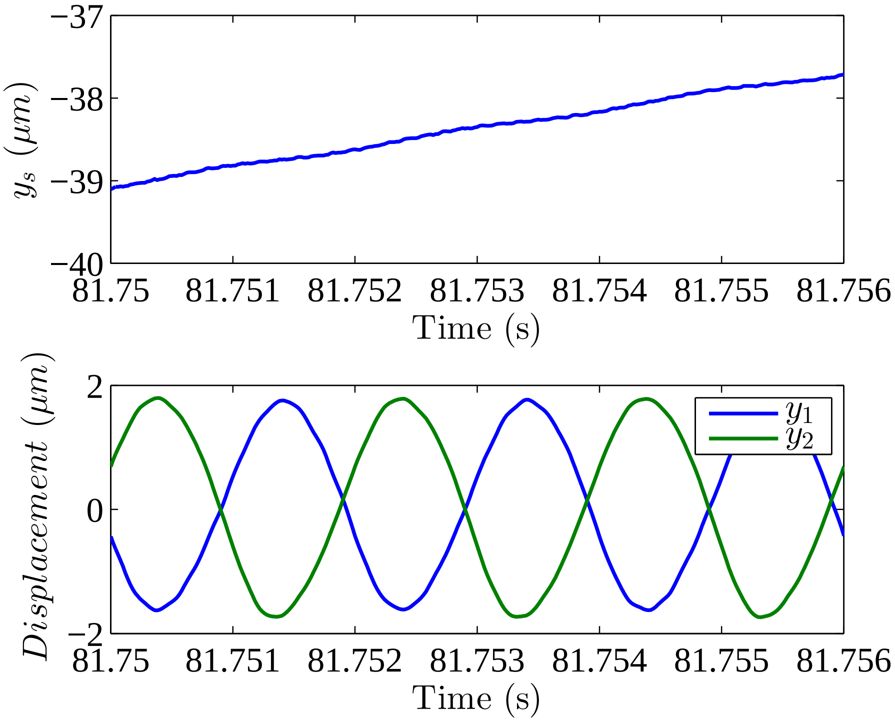

Figure 4.9: (Top) The resulting stage motion y_s due to the periodic inputs $u_{opt,i}$ $(i = 1, 2)$ to the piezos. (Bottom) The resulting piezo-tip displacements due to the periodic inputs $u_{opt,i}$ $(i = 1, 2)$ to the piezos.

$\approx 1300\mu m/s$. With the stepper in dual mode, the peak to peak oscillation magnitude is $\approx 500\mu m/s$. Thus a reduction of oscillations of $\approx 62\%$ is observed using the dual mode compared to the single mode.

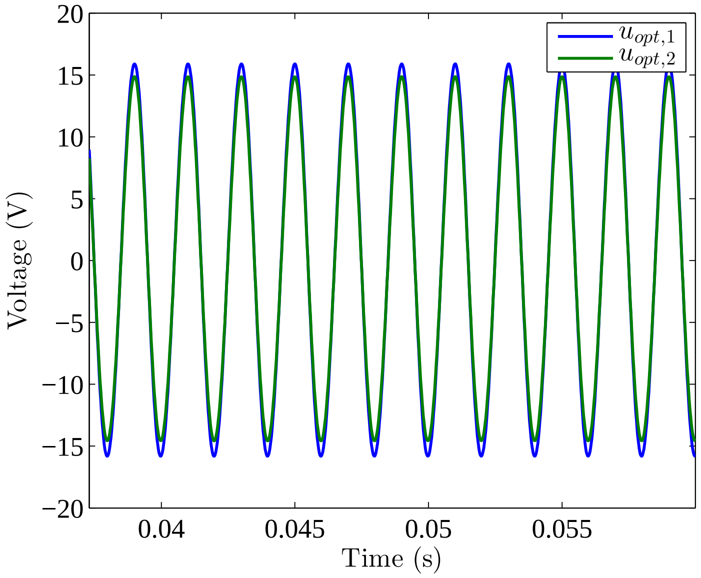

Figure 4.10: Inputs generated using the optimal inverse (4.1) for the single input mode. The trajectories for both piezos are the same such that $y_1 = y_2$.

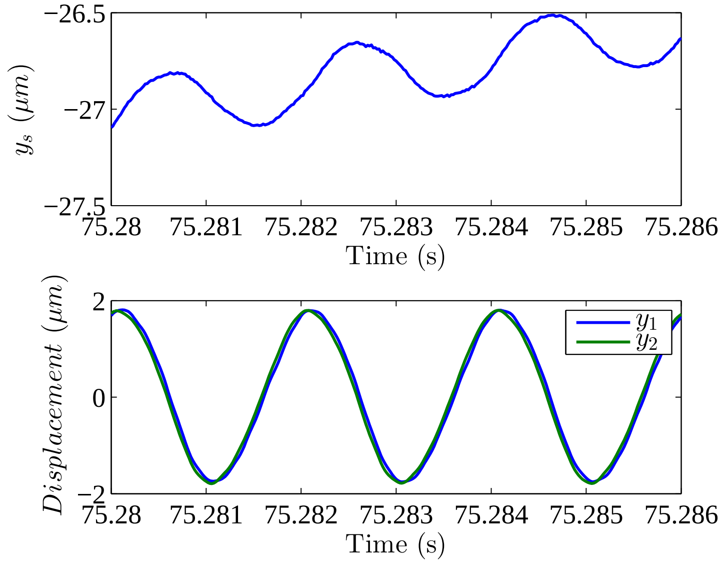

Figure 4.11: (Top) Motion of the stage y_s due to the single mode inputs shown in Fig. 4.10. Note, when compared to Fig. 4.9, the oscillations are more pronounced. (Bottom) Motion of the piezos y_i $(i = 2, 2)$ due to the single mode inputs shown in Fig. 4.10.

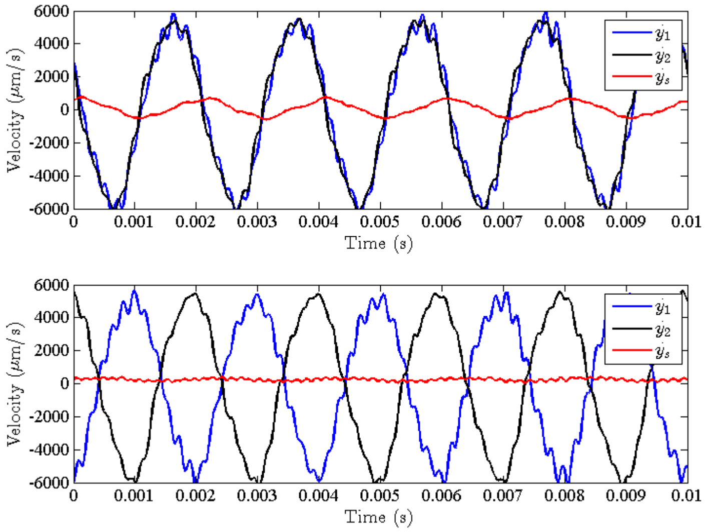

Figure 4.12: (Top) Velocities of the piezos ($\dot{y}_i$ ($i = 1, 2$) and the stage $\dot{y}_s$ with the stepper in single mode. (Bottom) Velocities of the piezos ($\dot{y}_i$ ($i = 1, 2$) and the stage $\dot{y}_s$ with the stepper in dual mode. Comparison of the oscillation size for both experiments yields $\approx 62\%$ reduction in oscillation magnitude.

Chapter 5

CONCLUSIONS

The research presented in this dissertation presented a method to solve the fundamental problem using stick-slip devices, including steppers, in which the output velocity has oscillations induced by the stepping behavior. This dissertation addressed three issues: (i) the stability and control of a single piezoelectric actuator (piezo) stepper system, (ii) the suppression of velocity oscillations found in stepper systems, and (iii) the design and test of a new two piezo stepper system.

To determine the stability of the stepper systems, a Poincaré map approach was used. However, due to the dynamics of the system, the Poincaré map approach needed to be extended to evaluate the stability in the presence of discontinuities. Additionally, the presence of oscillations was shown for any single actuator stepper system, therefore improvements were needed.

To suppress the oscillations found in the stepper systems, a new stepper system was designed. In this new design, a second piezo was introduced and a method for creating out-of-phase trajectories that will allow constant velocities to be achieved was presented.

Finally, this dissertation presented an experimental setup of the new stepper system. Results show $\approx$ 62% suppression in oscillation magnitude when using the out-of-phase trajectories when compared to a single actuator configuration.

Future work to extend this research to achieve constant stage velocities could include: implementing feedback into the piezos to achieve improved tracking performance yielding improved friction response, improved materials selection criteria, wear monitoring, stage design, the addition of extra contacts to reduce stage rotation, constrained trajectory design, and structural adaptations to allow for fine-tuning of the piezo alignment.

BIBLIOGRAPHY

[1] C. Schmitt, J.-M. Breguet, A. Bergander, and R. Clavel. Stick and slip actuators. *Proceedings of SPIE: Microrobotics and Microassembly*, 4194:65–74, November, 2000.

[2] D. Jeon and R. F. Willis. Inchworm controller for fine approach in a scanning tunneling microscope. *Journal of Vacuum Science and Technology A*, Jul/Aug, A-9 (4):2418–2419, 1991.

[3] Roel J E Merry, Joep L Holierhoek, Marinus J G Van De Molengraft, and Maarten Steinbuch. Gain Scheduling Control of a Walking Piezo Actuator. *IEEE/ASME Trans. on Mechatronics*, pages 1–9, 2013.

[4] J.M. Bergander, A and Breguet. Performance Improvements for Stick-Slip Positioners. pages 59–66, 2003.

[5] S. Devasia, E. Eleftheriou, and S. O. Reza Moheimani. A survey of control issues in nanopositioning. *IEEE Transactions on Control Systems Technology*, 15(5):802–823, Sept, 2007.

[6] Hassan K. Khalil. *Nonlinear Systems 3rd Edition.* Prentice Hall, 2002.

[7] W. Hanh. *Stability of Motion.* Springer-Verlag, 1967.

[8] D.W. Pohl. Dynamic piezoelectric translastion device. *Review of Scientific Instruments*, 58(1):54–57, January, 1987.

[9] Toshiro Higuchi, Yusof Hojjat, and Masahiro Watanabe. Micro Actuators Using Recoil of Ejected Mass. *IEEE Mirco Robots and Teleoperators*, pages 401–405, November 1987.

[10] T. Higuchi, Y. Yamagata, K. Furutani, and K. Kudoh. Precise positioning mechanism utilising rapid deformations of piezoelectric elements. *IEEE Mirco Electro Mechanical Systems*, pages 222–226, February, 1990.

[11] Jack Judy, Dennis Polla, and William Robbins. Experimental model and IC-Process design of a nanometer linear piezoelectric stepper motor. *Microstructures, Sensors, and Actuators*, 19:11–17, November, 1990.

[12] A. Bergander, J-M Breguet, C. Schmitt, R. Clavel, and H. Bleuler. Piezoactuators for motion control from centimeter to nanometer. *IEEE International Conference on Intelligent Robots and Systems*, 2000.

[13] Yingchun Zhang, Guangjun Liu, and Juergen Hesselbach. On development of a rotary-linear actuator using piezoelectric translators. *IEEE-ASME Transactions on Mechatronics*, 11(5):647–650, OCT, 2006.

[14] Sang-Chae Kim and Soo Hyun Kim. Precise rotary motor by inchworm motion using dual wrap belts. *Review of Scientific Instruments*, 70(5):2546–2550, May, 1999.

[15] Q. Zou, C. Vander Giessen, J. Garbini, and S. Devasia. Precision tracking of driving waveforms for inertial reaction devices. *Review of Scientific Instruments by the American Institute of Physics*, 76(2):Article No. 023701 (Pages 1–9), February 2005.

[16] Robert Chave and Christian Lindensmith. Nasa tech briefs. pages NPO–20153, 1999.

[17] Robert Chave. Nasa tech briefs. pages NPO–20270, 1999.

[18] J. C. Fasick. An inchworm actuator for the next generation space telescope. Technical report, Burleigh Instruments, Inc., Fishers, NY, oct 1998.

[19] L. Howald, H. Rudin, and H. J. Guntherodt. Piezoelectric inertial stepping motor with spherical rotor. *Review of Scientific Instruments*, 63(8):3909–3912, Aug, 1992.

[20] R. Stibitz. Incremental feed mechanisms. *U.S. Patent*, 1964.

[21] Bi Zhang and Zhenqi Zhu. Developing a linear piezomotor with nanometer resolution and high stiffness. *IEEE/ASME Transactions on Mechatronics*, 2(1), March:22–29, 1997.

[22] K Uchino. *Piezoelectric Actuators and Ultrasonic Motors.* Kluwer Academic Publishers, 1997.

[23] Kyu-Jin Cho and Je-Sung Koh. Omega-shaped inchworm-inspired crawling robot with large-index-and-pitch (lip) SMA spring actuators. *IEEE/ASME Transactions on Mechatronicx*, 18(2):419–429, Apr, 2013.

[24] Roel J. E. Merry, Niels C. T. De Kleijn, and Marinus J. G. Van De Molengraft. Using a walking piezo actuator to drive and control. *IEEE/ASME Transactions on Mechatronics*, 14:21–31, 2009.

[25] Roel Merry, Ren van de Molengraft, and Maarten Steinbuch. Modeling of a walking piezo actuator. *Sensors and Actuators A: Physical*, 162(1):51–60, 2010.

[26] Roel J. E. Merry, Martijn G. J. M. Maassen, Marinus Ren, Nathan Van de Wouw, and Maarten Steinbuch. Modeling and waveform optimization of a nano- motion piezo stage. *IEEE/ASME Transactions on Mechatronics*, 16(4):615–626, 2011.

[27] Won-jong Kim and Yi-chu Chang. Aquatic ionic-polymer-metal-composite insectile robot with multi-DOF legs. *IEEE/ASME Transactions on Mechatronics*, 18(2):547–555, April, 2013.

[28] Takuro Ikeda. *Fundamentals of Piezoelectricity.* Oxford Science Publications, 1990.

[29] S. Wilcox and S. Devasia. Stability and velocity control for a piezoelectric stepper. *IEEE Trans. on Mechatronics*, 2015.

[30] G. M. Clayton, S. Tien, K. K. Leang, Q. Zou, and S. Devasia. A review of feedforward control approaches in nanopositioning for high speed SPM. *ASME Jounrnal of Dynamic Systems, Measurement and Control, Special Issue on Dynamic Modeling, Control and Manipulation at the Nanoscale*, 131(6):1–19, Nov, 2009.

[31] B Bhikkaji, M Ratnam, Andrew J Fleming, and S O Reza Moheimani. High-Performance Control of Piezoelectric Tube Scanners. 15(5):853–866, 2007.

[32] Timothy Smith and Kirby Lester. Methods and apparatus for controlling the feed rate of a discrete object sorter/counter. *U.S. Patent*, 1995.

[33] Ettlinger Jr. R., W. Schneider, and Avant Industries Inc. Vibrating sorter for soiled tableware. *U.S. Patent*, 1971.

[34] Kenji Uchino. Piezoelectric ultrasonic motors: overview. *Smart Materials and Structures*, 7(3):273–285, June 1998.

[35] S. Wilcox and S. Devasia. Precision control through vibration suppresion in piezoelectric-stepper response. In *Proceedings of the ASME Dynamic Systems and Control Conference*, Palo Alto, CA, Oct 2013.

[36] N. Shimizu, T. Kimura, T. Nakamura, and I. Umebu. An ultrahigh vacuum scanning tunneling microscope with a new inchworm mechanism. *Journal of Vacuum Science and Technology A*, 8(1):333–335, 1990.

[37] L Meirovitch. *Fundamentals of Vibrations.* McGraw Hill, 2001.

[38] T.S. Low and W. Guo. Modeling of a three-layer piezoelectric bimorph beam with hysteresis. *Journal of Microelectromechanical Systems*, 4(4):230–237, 1995.

[39] N. B. Haaser and J. A. Sullivan. *Real Analysis.* Dover, New York, 1991.

[40] M. Arafa, O. Aldraihem, , and A. Baz. Modeling and characteriziation of a linear piezomotor. *Journal of Intelligent Material Systems and Structures*, 20(16):1913–1921, 2009.

[41] E. Shamoto and T. Moriwaki. Development of a "Walking Drive" ultraprecision positioner. *Precision Engineering*, 6359(97):85–92, 1997.

[42] Peter Eaton and Paul West. *Atomic Force Microscopy.* Oxford University Press, 2010.

[43] Greg Haugstad. *Atomic Force Microscopy: Understanding Basic Modes and Advanced Applications.* Wiley, 2012.

[44] J. Dewey, K. Leang, and S. Devasia. Experimental and theoretical results in output-trajectory redesign for flexible structures. *ASME Journal of Dynamic Systems, Measurement, and Control*, 120(4):446–461, 1998.

Appendix A

MATLAB CODE

A.1 Trajectory Generation

```
% Function to Create Trajectories
% y=TrajFun_5th(Freq,Skew,Kdc,dt)
% Output y is [Postion
%              Velocity
%              Acceleration
%              Time]
%
% Freq is the Frequency(Hz) of the Desired Trajectory
% Skew is the percentage of skew of the trajectory (50 is
  symmetric)
% Delta is the Maximum Displacement of the Position Trajectory
% dt is the time step

function y=TrajFun_5th(Freq,Skew,delta,dt)

Skew=Skew/100;

% Positive Time Edge
Tp = (1-Skew)*1/Freq;

% Negative Time Edge
Tn = -Skew/Freq;

% Negative Time Vector
tn = 0:-dt:Tn;

% Reverse the Time vector to get the negative time values
```

```
tn = fliplr(tn);

% Positive Time Vector (DOESN'T START AT ZERO!)
tp = dt:dt:Tp;

% Create Total Time Vector
t = [tn tp];

% Create the Data Vector
y=zeros(4,max(size(t)));

% The Boundary Condition Matrix
Am=[ Tp^5     Tp^4     Tp^3    Tp^2     0          0        0
   0;
    Tp^5     Tp^4     Tp^3    Tp^2    -(Tn^5)    -(Tn^4)   -(Tn^3)
       -(Tn^2);
    5*Tp^4  4*Tp^3   3*Tp^2   2*Tp   -5*(Tn^4)   -4*(Tn^3)  -3*(Tn
       ^2) -2*Tn;
    20*Tp^3 12*Tp^2 6*Tp     2     -20*(Tn^3) -12*(Tn^2)  -6*Tn
       -2;
    60*Tp^2 24*Tp     6       0      -60*(Tn^2) -24*Tn    -6
       0;
    0         0        0    2         0          0       0       -2;
    0         0        6    0         0          0      -6        0;
    5*Tp^4  4*Tp^3   3*Tp^2   2*Tp     0          0       0        0];

% The solution Matrix - The -1 is what causes output position
   height
b=[-1 0 0 0 0 0 0 0]';
```

```
% The Coefficient Vector
coeff=Am\b;

% Grab all the Coefficients
ap=coeff(1);
bp=coeff(2);
cp=coeff(3);
dp=coeff(4);
an=coeff(5);
bn=coeff(6);
cn=coeff(7);
dn=coeff(8);

% Positive Time Polynomials
Pp=ap*tp.^5+bp*tp.^4+cp*tp.^3+dp*tp.^2;
Vp=5*ap*tp.^4+4*bp*tp.^3+3*cp*tp.^2+2*dp*tp;
Ap=20*ap*tp.^3+12*bp*tp.^2+6*cp*tp+2*dp;

% Negative Time Polynomials
Pn=an*tn.^5+bn*tn.^4+cn*tn.^3+dn*tn.^2;
Vn=5*an*tn.^4+4*bn*tn.^3+3*cn*tn.^2+2*dn*tn;
An=20*an*tn.^3+12*bn*tn.^2+6*cn*tn+2*dn;

% Join the negative and positive time polynomials
p=[Pn Pp];
v=[Vn Vp];
a=[An Ap];
```

```
% Shift the time vector
t=t-Tn;

% Create the function output
y=[p;
   v;
   a;
   t];



% figure(1)
% subplot(311), plot(t,p)
% subplot(312), plot(t,v)
% subplot(313), plot(t,a)

% sys_int = ss([0],[1],[1],[0]);
% [vint,ttsys,Xsys] = lsim(sys_int,a,t,[v(1)]);
% [yint,ttsys,Xsys] = lsim(sys_int,v,t,[p(1)]);

% figure(2)
% subplot(311), plot(t*1000,p,'g',t*1000,yint,'r')
% xlabel('time(ms)'); ylabel('position'); legend('original','
    integrated')
% grid
% subplot(312), plot(t*1000,v,'g',t*1000,vint,'r')
% xlabel('time(ms)'); ylabel('velocity'); legend('original','
    integrated')
% grid
% subplot(313), plot(t*1000,a)
```

```
% xlabel('time(ms)'); ylabel('acceleration'); grid
% title('polynomial case')
```

A.2 Matlab Code for Chapter 2

A.2.1 Piezo Variables

```
function Piezo(K_dc,wn)

% Piezoelectric Properties Management File
% Calculates the requied variables needed
% Give (K_dc,wn) as input variables

global L I Thick Width AP Kp d31 p Mt Ml Mb g beta1L beta1 E
   EI sigma1
global FunXofL1 FunSQ1 X1_bar X1_sq XL1 dXL1 K_1 K_2 K_3 K_31
   K_32

L=28.6e-03; %m
Thick=0.51e-03; %m
Width=12.7e-03; %m
AP=Thick*Width; %m^2
I=(Width*(Thick)^3)/12; % m^4

Kp=K_dc; % Piezo Actuator Gain

%Piezoelectric Strain Coefficient in the 3-1 plane
d31=Kp*(Thick^2)/(3*L^2)*1.12;

%Material Properties
p=7600; %kg/m^3
```

```
Mt=27.64*10^-3; %kg
Ml=2.81*10^-3; %kg
Mb=Mt-3*Ml; %kg
g=9.81; %m/s^2

%Beta_n's from Beam Equation
beta1L=1.875;
beta1=beta1L/L;
% syms x

%Solution for omega1 from Beam Equation
E=(((wn/3.5160)^2)*p*AP*L^4)/I; %pa
EI=E*I;
%

syms x
%Create the X(x) Function to obtain constants (Normalized)
sigma1=(sin(beta1L)+sinh(beta1L))/(cos(beta1L)+cosh(beta1L));
FunXofL1=(sin(beta1*x)-sinh(beta1*x)-sigma1*(cos(beta1*x)-cosh
    (beta1*x)))/2.7242;
FunSQ1=FunXofL1^2;
LL=0:.0001:L;

%Calculate Constants for Equations
X1_bar=eval(int(FunXofL1,0,L));
X1_sq=trapz(LL,subs(FunSQ1,LL));
XL1=subs(FunXofL1,L);
dXL1=subs(diff(FunXofL1),L);
```

```
K_1=-X1_bar/X1_sq;
K_2=XL1/(p*AP*X1_sq);
K_31=dXL1/(p*Thick*Width*X1_sq);
K_32=6*d31*EI*K_31/(Thick^2);
K_3=K_dc*wn^2;

%PV=[L Thick Width Kp d31 p Mt Ml Mb g beta1L beta1 E EI
   sigma1 FunXofL1 FunSQ1 X1_bar X1_sq XL1 dXL1 K_1 K_2 K_3];

% L=PiezoValues(1);
% Thick=PiezoValues(2);
% Width=PiezoValues(3);
% Kp=PiezoValues(4);
% d31=PiezoValues(5);
% p=PiezoValues(6);
% Mt=PiezoValues(7);
% Ml=PiezoValues(8);
% Mb=PiezoValues(9);
% g=PiezoValues(10);
% beta1L=PiezoValues(11);
% beta1=PiezoValues(12);
% E= PiezoValues(13);
% EI=PiezoValues(14);
% sigma1=PiezoValues(15);
% FunXofL1=PiezoValues(16);
% FunSQ1=PiezoValues(17);
% X1_bar=PiezoValues(18);
% X1_sq= PiezoValues(19);
% XL1= PiezoValues(20);
```

```
% dXL1=PiezoValues(21);
% K_1=PiezoValues(22);
% K_2=PiezoValues(23);
% K_3=PiezoValues(24);
```

A.2.2 Piezo Modeling

```
%function GOL=Actuator_Model_All()
clear all
close all
clc
%global Ks
% GOL
%Step 1 --- fit the open loop model
%load the experimental freq response data
%load L2_1V
load NP11K


Ks=200000; % Sensor Gain
Ka=.875*3.98; % Amplifier/Saturation/Filter * Bias/Amplifier/
   Filter Gain


% first row of piezo  is frequency in Hz
% second column of piezo is G(jw) a complex number
f1_hz    = np11k(:,1); % frequency in Hz --- this is 0 to 1KHz
f1_rad   = 2*pi*f1_hz;  % frequency in radians
G1       = np11k(:,2)/Ks/Ka;  % these are complex numbers

% extract the magnitude and phase information
```

```
m1=(abs(G1)); % the magnitude of G
m1_db=20*log10(abs(G1));  % magnitude in db
p1=unwrap(angle(G1))*180/pi;



figure()
subplot(211), semilogx(f1_hz,m1_db)
subplot(212), semilogx(f1_hz,p1)
legend('1V_{pp}')
% return

% Begin model checking

% first row of piezo  is frequency in Hz
% second column of piezo is G(jw) a complex number
f_Hz    = f1_hz; % frequency in Hz --- this is 0 to 20KHz
f_rad   = f1_rad;  % frequency in radians
G       = G1;  % these are complex numbers
%return

% extract the magnitude and phase information
m=m1; % the magnitude of G
m_db=m1_db;  % magnitude in db
p=p1;
%return


%
   %%%%%%%%%%%%%%%%%%%%%%%%%%%%%%%%%%%%%%%%%%%%%%%%%%%%%%%%%%%%%%%%%%%
```

```
a1= (-0.15e02)*2*pi;  % real part of pole 1
b1= (1.25e02)*2*pi;  % imaginary part of pole 1
c1= (-0.22e02)*2*pi; % real part of zero 1
d1= (1.15e02)*2*pi;  %imaginary part of zero 1

a=a1; b=b1; c=c1; d =d1;
p1=a+b*i ; % pole 1
p2=conj(p1) ; % pole 2
z1=c+d*i ; % zero 1
z2=conj(z1); % zero 2
TF_1=(3e5)*tf([1 -z1],[1 -p1])*(tf([1 -z2],[1 -p2]));
%TF_1=  (7.0926e+006)*tf([1],[1 -p1])*(tf([1],[1 -p2])); % DC
   gain adjusted

a3= (-.0140e02)*2*pi;  % real part of pole 3
b3= (2.65e02)*2*pi;  % imaginary part of pole 3
c3= (0.3e02)*2*pi; % real part of zero 3
d3= (2.36e02)*2*pi;  %imaginary part of zero 3
%
a=a3; b=b3; c=c3; d =d3;
p1=a+b*i; % pole 1
p2=conj(p1); % pole 2
z1=c+d*i ; % zero 1
z2=conj(z1); % zero 2
TF_2=tf([1 -z1],[1 -p1])*(tf([1 -z1],[1 -p2]));
%TF_2=tf([1 ],[1 -p1])*(tf([1],[1 -p2]));

%-0.2288 + 4.3202i
```

```
%-0.1957 + 4.2854i

%-0.2037 + 4.2745i

a5= (-0.2e02)*2*pi;  % real part of pole 5 ,NEED to tune the
   damping here(a5)
b5= (3.11e02)*2*pi;  % imaginary part of pole 5
c5= (20e02)*2*pi*2*pi; % real part of zero 5
d5= (2.85e02)*2*pi;  %imaginary part of zero 5

a=a5; b=b5;
%c=c5; d =d5;
p1=a+b*i ; % pole 1
p2=conj(p1); % pole 2
z1=c+d*i ; % zero 1
z2=conj(z1);% zero 2
%TF_3=tf([1 -z1],[1 -p1])*(tf([1 -z2],[1 -p2])); % TF for the
   third peak and the third valley
TF_3=tf([1],[1 -p1])*(tf([1],[1 -p2])); %




a7=-(0.1693e02)*2*pi;  % real part of pole 5 ,NEED to tune the
    damping here(a5)
b7= (8.8382e02)*2*pi;  % imaginary part of pole 5
c7=-(0.1354e02)*2*pi; % real part of zero 5
d7= (8.7325e02)*2*pi;  %imaginary part of zero 5
```

```
a=a7; b=b7; c=c7; d =d7;
p1=a+b*i ;  % pole 1
p2=conj(p1); % pole 2
z1=c+d*i ; % zero 1
z2=conj(z1); % zero 2
TF_4=tf([1 -z1],[1 -p1])*(tf([1 -z2],[1 -p2])); % TF for the
   third peak and the third valley


syst_current=1; CASE=1;
% syst_current=TF_1;   CASE=0;
% syst_current=TF_1*TF_2;   CASE=0;
% syst_current=TF_1*TF_2*TF_3;   CASE=0;
%syst_current=TF_1*TF_2*TF_3*TF_4;   CASE=0;




%%%%%%%%%&&&&&&&&&&&&&&&&&&&&&&&&&&&&&&&&&&&&&&&&&


%[b,a]=invfreqs(G,f_rad,Nzeros,Npoles,Wt);
disp('syst_current')
GOL = syst_current % this is the model we obtain

if CASE~=1
% d=[1]
```

```
% n=[1]
%return
% lets compare the frequency responses (i.e., bode plots)
% the following generates the frequency response and store
   them
%H_sys1 = freqresp(GOL,f_rad); % obtain freq response
H_sys1 = freqresp(GOL,f_rad); % obtain freq response
Res_sys1=zeros(1,length(H_sys1(1,1,:))); Res_sys1(:)= H_sys1
   (1,1,:);

% lets compare the frequency responses (i.e., bode plots)
% the following generates the frequency response and store
   them
H_sys_current = freqresp(syst_current,f_rad); % obtain freq
   response
Res_syst_current=zeros(1,length(H_sys_current(1,1,:)));
Res_syst_current(:)= H_sys_current(1,1,:);
%return
% magnitude and phase in degrees
m_syst_current=20*log10(abs(Res_syst_current));
p_syst_current=unwrap(angle(Res_syst_current))*180/pi;


%%%%%%%%%%%%%%%%%%%%%%%%%%%%%%%%%%%%%%%%

%G=Gexperiment
sys_extra=G./Res_syst_current(:);

else
```

```
sys_extra=G;
end



Wtfreq   =[1    100   150    200 220 230 240 250   260   270 280 290
      300 325 350 400 450 500 750 1000];
Wtval    =[500    500    1      1    2   20   500   20      1     1    1
      1     1    1    1    1    1    1    1    1];

% Wtfreq   =[0    160   161    200 250   260   270 280 290   300 310
   312   315   340 400 450 460 470 500 510 700 750 1000];
% Wtval    =[1     1     1      1    1     1     1   1   1       1     1
     1    1     1     1    2     2    2    1    1    0    0    0];

% Wtfreq   =[0    160   161    200 220   245   250 255 290   295 299
   300 310 312   335   340 400 450 550 551 850 855 2000];
% Wtval    =[1     1     1      1    1    1    1    1   1    1    1     1
      1    1     1      1   1    1    0    0    0    0    0];

% Wtfreq   =[0   390 396 463 465 2000];
% Wtval    =[0   0     1   1     0   0];
Wt_extra=interp1(Wtfreq, Wtval, f_Hz);

%Wt_extra = ones(size(f_Hz));

figure();
plot(f_Hz,Wt_extra);

%return
```

```
Nzeros_extra=0;
Npoles_extra=2;

[b,a]=invfreqs(sys_extra,f_rad,Nzeros_extra,Npoles_extra,
   Wt_extra);
sys_extra_tf = tf(b,a) % this is the extra model we obtain
num =b; den =a;
save datamodel syst_current
%return

poles_new_Hz=pole(sys_extra_tf)/2/pi
zeros_new_Hz=tzero(sys_extra_tf)/2/pi



%return

sys_total= syst_current*sys_extra_tf

%
   %%%%%%%%%%%%%%%%%%%%%%%%%%%%%%%%%%%%%%%%%%%%%%%%%%%%%%%%%%%%%%%%%%%

%
   %%%%%%%%%%%%%%%%%%%%%%%%%%%%%%%%%%%%%%%%%%%%%%%%%%%%%%%%%%%%%%%%%%%


%return
poletotal_radpsec=pole(sys_total)
```

```
zerototal_radpsec=tzero(sys_total)

poletotal_Hz=pole(sys_total)/2/pi
zerototal_Hz=tzero(sys_total)/2/pi

%return




%[b,a]=invfreqs(G,f_rad,Nzeros,Npoles,Wt);
GOL = sys_total % this is the model we obtain

% lets compare the frequency responses (i.e., bode plots)
% the following generates the frequency response and store
   them
H_sys1 = freqresp(GOL,f_rad); % obtain freq response
Res_sys1=zeros(1,length(H_sys1(1,1,:))); Res_sys1(:)= H_sys1
   (1,1,:);
% magnitude and phase in degrees
m_GOL=20*log10(abs(Res_sys1));
p_GOL=unwrap(angle(Res_sys1))*180/pi;



%m_syst_current=20*log10(abs(Res_syst_current));
%p_syst_current=unwrap(angle(Res_syst_current))*180/pi;
%return
% compare the frequency responses

if CASE~=1
```

```
%figure_no = figure_no +1;
figure()
subplot(2,1,1);
semilogx(f_Hz, m_db,'b-', f_Hz, m_GOL,'k:',f_Hz,m_syst_current
    ,'r');
title('OPEN␣LOOP␣Freq␣response');
xlabel('Frequency␣(Hz)');
ylabel('Magnitude␣(db)');
subplot(2,1,2);
semilogx(f_Hz, p,'b-', f_Hz, p_GOL,'k:',f_Hz,p_syst_current,'r
   ' );
xlabel('Frequency␣(Hz)');
ylabel('Phase␣(degree)');
legend('experimental','model','sys_{current}',3);

else
%figure_no = figure_no +1;
figure()
subplot(2,1,1);
semilogx(f_Hz, m_db,'b-', f_Hz, m_GOL,'k:');
title('OPEN␣LOOP␣Freq␣response');
xlabel('Frequency␣(Hz)');
ylabel('Magnitude␣(db)');
subplot(2,1,2);
semilogx(f_Hz, p,'b-', f_Hz, p_GOL,'k:');
xlabel('Frequency␣(Hz)');
ylabel('Phase␣(degree)');
legend('experimental','model','sys_{current}',3);
end
```

```
%%%%%%%%%%%%%%%%%%%%%%%
return
K=2.32e-06;
wn=239.6696*2*pi;
zeta=.045;
sys_model=tf([K*wn^2],[1 2*zeta*wn wn^2]);
H_sys2 = freqresp(sys_model,f_rad); % obtain freq response
Res_sys2=zeros(1,length(H_sys2(1,1,:))); Res_sys2(:)= H_sys2
   (1,1,:);
% magnitude and phase in degrees
m_sys=20*log10(abs(Res_sys2));
p_sys=unwrap(angle(Res_sys2))*180/pi;

figure()
subplot(2,1,1);
semilogx(f_Hz, m_db,'b-', f_Hz, m_sys,'k:');
title('OPEN␣LOOP␣Freq␣response');
xlabel('Frequency␣(Hz)');
ylabel('Magnitude␣(db)');
subplot(2,1,2);
semilogx(f_Hz, p,'b-', f_Hz, p_sys,'k:');
xlabel('Frequency␣(Hz)');
ylabel('Phase␣(degree)');
legend('experimental','model','sys_{current}',3);

figure()
subplot(2,1,1);
semilogx(f_Hz, m_db-m_sys');
title('OPEN␣LOOP␣Freq␣response');
```

```
xlabel(’Frequency␣(Hz)’);
ylabel(’Magnitude␣(db)’);
subplot(2,1,2);
semilogx(f_Hz, p-p_sys’);
xlabel(’Frequency␣(Hz)’);
ylabel(’Phase␣(degree)’);

figure()
subplot(2,2,1);
semilogx(f_Hz, m_db,’b-’, f_Hz, m_sys,’k:’);
title(’Frequency␣Response␣of␣Actuator␣and␣Model’);
xlabel(’Frequency␣(Hz)’);
ylabel(’Magnitude␣(db)’);
subplot(2,2,3);
semilogx(f_Hz, p,’b-’, f_Hz, p_sys,’k:’);
xlabel(’Frequency␣(Hz)’);
ylabel(’Phase␣(degree)’);
legend(’experimental’,’model’);
subplot(2,2,2);
semilogx(f_Hz, m_db-m_sys’);
title(’Modeling␣Errors’);
xlabel(’Frequency␣(Hz)’);
ylabel(’Magnitude␣(db)’);
subplot(2,2,4);
semilogx(f_Hz, p-p_sys’);
xlabel(’Frequency␣(Hz)’);
ylabel(’Phase␣(degree)’);
```

A.2.3 Positive and Negative Time Checking

```
% FUNCTION SIGN CHECKER
```

```
function ptime=postime(t,v)
p=zeros(size(v));

j=max(size(v));

for k=1:j
    if (v(k) > 0)
        p(k)=1;
    else
        p(k)=0;
    end
end
ptime=trapz(t,p);

return
% FUNCTION SIGN CHECKER

function ptime=negtime(t,v)
p=zeros(size(v));

j=max(size(v));

for k=1:j
    if (v(k) < 0)
        p(k)=1;
    else
        p(k)=0;
    end
```

```
end
ptime=trapz(t,p);

return
```

A.2.4 Main Simulation

```
% piezo
% V15 uses the simulated friction as opposed to the theory
   friction to get
% the system voltage
clear all
close all
clc

% tstart=tic;

% global L I Thick Width AP Kp d31 p Mt Ml Mb g beta1L beta1 E
    EI sigma1 wn zeta
% global FunXofL1 FunSQ1 X1_bar X1_sq XL1 dXL1 K_1 K_2 K_3
   K_31 K_32 dt mu_k mu_s

global p Mt g wn zeta XL1 K_1 K_2 K_32 dt mu_k mu_s
global time_low yyd yydd V_sys yy F_total switchvar
switchvar=1;
% friction force parameters
% mu_k = 0.4; % kinetic friction coefficient
mu_k=0.2;
mu_s = 0.3; % static friction coefficient
% mu_s=mu_k;
g  = 9.81; % gravity constant
```

```
% return

% piezo parameters
wn=239*2*pi; % Natural Frequency
zeta = 0.045;     % damping ratio
Kdc =2.32e-06;          % dc gain of system
y_disp_max = 1*Kdc; % micro-meters of motion

% Piezo(Kdc,wn)
load variables_all
Mt=0.01;

% return
% original system
G = ss([0 1; -wn*wn -2*wn*zeta],[0; Kdc*wn*wn],[1 0],[0]);
G_pert_wn = ss([0 1; -(1.05*wn)*(1.05*wn) -2*(1.05*wn)*zeta
   ],[0; Kdc*(1.05*wn)*(1.05*wn)],[0 1],[0]);
G_pert_zeta = ss([0 1; -wn*wn -2*wn*(1.05*zeta)],[0; Kdc*wn*wn
   ],[ 0 1 ],[0]);



% G_pert_wn = ss([0 1; -(1.05*wn)*(1.05*wn) -2*(1.05*wn)*zeta
   ],[0; Kdc*(1.05*wn)*(1.05*wn)],[1 0],[0]);
% G_pert_zeta = ss([0 1; -wn*wn -2*wn*(1.05*zeta)],[0; Kdc*wn*
   wn],[ 1 0 ],[0]);



%filter system
wf = 8000*2*pi; sys_f = ss([-wf],[wf],[1],[0]);
```

```
dt=1/10000000; % Delta T
dt2=1/1000000; % Delta T

Freq=100; % Frequency
T=1/Freq; % Period
% return
% V_in=47; % Minimum Value for mu=0.41 THEORY
% V_in=46; % Minimum Value for mu=0.41 SIMULATION
%  These values are for 100 Hz operating frequency
% V_in=21.5600; % 50  um
% V_in=32.3400; % 75  um
% V_in=43.1200; % 100 um
% V_in=53.8991; % 125 um
% V_in=64.6789; % 150 um
% V_in=75.4587; % 175 um
% V_in=86.2385; % 200 um
% V_in=97.0183; % 225 um
% V_in=107.7982; % 250 um
% V_in=118.5780; % 275 um
% V_in=129.3500; % 300 um
% V_in=140.1376; % 325 um
% V_in=150.9174; % 350 um
% V_in=(1/2.3192)*disp; % Any arbitrary displacement
disp=30e-6;
% V_in=(disp)*sqrt((wn^2-(Freq*2*pi)^2)^2-(4*zeta^2*wn^2*(Freq
   *2*pi)^2))/(Kdc*wn^2);
% Asymmetry (FIXED)
Skew=35;
```

```
% New trajectory, no linear/1st order constraints
y=TrajFun_5th(Freq, Skew, Kdc, dt) ;

% This is where I can scale the trajectories
Delta_P=max(y(1,:))-min(y(1,:)); % Maximum change in position

% V input set above
p=(y(1,:)/(Delta_P))*disp;
p=p+((max(p)-min(p))/2);
v=(y(2,:)/(Delta_P))*disp;
a=(y(3,:)/(Delta_P))*disp;
t=y(4,:)-min(y(4,:));
disp_max=max(p)-min(p);
%
% Uncomment this block if you want to plot the sticking region
% figure()
% subplot(211), plot(t,-v)
% subplot(212), plot(t,a,t,ones(size(a))*mu_s*g,'r--',t,ones(
   size(a))*-mu_s*g,'r--')
% return

% Uncomment this block if you want to plot the trajectories
% figure()
% subplot(311), plot(t,p)
% ylabel('Position')
% subplot(312), plot(t,v)
% ylabel('Velocity')
```

```
% subplot(313), plot(t,a)
% ylabel('Acceleration')
% xlabel('Time (sec)')
% return

% Pattern the trajectories, end up with repeatvalue+1
tsize=length(t);
repeatvalue=9;
yy=[p repmat(p(2:tsize),1,repeatvalue)];
yyd=[v repmat(v(2:tsize),1,repeatvalue)];
yydd=[a repmat(a(2:tsize),1,repeatvalue)];
time=linspace(0,(repeatvalue+1)*1/Freq,max(size(yy)));


% NFFT = 2^nextpow2(length(time)); % Next power of 2 from
   length of y
% Y = fft(yyd,NFFT)/length(time);
% f = (1/dt)/2*linspace(0,1,NFFT/2+1);
%
% % Plot single-sided amplitude spectrum.
% plot(f,2*abs(Y(1:NFFT/2+1)))
% title('Single-Sided Amplitude Spectrum of y(t)')
% xlabel('Frequency (Hz)')
% ylabel('|Y(f)|')

u_dot=zeros(size(time));
% u_dot(1)=0.031006;
% u_dot(1)=0.029;
u_dot(1)=0.0;
```

```
% u_dot(1)=0.0176606;
F_total=zeros(size(time));
F_total(1)=0;

for ii=2:length(time)
    u_dot(ii)=u_dot(ii-1)-dt*fstep(u_dot(ii-1),yyd(ii-1),yydd(
       ii-1),mu_k,mu_s,dt);
    F_total(ii)=-Mt*fstep(u_dot(ii-1),yyd(ii-1),yydd(ii-1),
       mu_k,mu_s,dt);
end
F_total(1)=F_total(2);
F_repeat=F_total(end-T/dt:end);
F_total=[F_repeat repmat(F_repeat(2:tsize),1,repeatvalue)];
% FF=[F_total repmat(F_total(2:tsize),1,repeatvalue)];
%
V_Piezo=(1/(XL1*K_32))*(yydd+2*zeta*wn*yyd+(wn^2)*yy);
V_Friction=(-1/K_32)*(((K_1/Mt)+K_2/3)*F_total);
V_Friction(1)=V_Friction(end);
% V_DC=yy/Kdc;
% % Total System voltage
V_sys=V_Piezo+V_Friction;
%
%


figure()
plot(time,u_dot,time,-yyd)
xlabel('Time')
ylabel('Velocity')
```

```
figure()
plot(time,u_dot)
xlabel('Time')
ylabel('Velocity')

figure()
plot(time,cumtrapz(time,u_dot))


% return
% Y_p=lsim(G_pert,V_Piezo,time);
% figure()
% plot(time(end-T/dt:end),-u_dot(end-T/dt:end),time(end-T/dt:
   end),Y_p(end-T/dt:end))
% return
% % RESAMPLE THE VECTORS TO FREE UP SOME MEMORY...
time_low=0:dt2:time(end);
yy=qinterp1(time,yy,time_low,0);
yyd=qinterp1(time,yyd,time_low,0);
yydd=qinterp1(time,yydd,time_low,0);
V_sys=qinterp1(time,V_sys,time_low,0);
V_Piezo=qinterp1(time,V_Piezo,time_low,0);
V_Friction=qinterp1(time,V_Friction,time_low,0);
F_total=qinterp1(time,F_total,time_low,0);
u_dot=qinterp1(time,u_dot,time_low,0);
```

```
% figure()
% plot(time,V_Piezo,time,V_sys,'r--',time,V_DC,'k:')
% xlabel('Time')
% ylabel('Voltage')
% legend('$V_{Piezo}$','$V_{Friction}$','$V_{DC}$')
% return
%

options=odeset('RelTol',1e-5,'AbsTol',1e-10);
yydd=yydd';
yyd=yyd';
yy=yy';
F_total=F_total';
V_sys=V_sys';

param=[time_low;yyd;yydd;V_sys;yy;F_total];
% 0.031513
% yy(1);yyd(1);0.0314007
% [-9.612439328255877e
   -005;-0.007528626214358;0.025040949874989]
tic
[TT,YY]=ode23s(@stepper,time_low,[yy(1);yyd(1);0;0],options,
   param);
toc
yb_sim=YY(:,4)';
yb_pos_sim=YY(:,3)';
yp_sim=YY(:,2)';

figure()
```

```
plot(TT,yb_sim,TT,-yp_sim)
legend(’ybsim’,’-ypsim’,’-v’,’udot’)

figure()
plot(TT,yb_sim,time_low,u_dot)
title(’body␣velocities’)
%
% figure()
% plot(time_low,yb_pos_sim,’b--’,0.19926,yb_pos_sim(floor
   (10*0.19926*5000/0.05)),’rs’,0.4246,yb_pos_sim(floor
   (10*0.4246*5000/0.05)),’r+’,0.61392,yb_pos_sim(floor
   (10*0.61392*5000/0.05)),’rs’)%,1.219,yb_pos_sim(floor
   (10*1.219*T/dt)),’r+’)
% % title(’’)
% xlabel(’Time (s)’)
% ylabel(’Position (m)’)
% legend(’$y_b$’,’$t_{trans,i}$’,’$t_{trans,f}$’)
% axis([0.00 time_low(end)  -12e-3 12e-3])

% figure()
% plot(time_low,yb_pos_sim,’b--’,0.3767,yb_pos_sim(floor
   (10*0.3767*T/dt)),’rs’,0.4688,yb_pos_sim(floor(10*0.4688*T/
   dt)),’r+’,1.1254,yb_pos_sim(floor(10*1.1254*T/dt)),’rs
   ’,1.219,yb_pos_sim(floor(10*1.219*T/dt)),’r+’)
% % title(’’)
% xlabel(’Time (s)’)
% ylabel(’Body Position, $\dot{y}_b$ (m)’)
% legend(’$y_b$’,’$t_{trans,i}$’,’$t_{trans,f}$’)
% axis([0.00 time_low(end)  -1e-3 13e-3])
```

```
% ,[0.07 0.07],[-1e-3 yb_pos_sim(70000)],'g:'
% ,[0.928 0.928],[13e-3 yb_pos_sim(44780)],'g:'
return
figure(44)
plot(time_low,yb_pos_sim,time_low,ones(size(time_low))*0.0009,
   'r--',time_low,ones(size(time_low))*0.0023,'r--',time_low
   ,(0.025791193141064.*time_low-0.000631101008483),'g')
xlabel('Time␣(s)')
ylabel('Body␣Position␣(m)')
axis([0.07 0.12  0.5e-3 3.5e-3])

figure(55)
plot(time_low,yb_pos_sim-(-0.025850636373286.*time_low
   +0.019988497953702))
xlabel('Time␣(s)')
ylabel('Error␣(m)')
% axis([0.4688 1.12 -2e-5 2e-5])
axis([0.80 0.82 -1.5e-5 1.5e-5])

figure(56)
plot(time_low,yb_pos_sim-(-0.058571177350000.*time_low
   +0.026398180204528))
xlabel('Time␣(s)')
ylabel('Error␣(m)')
axis([0.4596 0.6065 -0.5e-5 0.5e-5])

return
figure()
plot(TT,yp_sim,time_low,yyd)
```

```
title('piezo␣velocities')

% yp_sim_interp=interp1(TT,yp_sim,time);
% yb_sim_interp=interp1(TT,yb_sim,time);
% yb_pos_sim_interp=interp1(TT,yb_pos_sim,time);
clear yy yydd

% return
%
% error_body=u_dot-yb_sim_interp;
%
% figure()
% plot(time,error_body)
% title('body error')
%
% yp_sim_interp=interp1(TT,yp_sim,time);
% error_piezo=yyd-yp_sim_interp;
%
% figure()
% plot(time,error_piezo)
% title('piezo error')

% save yb_sim_interp
% save param

% load yb_sim_interp
% load param

% return
```

```
% 0.0314007
% wn_p,zeta_p,muk_p,mus_p,mass_p
tic
[TT_p,YY_p]=ode23s(@stepper_perturbation,[0 time(end)
   ],[0;0;0],[],param,1,1,1,1,1);
toc
yb_sim_p=YY_p(:,3)';
yp_sim_p=YY_p(:,2)';

yb_sim_interp_p=interp1(TT_p,yb_sim_p,time);
yp_sim_interp_p=interp1(TT_p,yp_sim_p,time);

figure()
plot(time,yb_sim_interp,time,yb_sim_interp_p)
xlabel('Time')
ylabel('Velocity')
legend('Steady-state','Zero␣I.C.␣for␣Piezo')

figure()
plot(time,yp_sim_interp,time,yp_sim_interp_p)
xlabel('Time')
ylabel('Velocity')
legend('Steady-state','Zero␣I.C.␣for␣Piezo')



figure()
plot(time,yb_sim_interp-yb_sim_interp_p)
title('error')
```

```
SS_Vel=trapz(time_low((end-(T/dt)):end),yb_sim((end-T/dt):end)
   )/T;
SS_Vel_p=trapz(time((end-(T/dt)):end),yb_sim_interp_p((end-T/
   dt):end))/T;

error=SS_Vel_p-SS_Vel;
percenterror=100*error/SS_Vel

% m_error_p99=yb_sim_interp_p;
wn_error_p95=yb_sim_interp_p;
% textme



beep
beep
beep
beep
% fprintf_r('\r %0.5f',t)
% v1=interp1(time,v,t,'nearest');
% a1=interp1(time,a,t,'nearest');
% p1=interp1(time,p,t,'nearest');
% F1=interp1(time,FF,t,'nearest');
```

A.2.5 ODE Function

```
function Y=stepper(t,X,param)

% global Mt K_1 K_2 K_32 wn mu_k  zeta
global V_sys time_low yyd yydd yy switchvar
Mt=0.0276;
```

```
K_1=-1.565953009261387;
K_2=2.841203196673054e+03;
K_32=5.219593077017946;
wn=1.501681288415921e+03;
mu_k=0.2;
mu_s=0.4;
zeta=0.045;
g=9.81;
% time=param(1,:);
% v=param(2,:);
% a=param(3,:);
% p=param(5,:);
% FF=param(6,:);
% Vin=param(4,:);
V=qinterp1(time_low,V_sys,t,0);
% v1=qinterp1(time_low,yyd,t,0);
% a1=qinterp1(time_low,yydd,t,0);
% p1=qinterp1(time_low,yy,t,0);
% F1=qinterp1(time,FF,t,0);
% fprintf_r('\r %0.5f',t)
Y=[0;0;0;0];
fprintf_r('\r␣%0.5f',t)
% Perfect System
% Y(1)=v1;
% Y(2)=a1;
% Y(3)=F1/Mt;

% Compute F
% Y(1)=v1;
```

```
% Y(2)=a1;
% Fs=-mu_k*Mt*g*sign(X(4)+v1);
% Y(3)=X(4);
% Y(4)=Fs/Mt;

% % Calculate Y(2) with other perfect information
% Y(1)=v1;
% Fs=-mu_k*Mt*g*sign(X(4)+v1);
% Y(2)=-wn^2*p1-2*zeta*wn*v1+K_32*V+(K_1/Mt+K_2/3)*Fs;
% Y(3)=X(4);
% Y(4)=Fs/Mt;
%
%
% Calculate Y(2) with other perfect information
% if (X(3)>0.009)
% figure(99)
% plot(t,X(3))
% hold on
% switchvar
% end

% if (X(3))>0.010  && switchvar == 1
%      V=-V;
%      p1=-p1;
%      v1=-v1;
%      switchvar=2;
%      t
% end
%
```

```
% if switchvar==2
%       V=-V;
%       p1=-p1;
%       v1=-v1;
% end
%
% if (X(3))<-0.010 && switchvar == 2
% %       V=V;
% %       p1=p1;
% %       v1=v1;
%       switchvar=1;
%       t
% end
% if switchvar==1
%       V=V;
%       p1=p1;
%       v1=v1;
% end

% Y(1)=v1;
% Fs=-mu_k*Mt*g*sign(X(4)+v1);
% Y(2)=-wn^2*p1-2*zeta*wn*v1+K_32*V+(K_1/Mt+K_2/3)*Fs;
% Y(3)=X(4);
% Y(4)=Fs/Mt;



% % Calculate Y(2) with friction known but others not
% Y(1)=X(2);
% Y(2)=-wn^2*X(1)-2*zeta*wn*X(2)+K_32*V+(K_1/Mt+K_2/3)*F1;
```

```
% Y(3)=F1/Mt;

%       if (X(3))>0.003
%            V=0;
%       end

% Calculate Y(2), F, states, kinetic only
% Y(1)=X(2);
% Fs=-mu_k*Mt*g*sign(X(4)+X(2));
% Y(2)=-wn^2*X(1)-2*zeta*wn*X(2)+K_32*V+(K_1/Mt+K_2/3)*Fs;
% Y(3)=X(4);
% Y(4)=Fs/Mt;
%
% % Calculate Y(2), F, states, static Check kinetic first
% Y(1)=X(2);
% if abs(X(3)+X(2))>0.000001
%       Fs=-mu_k*Mt*g*sign(X(3)+X(2));
%       Y(2)=-wn^2*X(1)-2*zeta*wn*X(2)+K_32*V+(K_1/Mt+K_2/3)*Fs;
% else
% %       Fs=-mu_s*Mt*g*sign(X(3));
%       Fs=(K_1/Mt+K_2/3+1/Mt)^-1*(wn^2*X(1)+2*zeta*wn*X(2)-K_32
   *V);
%       Y(2)=-Fs/Mt;
%       disp('I got into the static check')
% end
%       Y(3)=Fs/Mt;

% % % Calculate Y(2), F, states, static Check static first
% Y(1)=X(2);
```

```
% Fs=(K_1/Mt+K_2/3+1/Mt)^-1*(wn^2*X(1)+2*zeta*wn*X(2)-K_32*V);
% if abs(Fs)<= mu_s*Mt*g
%     if abs(X(3)+X(2))<0.0000001
%         Y(2)=-Fs/Mt;
%         disp('I got into the static check')
%     else
%         Fs=-mu_k*Mt*g*sign(X(3)+X(2));
%         Y(2)=-wn^2*X(1)-2*zeta*wn*X(2)+K_32*V+(K_1/Mt+K_2/3)
   *Fs;
%     end
% else
%     Fs=-mu_k*Mt*g*sign(X(3)+X(2));
%     Y(2)=-wn^2*X(1)-2*zeta*wn*X(2)+K_32*V+(K_1/Mt+K_2/3)*Fs;
% end
% Y(3)=Fs/Mt;

% % Calculate Y(2), F, states, static Check static first
Y(1)=X(2);
    if abs(X(4)+X(2))<eps(1)
            Fs=(K_1/Mt+K_2/3+1/Mt)^-1*(wn^2*X(1)+2*zeta*wn*X
               (2)-K_32*V);
            if abs(Fs)<= mu_s*Mt*g
                Y(2)=-Fs/Mt;
                disp('I␣got␣into␣the␣static␣check')
            else
                Fs=-mu_s*Mt*g*sign(X(4)+X(2));
                Y(2)=-wn^2*X(1)-2*zeta*wn*X(2)+K_32*V+(K_1/Mt+
                   K_2/3)*Fs;
                disp('Saturated␣Static␣Friction')
```

```
            end
    else
        Fs=-mu_k*Mt*g*sign(X(4)+X(2));
        Y(2)=-wn^2*X(1)-2*zeta*wn*X(2)+K_32*V+(K_1/Mt+K_2/3)*
           Fs;
    end
Y(3)=X(4);
Y(4)=Fs/Mt;
```

A.2.6 Sensitivity Analysis

```
% Parameter Sensitivity Plots

Variation=-5:1:5;

wn_error=[-16.5 -8.5 -1.26 4.4 2.99 0 -5.05 -10.5 -15 -18
   -23];

zeta_error=[0.5 0.4 0.19 0.13 0.10 0 -0.17 -0.27 -0.36 -0.48
   -0.59  ];

muk_error=[ 0.027 0.02 0.07 0.022 -0.023 0 -0.07 -0.47 -0.6
   -0.8 -0.96 ];

m_error=[-1.99 -0.55 -0.39 -0.24 -0.26  0 0.03 -0.06 -0.23
   -0.46 -0.35 ];
figure()
plot(Variation,wn_error,'bs',Variation,zeta_error,'rx',
   Variation,muk_error,'ko')
xlabel('Variation␣in␣Parameter␣(1=nominal)')
ylabel('Percent␣Error␣in␣Response')
```

```
title('Parameter␣Sensitivity')
legend('$\omega_1$','$\zeta$','$\mu_k$')
set(gca,'XTick',Variation)

figure()
subplot(221), plot(Variation,wn_error,'bs')
ylabel('$e_{ss}~(\%)$')
xlabel('$\%$␣Variation,␣$\omega_1$')
set(gca,'XTick',[-5 0 5])
subplot(222), plot(Variation,zeta_error,'bs')
ylabel('$e_{ss}~(\%)$')
xlabel('$\%$␣Variation,␣$\zeta_1$')
set(gca,'XTick',[-5 0 5])
subplot(223), plot(Variation,muk_error,'bs')
ylabel('$e_{ss}~(\%)$')
xlabel('$\%$␣Variation,␣$\mu_k$')
set(gca,'XTick',[-5 0 5])
subplot(224), plot(Variation,m_error,'bs')
ylabel('$e_{ss}~(\%)$')
xlabel('$\%$␣Variation,␣$M_t$')
set(gca,'XTick',[-5 0 5])

figure()
plot(Variation,muk_error,'ko')
xlabel('Variation␣in␣Parameter␣(1=nominal)')
ylabel('Percent␣Error␣in␣Response')
title('Parameter␣Sensitivity␣in␣$\mu_k$')
% legend('$\omega_1$','$\zeta$','$\mu_k$')
set(gca,'XTick',Variation)
```

A.2.7 Friction Analysis

```
% Friction Coefficient Experiment 10

Frames=[0
1
2
3
4
5
6
7
8
9
10
11
12
13
14
15
16
17
18
19
20
21
22
23
24
25
```

```
26
27
28];
Time=(1/60)*Frames;

Dist_Actual=(1/1000)*[102
103
104
106
109
112
116
120
125
131
137
144
152
160
169
179
189
200
211
224
237
251
266
282
```

```
298
315
333
351
370];

Dist_Actual=Dist_Actual-Dist_Actual(1);
Time_Matrix=[.5*((Time-0/30).^2) (Time-0/30)];
Time_Matrix2=[.5*(Time.^2)];
Sol=Time_Matrix\Dist_Actual;
Sol2=Time_Matrix2\Dist_Actual;
a=Sol(1);
v_o=Sol(2);
a2=Sol2(1);
g=9.81;
%
theta_deg=35;
theta=theta_deg*pi/180;



mu=(g*sin(theta)-a)/(g*cos(theta));
mu2=(g*sin(theta)-a2)/(g*cos(theta));
S=v_o*Time+.5*a*Time.^2;
S2=.5*a*(Time).^2;

figure()
plot(Time,Dist_Actual,Time,S,'--')
xlabel('Time')
ylabel('Distance')
```

```
legend('Experimental','Fit')

figure()
plot(Time,Dist_Actual,Time,S,'--',Time,S2,'.-')
xlabel('Time')
ylabel('Distance')
legend('Experimental','Fit','Fit␣Quad␣only')
```

A.3 Matlab Code for Chapter 3

A.3.1 Stepper Simulation

```
clear all
close all
clc

% tstart=tic;

% global L I Thick Width AP Kp d31 p Mt Ml Mb g beta1L beta1 E
    EI sigma1 zeta wn
% global FunXofL1 FunSQ1 X1_bar X1_sq XL1 dXL1 K_1 K_2 K_3
   K_31 K_32 dt mu_k mu_s switchvar

% friction force parameters
mu_k = 0.2; % kinetic friction coefficient
mu_s = 0.3; % static friction coefficient

g  = 9.81e6; % gravity constant um/s^2

% Natural Frequency
% w1=188000; % rad/sec
```

```
% w1_hz=29932; % hz

w1_hz1=4147;
w1_1=w1_hz1*2*pi;

w1_hz2=6150;
w1_2=w1_hz2*2*pi;

% Damping Ratio
zeta1=0.0159;
zeta2=0.0159;
% DC Gain
% K_dc1=(0.0901)/(1e6); % m/V
% K_dc2=(0.0923)/(1e6); % m/V
K_dc=10^(-18.76/20);
% load variables_all
Mt=0.008;

dt=1/10000000; % Delta T
% dt=1/100000; % Delta T % Increased  to increase comp speed.
Freq=750; % Frequency
T=1/Freq; % Period

disp=3; % um

% Asymmetry (FIXED)
Skew=65;
Kdc=1;
```

```
% New trajectory, no linear/1st order constraints
y=TrajFun_5th(Freq, Skew, Kdc, dt);

% This is where I can scale the trajectories
Delta_P=max(y(1,:))-min(y(1,:)); % Maximum change in position

% V input set above
p=(y(1,:)/(Delta_P))*disp;
p=p+((max(p)-min(p))/2);
v=(y(2,:)/(Delta_P))*disp;
a=(y(3,:)/(Delta_P))*disp;
t=y(4,:)-min(y(4,:));
disp_max=max(p)-min(p);
% p=2*disp*sin(100*2*pi*t);
% v=2*disp*100*2*pi*cos(100*2*pi*t);
% a=-2*disp*(100*2*pi)^2*sin(100*2*pi*t);

% Uncomment this block if you want to plot the trajectories
% figure()
% subplot(311), plot(t,p)
% ylabel('Position')
% subplot(312), plot(t,v)
% ylabel('Velocity')
% subplot(313), plot(t,a)
% ylabel('Acceleration')
% xlabel('Time (sec)')
% return

% Pattern the trajectories, end up with repeatvalue+1
```

```
tsize=length(t);
repeatvalue=19;
yy=[p repmat(p(2:tsize),1,repeatvalue)]-min(p);
yyd=[v repmat(v(2:tsize),1,repeatvalue)];
yydd=[a repmat(a(2:tsize),1,repeatvalue)];
time=linspace(0,(repeatvalue+1)*1/Freq,max(size(yy)));

% Generate the shifted trajectories
yy1=circshift(yy,round(T/dt/2)*ones(size(yy)));
yyd1=circshift(yyd,round(T/dt/2)*ones(size(yyd)));
yydd1=circshift(yydd,round(T/dt/2)*ones(size(yydd)));

figure()
plot(time,yy,time,yy1,’g--’)
xlabel(’Time␣(s)’)
ylabel(’Position␣(m)’)
% axis([0 time(end) -0.04 0.14])
legend(’$y_1(t)$’,’$y_2(t)$’)

figure()
plot(time,yyd,time,yyd1,’g--’)
xlabel(’Time␣(s)’)
ylabel(’Velocity␣(m/s)’)
% axis([0 time(end) -0.04 0.14])
legend(’$\dot{y}_1(t)$’,’$\dot{y}_2(t)$’)


% return
```

```
u_dot=zeros(size(time));
N=Mt*g/(4*sin(0.908));
slope1=2*mu_k*N*dt;
slope2=2*mu_k*N*dt;
u_dot(1)=0;

for ii=2:length(time)
    u_dot(ii)=u_dot(ii-1)-(slope1/Mt)*sign(u_dot(ii-1)-yyd(ii
       -1))-(slope2/Mt)*sign(u_dot(ii-1)-yyd(ii-1))-0*dt*g*sin(
       pi*2/180);
end
figure()
plot(time,yyd,time,yyd1,time,u_dot)
xlabel(’Time’)
ylabel(’Velocity’)

u=cumtrapz(time,u_dot);

figure()
plot(time,u)
xlabel(’Time␣(s)’)
ylabel(’Stage␣Position␣(um)’)


return

F_1=-mu_k*2*N*sign(u_dot-yyd); % Friction Force - 1
F_2=-mu_k*2*N*sign(u_dot-yyd1); % Friction Force - 2
```

```
V_Piezo=yy/K_dc;
V_Piezo1=yy/K_dc;

% V_Piezo=(1/(K_dc1*(w1_1^2)))*(yydd+2*zeta1*w1_1*yyd+(w1_1^2)
   *(yy));
% V_Piezo1=(1/(K_dc2*(w1_2^2)))*(yydd1+2*zeta2*w1_1*yyd1+(w1_2
   ^2)*(yy1));

% V_F=-(1/(K_dc1*(w1_1^2)))*F_1*0;
% V_F_1=-(1/(K_dc2*(w1_2^2)))*F_2*0;

% V_in=V_Piezo+V_F;
% V_in_1=V_Piezo1+V_F_1;

V_in=V_Piezo;
V_in_1=V_Piezo1;



figure()
plot(time,V_Piezo,time,V_in)

V_in=1*sin(2*pi*Freq*time);
V_in1=V_in;
% return
V_double=V_in((end-2/dt/Freq):end);
index_of_zero=find(V_double(1:end-1).*V_double(2:end)<=0);
index_of_zero=index_of_zero(end-2);
U_FF=V_double(index_of_zero:index_of_zero+1/Freq/dt);
U_FF_Actuator=U_FF-(U_FF(end));
```

```
V_double1=V_in_1((end-2/dt/Freq):end);
% index_of_zero=find(V_double1(1:end-1).*V_double1(2:end)<=0);
% index_of_zero=index_of_zero(end-2);
% U_FF1=V_double1(index_of_zero:index_of_zero+1/Freq/dt);
% U_FF_Actuator1=U_FF1-(U_FF1(end));
U_FF_Actuator1=V_double1(index_of_zero:index_of_zero+1/Freq/dt
   );


% time_200K=0:1/200000:1/Freq;
time_200K=0:1/200000:1/Freq;
Voltage_new=interp1(0:dt:1/Freq,U_FF_Actuator,time_200K','
   nearest');
Voltage_new1=interp1(0:dt:1/Freq,U_FF_Actuator1,time_200K','
   nearest');

figure()
plot(time_200K,Voltage_new,time_200K,Voltage_new1)
xlabel('Time␣(s)')
ylabel('Voltage␣(V)')
legend('$V_1(t)$','$V_2(t)$')
% return
VT=(Voltage_new)/20; % Accounts for Amplifier Pre-Piezo
VT1=(Voltage_new1)/20; % Accounts for Amplifier Pre-Piezo

if  mean(VT>120) > 0
    disp('STOP')
```

```
    return
end
if  mean(VT<-20) > 0
    disp('STOP')
    return
end

% return
figure()
plot(time_200K,VT,time_200K,VT1)
xlabel('Time␣(sec)')
ylabel('Scaled␣Voltage␣(V)')
title('␣Output␣Voltage␣to␣be␣Amplified')
% return
VT=VT(1:end-1);
VT1=VT1(1:end-1);
return
outputname='Sine_Wave_750Hz';
VT_Store=VT;
% VT=VT(1:end-1);
format short
% DataName=sprintf('INV_100_%dV_25.txt',V);
DataName=sprintf('%s.txt',outputname);
fid = fopen(char(DataName),'w');
fprintf(fid, '%2.4f\t', VT);
fclose('all');

outputname1='SINGLE_A2_1um_1khz';
VT_Store1=VT1;
```

```
% VT1=VT1(1:end-1);
format short
% DataName=sprintf('INV_100_%dV_25.txt',V);
DataName=sprintf('%s.txt',outputname1);
fid = fopen(char(DataName),'w');
fprintf(fid, '%2.4f\t', VT1);
fclose('all');

%
    %%%%%%%%%%%%%%%%%%%%%%%%%%%%%%%%%%%%%%%%%%%%%%%%%%%%%%%%%%%%%%%%%%%%%%%%%

%
    %%%%%%%%%%%%%%%%%%%%%%%%%%%%%%%%%%%%%%%%%%%%%%%%%%%%%%%%%%%%%%%%%%%%%%%%%

%
    %%%%%%%%%%%%%%%%%%%%%%%%%%%%%%%%%%%%%%%%%%%%%%%%%%%%%%%%%%%%%%%%%%%%%%%%%

%
    %%%%%%%%%%%%%%%%%%%%%%%%%%%%%%%%%%%%%%%%%%%%%%%%%%%%%%%%%%%%%%%%%%%%%%%%%

%
    %%%%%%%%%%%%%%%%%%%%%%%%%%%%%%%%%%%%%%%%%%%%%%%%%%%%%%%%%%%%%%%%%%%%%%%%%

%
    %%%%%%%%%%%%%%%%%%%%%%%%%%%%%%%%%%%%%%%%%%%%%%%%%%%%%%%%%%%%%%%%%%%%%%%%%
```

```
% return
% p=param(2,:);
% p2=param(3,:);
% v=param(4,:);
```

```
% v2=param(5,:);
% a=param(6,:);
% a2=param(7,:);
switchvar=1;
param=[time;yy;yy1;yyd;yyd1;yydd;yydd1];
% param=[time;yy;yy;yyd;yyd;yydd;yydd];

options=odeset('RelTol',1e-3,'AbsTol',1e-6);
% T_settle=zeros(1,8);

% [TT,YY]=ode23s(@two_step,[0 time(end)],[yy(1);yyd(1);yy1(1);
    yyd1(1);u_dot(1)],[],param);
[TT,YY]=ode23s(@stage_dyn,time,[yy(1);yyd(1);yy(1);yyd(1)
    ;0;0],options,param,mu_k);

y1_dot_sim=YY(:,2)';
y2_dot_sim=YY(:,4)';
ys_sim=YY(:,5)';
ys_dot_sim=YY(:,6)';




% figure()
% plot(time,yyd*1e6,'b--',time,yyd1*1e6,'g--',TT,ys_dot_sim*1
    e6,'r')
% xlabel('Time (s)')
% ylabel('Velocity ($\mu$m/s)')
```

```
figure()
plot(TT,ys_dot_sim,'r',time,yyd,time,yyd1)
xlabel('Time␣(s)')
ylabel('Velocity␣($\mu$␣m/s)')

figure()
plot(TT,ys_sim)
xlabel('Time␣(s)')
ylabel('Stage␣Position␣($\mu$m)')

figure()
subplot(211), plot(TT,ys_sim)
xlabel('Time␣(s)')
ylabel('Stage␣Position␣($\mu$m)')
subplot(212), plot(TT,ys_dot_sim,'r')
xlabel('Time␣(s)')
ylabel('Velocity␣($\mu$m/s)')
return


% Natural Frequency
w1=188000; % rad/sec
w1_hz=29932; % hz

% Damping Ratio
zeta1=0.1171;

% DC Gain
K_dc=0.1507; % um/V
```

```
V_in=(1/(K_dc*(w1^2)))*(yydd+2*zeta1*w1*yyd+(w1^2)*(yy-0.9*min
    (yy)));
V_in_1=(1/(K_dc*(w1^2)))*(yydd1+2*zeta1*w1*yyd1+(w1^2)*(yy1
    -0.9*min(yy1)));



% A=0.005;
% w=1;
% % ys_d_dot=A*sin(2*pi*w*time);
% ys_d_dot=A*ones(size(time));
% figure()
% plot(time,ys_d_dot,time,ys_dot_sim)
% xlabel('Time (s)')
% ylabel('Stage Velocity (m)')
% legend('Desired','Simulation')

return
y1_dot_sim=YY(:,2)';
y2_dot_sim=YY(:,4)';

% figure()
% plot(time,y1_dot_sim,time,y2_dot_sim,'g--',time,ys_dot_sim,'
    r:')
% legend('y1','y2','ys')
```

```
ii=1;
while abs(xs_dot_sim(ii)) <= abs(0.98*xs_dot_sim(end))
    ii=ii+1;
end

T_settle=[TT(ii) ys_dot_sim(end)]
```

A.4 Matlab Code for Experiments and Measurement

A.4.1 Input Generation

```
clear all
close all
clc

% friction force parameters
mu_k = 0.2; % kinetic friction coefficient
mu_s = 0.3; % static friction coefficient

g  = 9.81; % gravity constant um/s^2

% load variables_all
Mt=0.006;

dt=1/10000000; % Delta T
Freq=500; % Frequency
T=1/Freq; % Period

disp=3; % um

% Asymmetry (FIXED)
```

```
Skew=52;
Kdc=1;

% New trajectory, no linear/1st order constraints
y=TrajFun_5th(Freq, Skew, Kdc, dt);

% This is where I can scale the trajectories
Delta_P=max(y(1,:))-min(y(1,:)); % Maximum change in position

% V input set above
p=(y(1,:)/(Delta_P))*disp;
p=p+((max(p)-min(p))/2);
v=(y(2,:)/(Delta_P))*disp;
a=(y(3,:)/(Delta_P))*disp;
t=y(4,:)-min(y(4,:));
disp_max=max(p)-min(p);

% Pattern the trajectories, end up with repeatvalue+1
tsize=length(t);
repeatvalue=89;
yy=[p repmat(p(2:tsize),1,repeatvalue)];

% yy=[p repmat(p(2:tsize),1,repeatvalue)]-min(p);
yyd=[v repmat(v(2:tsize),1,repeatvalue)];
yydd=[a repmat(a(2:tsize),1,repeatvalue)];
time=linspace(0,(repeatvalue+1)*1/Freq,max(size(yy)));

%  add zeros/constants at the beginning and end of the
   trajectory
```

```
Npre = 60*(1/Freq); Npost = Npre;
tpre  = 0:dt:(Npre-dt);
tpost = 0:dt:(Npost-dt);

yy = [zeros(size(tpre))   yy zeros(size(tpost))];
yyd = [zeros(size(tpre))  yyd zeros(size(tpost))];
yydd = [zeros(size(tpre))  yydd zeros(size(tpost))];

[bb,aa]=butter(2,8000/(1/(2*dt)));
yy_filt=filtfilt(bb,aa,yy);
yyd_filt=filtfilt(bb,aa,yyd);
yydd_filt=filtfilt(bb,aa,yydd);

yy=yy_filt;
yyd=yyd_filt;
yydd=yydd_filt;
t=0:dt:((length(yy)-1)*dt);

% Generate the shifted trajectories
yy1=circshift(yy,round(T/dt/2)*ones(size(yy)));
yyd1=circshift(yyd,round(T/dt/2)*ones(size(yyd)));
yydd1=circshift(yydd,round(T/dt/2)*ones(size(yydd)));
% figure()
% subplot(311), plot(t,yy,t,yy_filt)
% ylabel('$y_d$')
% subplot(312), plot(t,yyd,t,yyd_filt)
% ylabel('$\dot{y}_d$')
% subplot(313), plot(t,yydd,t,yydd_filt)
% ylabel('$\ddot{y}_d$')
```

```
% xlabel('time')
% return

figure()
subplot(311), plot(t,yy)
ylabel('$y_d$')
subplot(312), plot(t,yyd)
ylabel('$\dot{y}_d$')
subplot(313), plot(t,yydd)
ylabel('$\ddot{y}_d$')
xlabel('time')

figure()
plot(t,yy,t,yy1)
xlabel('Time␣(s)')
ylabel('Displacement␣($\mu$m)')
legend('$y_1$','$y_2$')
% return

% Number of points for FFT
% Nfft = 2^19;
Nfft = 2^14;
% Nfft=2048;
tmax =max(t);

% Redefine the time vector in terms of the FFT vector
told=t;
deltt=tmax/Nfft;
t=0:deltt:tmax;
```

```
yd=interp1(told,yy,t);
yd1=interp1(told,yy1,t);

% figure()
% plot(t,yd)
% return

% Define the optimal inverse TF's
K = 1e5; wc =3000; % cutoff frequency
wf = wc*2*pi;
numf=[wf]; denf=[1 wf];
Q1 = tf(K*numf,denf)
R1 = tf(denf,numf)
Qtf = Q1'*Q1;
Rtf = R1'*R1;

load sg11.mat
load sg12.mat
load sg21.mat
load sg22.mat

Ks_Inductive=0.2012; % V/um
Ka=10*8; % Amplifier/Saturation/Filter <UNUSED>

% Output_Data=[f_hz f_rad m_db phase_deg G];
[f_hz_g11,f_rad_g11,m_db_g11,phase_g11,G_g11,angle_g11]=
   Model_Extraction(sg11,Ks_Inductive,Ka);
[f_hz_g12,f_rad_g12,m_db_g12,phase_g12,G_g12,angle_g12]=
   Model_Extraction(sg12,Ks_Inductive,Ka);
```

```
[f_hz_g21,f_rad_g21,m_db_g21,phase_g21,G_g21,angle_g21]=
   Model_Extraction(sg21,Ks_Inductive,Ka);
[f_hz_g22,f_rad_g22,m_db_g22,phase_g22,G_g22,angle_g22]=
   Model_Extraction(sg22,Ks_Inductive,Ka);


% figure()
% subplot(211), semilogx(f_hz_g11,m_db_g11,f_hz_g12,m_db_g12,
   f_hz_g21,m_db_g21,f_hz_g22,m_db_g22)
% xlabel('Frequency (Hz)')
% ylabel('Magnitude (db)')
% axis([min(f_hz_g11) 2500 -100 50])
% subplot(212), semilogx(f_hz_g11,phase_g11,f_hz_g12,phase_g12
   ,f_hz_g21,phase_g21,f_hz_g22,phase_g22)
% xlabel('Frequency (Hz)')
% ylabel('Phase (deg)')
% axis([min(f_hz_g11) 2500 -7000 360])
% legend('$G_{11}$','$G_{12}$','$G_{21}$','$G_{22}$','Location
   ','SW')
figure()
subplot(211), semilogx(f_hz_g11,m_db_g11,f_hz_g22,m_db_g22)
xlabel('Frequency␣(Hz)')
ylabel('Magnitude␣(db)')
axis([min(f_hz_g11) max(f_hz_g11) -100 50])
subplot(212), semilogx(f_hz_g11,phase_g11,f_hz_g22,phase_g22)
xlabel('Frequency␣(Hz)')
ylabel('Phase␣(deg)')
axis([min(f_hz_g11) max(f_hz_g11) min(phase_g11) 360])
legend('$G_{11}$','$G_{22}$','Location','SW')
```

```
% return
%%%%%%%%%%%%%%%%%%%%%%%%%%%%%%%%%%%%
% Step 4 ---  iterative control
%%%%%%%%%%%%%%%%%%%%%%%%%%%%%%%%%%%%

% Takes the FFT of the desired response
ydfft = fftshift(fft(yd));
yd1fft= fftshift(fft(yd1));
% Creates the frequency vector for FFT & Simulation
w = [-Nfft/2:1:(Nfft/2)]*2*pi/max(t);

% Create new double sided frequency vectors
% Adds a zero component to the frequency vector and extends to
    2*max(w)
f_rad_g11=f_rad_g11.';
f_rad_g11=[f_rad_g11 2*max(w)];
f_rad_g11_total=[(-1*fliplr(f_rad_g11)) 0 f_rad_g11];

f_rad_g12=f_rad_g12.';
f_rad_g12=[f_rad_g12 2*max(w)];
f_rad_g12_total=[(-1*fliplr(f_rad_g12)) 0 f_rad_g12];

f_rad_g21=f_rad_g21.';
f_rad_g21=[f_rad_g21 2*max(w)];
f_rad_g21_total=[(-1*fliplr(f_rad_g21)) 0 f_rad_g21];

f_rad_g22=f_rad_g22.';
f_rad_g22=[f_rad_g22 2*max(w)];
f_rad_g22_total=[(-1*fliplr(f_rad_g22)) 0 f_rad_g22];
```

```
% Create the double sided frequency response
% Adds a DC component at w=0;
G_g11=G_g11.';
G_g11=[G_g11 G_g11(end)];
conj_G_g11=conj(G_g11);
G_g11_total=[fliplr(conj_G_g11) abs(G_g11(1)) G_g11];

G_g12=G_g12.';
G_g12=[G_g12 G_g12(end)];
conj_G_g12=conj(G_g12);
G_g12_total=[fliplr(conj_G_g12) abs(G_g12(1)) G_g12];

G_g21=G_g21.';
G_g21=[G_g21 G_g21(end)];
conj_G_g21=conj(G_g21);
G_g21_total=[fliplr(conj_G_g21) abs(G_g21(1)) G_g21];

G_g22=G_g22.';
G_g22=[G_g22 G_g22(end)];
conj_G_g22=conj(G_g22);
G_g22_total=[fliplr(conj_G_g22) abs(G_g22(1)) G_g22];

%  Get Q & R in frequency domain
Q=freqresp(Qtf,w);
R=freqresp(Rtf,w);

Q=reshape(Q,1,length(w));
```

```
R=reshape(R,1,length(w));

% Create the iteration gain vector
% rho=ones(1,length(Q));
for ii=1:length(w)
    if abs(w(ii)/2/pi)>3000
        Q(ii) = 0;
    end
end

% Reshape G_gii_total to the right vector
H11=interp1(f_rad_g11_total,G_g11_total,w);
H12=interp1(f_rad_g12_total,G_g12_total,w);
H21=interp1(f_rad_g21_total,G_g21_total,w);
H22=interp1(f_rad_g22_total,G_g22_total,w);

% Create Full yd Vector
ydfft_Full=[ydfft
         yd1fft];
yfft_Full=0*ydfft_Full;
% Create Empty Input vector
u_fft_Full=0*ydfft_Full;
e_fft_Full=ydfft_Full-yfft_Full;
II=eye(2,2);
% Loop through G to get G_opt at each frequency
for jj=1:length(w)
    G_Full=[H11(jj) H12(jj)
            H21(jj) H22(jj)];
    R_Full=R(jj)*II;
```

```
    Q_Full=Q(jj)*II;
%       G_opt_Full=inv(R_Full+G_Full'*Q_Full*G_Full)*(G_Full'*
   Q_Full);
%       G_opt_Full=inv(G_Full);
    u_fft_Full(:,jj)=inv(R_Full+G_Full'*Q_Full*G_Full)*(G_Full
       '*Q_Full)*ydfft_Full(:,jj);
%   u_fft_Full(:,jj)=G_opt_Full*ydfft_Full(:,jj);

%       u_fft_Full(:,jj)=u_fft_Full(:,jj)+rho(jj)*G_opt_Full*
   e_fft_Full(:,jj);
end

y_fft_Full=[H11.*u_fft_Full(1,:)+H12.*u_fft_Full(2,:);
            H21.*u_fft_Full(1,:)+H22.*u_fft_Full(2,:)];

U_1=real(ifft(ifftshift(u_fft_Full(1,:))));
U_2=real(ifft(ifftshift(u_fft_Full(2,:))));

Y_1=real(ifft(ifftshift(y_fft_Full(1,:))));
Y_2=real(ifft(ifftshift(y_fft_Full(2,:))));

figure()
plot(t,U_1,t,U_2)
title('Inputs')
legend('U1','U2')

figure()
plot(t,Y_1,t,Y_2)
title('Outputs')
```

```
% return
u1=U_1;
u2=U_2;

u1_new=u1;
u2_new=u2;
yd_1_new=Y_1;
yd_2_new=Y_2;
% %
u1_middle=u1(round(90/Freq/deltt):round(120/Freq/deltt));
% yd_1_middle=yd(round(90/Freq/deltt):round(120/Freq/deltt));
% %
u2_middle=u2(round(90/Freq/deltt):round(120/Freq/deltt));
% yd_2_middle=yd(round(90/Freq/deltt):round(120/Freq/deltt));
% %
% u1_new=[u1_middle(1:end-1) u1_middle(1:end-1) u1_middle(1:
    end-1) u1_middle(1:end-1) u1_middle(1:end-1) u1_middle(1:end
    -1) u1_middle(1:end-1)];
% yd_1_new=[0*yd_1_middle(1:end-1) yd_1_middle(1:end-1)
    yd_1_middle(1:end-1) yd_1_middle(1:end-1) yd_1_middle(1:end
    -1) yd_1_middle(1:end-1) 0*yd_1_middle(1:end-1)];
%
%
% u2_new=[u2_middle(1:end-1) u2_middle(1:end-1) u2_middle(1:
    end-1) u2_middle(1:end-1) u2_middle(1:end-1) u2_middle(1:end
    -1) u2_middle(1:end-1)];
% yd_2_new=[0*yd_2_middle(1:end-1) yd_2_middle(1:end-1)
    yd_2_middle(1:end-1) yd_2_middle(1:end-1) yd_2_middle(1:end
    -1) yd_2_middle(1:end-1) 0*yd_2_middle(1:end-1)];
```

```
%
% t_new=0:deltt:(length(u1_new)-1)*deltt;
%
% if  length(t_new)>length(w)
%       LW=length(w);
%       LT=length(t_new);
%       L_Diff=abs(length(t_new)-length(w));
%       u1_new=u1_new(1:end-(L_Diff));
%       u2_new=u2_new(1:end-(L_Diff));
%       yd_1_new=yd_1_new(1:end-(L_Diff));
%       yd_2_new=yd_2_new(1:end-(L_Diff));
%       t_new=t_new(1:end-(L_Diff));
% end
%
% figure()
% plot(t,u1_new,t,u2_new)
% title('new input')
% figure()
% plot(t,yd_1_new,t,yd_2_new)
% title('new yd')
% % return
% u1yd2u2yd2__dual_3um=[u1_new; yd_1_new; u2_new; yd_2_new];
% save u1yd2u2yd2_dual_3um


u1_new=u1_middle;
u2_new=u2_middle;
t_middle=0:deltt:(length(u1_new)-1)*deltt;
```

```
figure()
plot(t_middle,u1_new,t_middle,u2_new)
xlabel(’Time␣(s)’)
ylabel(’Voltage␣(V)’)
legend(’$u_{opt,1}$’,’$u_{opt,2}$’)
ylim([-20 20])
xlim([0.0373 t_middle(end)])
return
t_new=t_middle;
time_200K=0:1/200000:t_new(end);
Voltage_new=interp1(t_new,u1_new,time_200K,’nearest’);
Voltage_new1=interp1(t_new,u2_new,time_200K,’nearest’);

figure()
plot(time_200K,Voltage_new,time_200K,Voltage_new1)

return
figure()
plot(t_new,u1_new,time_200K,Voltage_new,t_new,u2_new,time_200K
   ,Voltage_new1)
xlabel(’Time’)
ylabel(’Input␣Voltage’)
legend(’A1’,’Interp␣for␣DAQ␣A1’,’A2’,’Interp␣for␣DAQ␣A2’)
% return
% figure()
% plot(time_200K,Voltage_new,time_200K,Voltage_new1)
% xlabel(’Time (s)’)
% ylabel(’Voltage (V)’)
% legend(’$V_1(t)$’,’$V_2(t)$’)
```

```
% return
VT=(Voltage_new)/8; % Accounts for Amplifier Pre-Piezo
VT1=(Voltage_new1)/8; % Accounts for Amplifier Pre-Piezo

% VT=VT-min(VT)+2;
% VT1=VT1-min(VT1)+2;

if  max(VT>20) > 0
    disp('STOP')
    return
end
if  min(VT<-20) > 0
    disp('STOP')
    return
end

figure()
plot(time_200K,VT,time_200K,VT1)
xlabel('Time␣(sec)')
ylabel('Scaled␣Voltage␣(V)')
title('␣Output␣Voltage␣to␣be␣Amplified')

figure()
plot(time_200K,VT*8,time_200K,VT1*8)
xlabel('Time␣(sec)')
ylabel('Voltage␣(V)')
title('␣Output␣Voltage')

% return
```

```
figure()
plot(time_200K,VT,time_200K,VT1)
xlabel('Time␣(sec)')
ylabel('Scaled␣Voltage␣(V)')
title('␣Output␣Voltage␣to␣be␣Amplified')
% return
VT=VT(1:end-1);
VT1=VT1(1:end-1);
length(VT)

return
%
outputname='Single_A1_3um_750hz_0_8001pts_all';
% outputname='A1';
VT_Store=VT;

% VT=VT(1:end-1);
format short
% DataName=sprintf('INV_100_%dV_25.txt',V);
DataName=sprintf('%s.txt',outputname);
fid = fopen(char(DataName),'w');
fprintf(fid, '%2.4f\t',VT);
fclose('all');

outputname1='Single_A2_3um_750hz_0_8001pts_all';
% outputname1='A2_test';
VT_Store1=VT1;
% VT1=VT1(1:end-1);
format short
```

```
% DataName=sprintf('INV_100_%dV_25.txt',V);
DataName=sprintf('%s.txt',outputname1);
fid = fopen(char(DataName),'w');
fprintf(fid, '%2.4f\t', VT1);
fclose('all');
```

A.4.2 Measurement Code

```
% Scott Wilcox
% Data Retrieval from .lvm Measurment Files

clear all
close all
clc

% Sensor Constants
Inductive_Sensor_Gain=1/0.2012; % um/V
Amplifier_Gain=10; %V/V

% Data=lvm_import('C:\Users\Scott\Documents\Research\LabView\
    Measurements\11-11\Single 1um 1khz gaintest\
    Raw_Measurements_P1P2IS_2.lvm',2);
% Data=lvm_import('C:\Users\Scott\Documents\Research\LabView\
    Measurements\12-15\Dual Optimal Inverse wc3000 p7A1\
    Raw_Measurements_P1P2IS_1.lvm',2);
Data=lvm_import('C:\Users\Scott\Documents\Research\LabView\
    Measurements\Raw_Measurements_P1P2IS_17.lvm',2);
% Piezo_Data=lvm_import('Data\PiezoPosition_2.lvm',2);
% Piezo_Data=lvm_import('C:\Users\Scott\Documents\Research\
    LabView\Measurements\10-23\SINGLE\PiezoPosition.lvm',2);
% Piezo_Data=lvm_import('C:\Users\Scott\Documents\Research\
```

```
    LabView\Measurements\10-29\SINGLE 5um 1khz\PiezoPosition_5.
    lvm',2);

Piezo_1_Disp_Meas_V=Data.Segment1.data(:,2);
Piezo_2_Disp_Meas_V=Data.Segment1.data(:,5);
U1_Disp_Meas_V=Data.Segment1.data(:,4);
Stage_Disp_Meas_V=Data.Segment1.data(:,3);

Time=(0:1/50000:(length(Piezo_1_Disp_Meas_V)-1)/50000)';

figure()
plot(Time,U1_Disp_Meas_V),
xlabel('Time')
ylabel('Voltage')
title('Inputs␣Raw␣Voltage␣-␣Pre-␣Amplifier')
legend('$u_{opt,1}$')

figure()
plot(Time,Piezo_1_Disp_Meas_V)
xlabel('Time')
ylabel('Voltage')
title('$\dot{y}_1$␣Raw␣Voltage')

figure()
plot(Time,Piezo_2_Disp_Meas_V)
xlabel('Time')
ylabel('Voltage')
title('$\dot{y}_2$␣Raw␣Voltage')
```

```
figure()
plot(Time,Stage_Disp_Meas_V)
xlabel('Time')
ylabel('Voltage')
title('Stage␣Raw␣Voltage')
% return
% Convert from Volts to um
U1_Disp_Meas=U1_Disp_Meas_V*8;
Stage_Disp_Meas=Stage_Disp_Meas_V*Inductive_Sensor_Gain;
Piezo_1_Disp_Meas=Piezo_1_Disp_Meas_V*Inductive_Sensor_Gain/
   Amplifier_Gain;
Piezo_2_Disp_Meas=Piezo_2_Disp_Meas_V*Inductive_Sensor_Gain/
   Amplifier_Gain;
Piezo_1_Disp_Meas=Piezo_1_Disp_Meas-nanmean(Piezo_1_Disp_Meas)
   ;
Piezo_2_Disp_Meas=Piezo_2_Disp_Meas-nanmean(Piezo_2_Disp_Meas)
   ;

figure()
plot(Time,U1_Disp_Meas)
xlabel('Time')
ylabel('Voltage')
title('Inputs␣Real␣Voltage')
legend('$u_{opt,1}$')

figure()
plot(Time,Piezo_1_Disp_Meas,Time,Piezo_2_Disp_Meas)
xlabel('Time')
ylabel('Displacement␣($\mu$m)')
```

```
title('Actuators')
legend('$\dot{y}_1$','$\dot{y}_2$')

figure()
plot(Time,Stage_Disp_Meas)
xlabel('Time')
ylabel('Displacement␣($\mu$m)')
title('Stage')
legend('$\dot{y}_s')

Piezo_1_Disp_Meas=Piezo_1_Disp_Meas-nanmean(Piezo_1_Disp_Meas)
   ;
Piezo_2_Disp_Meas=Piezo_2_Disp_Meas-nanmean(Piezo_2_Disp_Meas)
   ;
% Stage_Disp_Meas=Stage_Disp_Meas-nanmean(Stage_Disp_Meas);

[b,a]=butter(2,(5000/25000));
Piezo_1_Disp_Meas=filtfilt(b,a,Piezo_1_Disp_Meas);
Piezo_2_Disp_Meas=filtfilt(b,a,Piezo_2_Disp_Meas);

figure()
plot(Time,Piezo_1_Disp_Meas,Time,Piezo_2_Disp_Meas)
xlabel('Time')
ylabel('Displacement␣($\mu$m)')
title('Actuators')
legend('$\dot{y}_1$','$\dot{y}_2$')

% Define the filter to get the velocity profiles
wc=100000*2*pi;
```

```
Af=[-wc];
Bf=[wc];
Cf=1;
Df=0;
lpf2=ss(Af,Bf,Cf,Df);

y1=Piezo_1_Disp_Meas;
y2=lsim(lpf2,y1,Time,y1(1));
y3=lsim(lpf2,y2,Time,y2(1));
Error=y3;
Piezo_1_Vel_Est=wc*(y2-y3);
Piezo_1_Acc_Est=wc^2*(y1-2*y2+y3);

y1=Piezo_2_Disp_Meas;
y2=lsim(lpf2,y1,Time,y1(1));
y3=lsim(lpf2,y2,Time,y2(1));
Error=y3;
Piezo_2_Vel_Est=wc*(y2-y3);
Piezo_2_Acc_Est=wc^2*(y1-2*y2+y3);

y1=Stage_Disp_Meas;
y2=lsim(lpf2,y1,Time,y1(1));
y3=lsim(lpf2,y2,Time,y2(1));
Error=y3;
Stage_Vel_Est=wc*(y2-y3);
Stage_Acc_Est=wc^2*(y1-2*y2+y3);


% These will contain the start and end times for the data that
```

```
    is in the
% measurment range of the sensor.
Stage_Disp_Start=[];
Stage_Disp_End=[];
```

Appendix B

LABVIEW CODE

B.1 Signal Generation

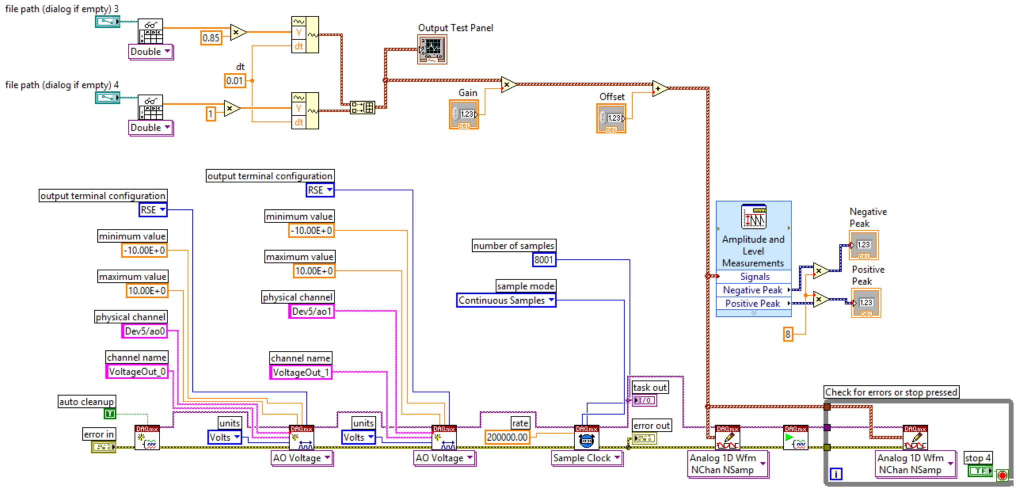

Figure B.1: LabVIEW VI for generating the input signals for the piezos.

B.2 Signal Measurement

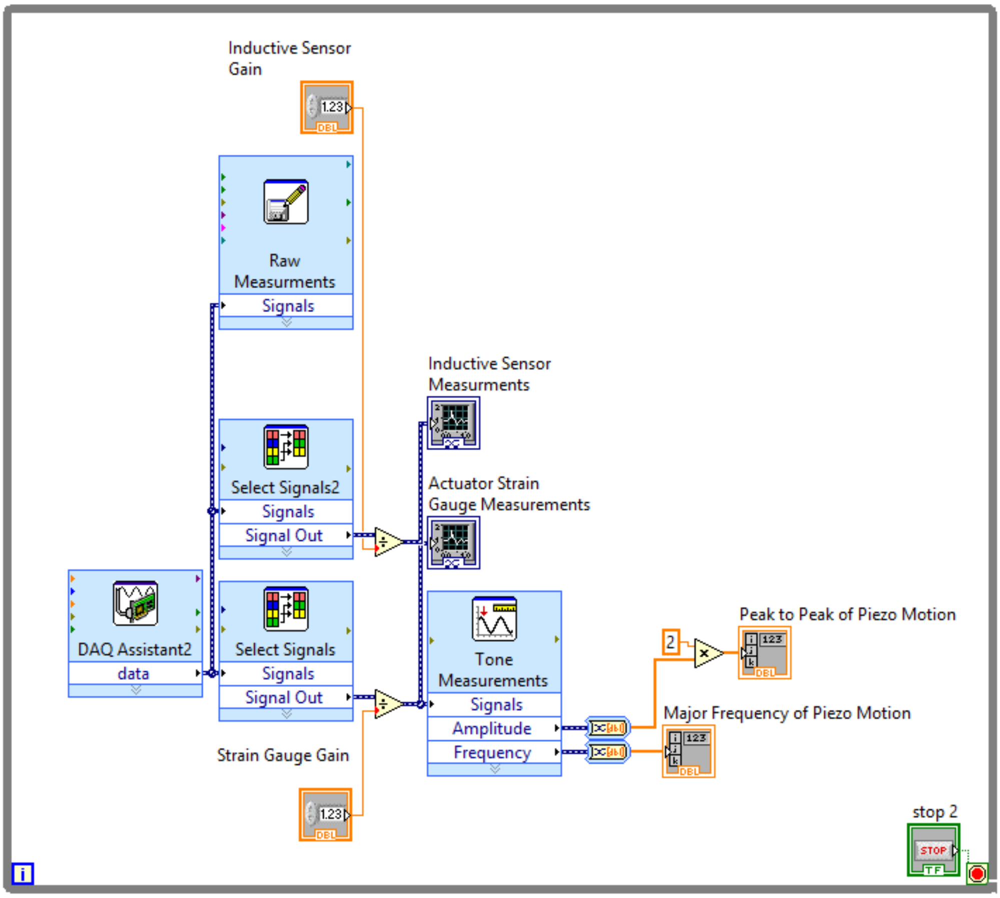

Figure B.2: LabVIEW VI for measuring the output signals from the inductive sensors and the input signals to the piezos.

Appendix C

STEPPER DESIGNS

C.1 First Iteration of Stepper System

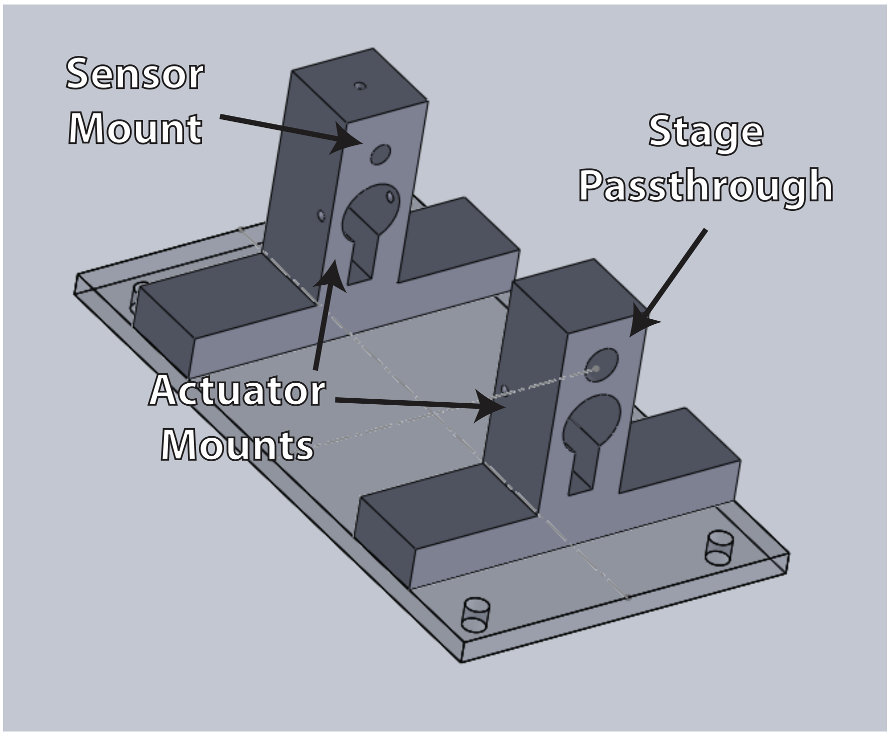

Figure C.1: CAD representation of the first stepper design.

The first stepper design consisted of two towers each containing one piezo. One tower had a passthrough to allow the stage to move freely over the actuators while the other tower held the inductive sensor to measure the stage motion.

This design ended up having two major disadvantages. The first being, it was difficult to find a position that would allow the inductive sensor to measure the motion of a the piezo-tip y_i $(i = 1, 2)$. The second (and much more major issue) was that the towers ended up having a significant amount of vibration due to the actuation of the piezos (Fig. C.2).

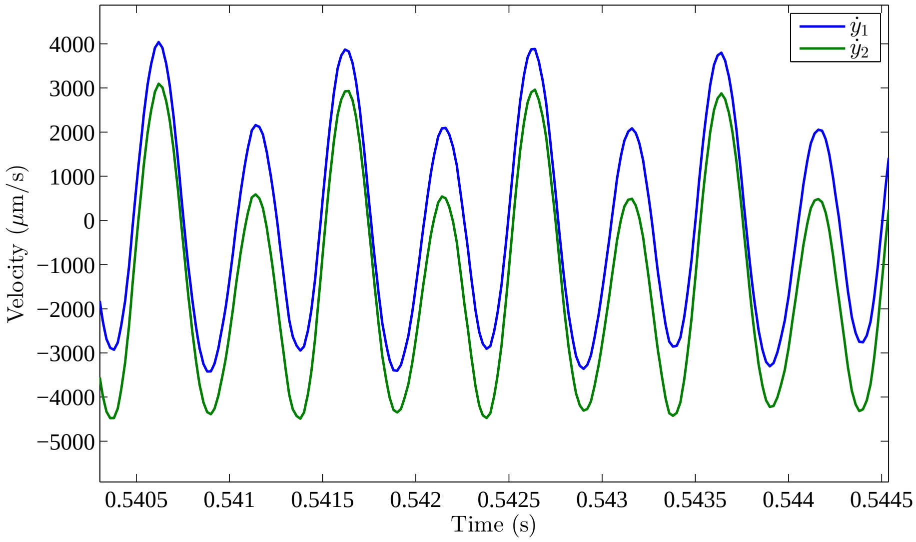

Figure C.2: Oscillations in Piezo-tip velocity $\dot{y}_i$ $(i = 1, 2)$ for piezos mounted in the first structure. These oscillations are induced by the structure vibrating and are at the driving frequency f_{dw}.

C.2 Second Iteration of Stepper System

With the oscillations in the first design, a second iteration of the stepper design was setup for experiments. This design was constructed out of ABS plastic and created in a 3D printer. The new design can be seen in Fig. C.3. The results from the second stepper system are shown in C.5 and C.6

With the second structure, the oscillations, when compared between the dual mode and single mode inputs, are reduced by $\approx$ 35%. However, the tracking was not ideal and the achieved velocity was slower than expected. This led to the design of the third iteration of the stepper system, constructed from aluminum.

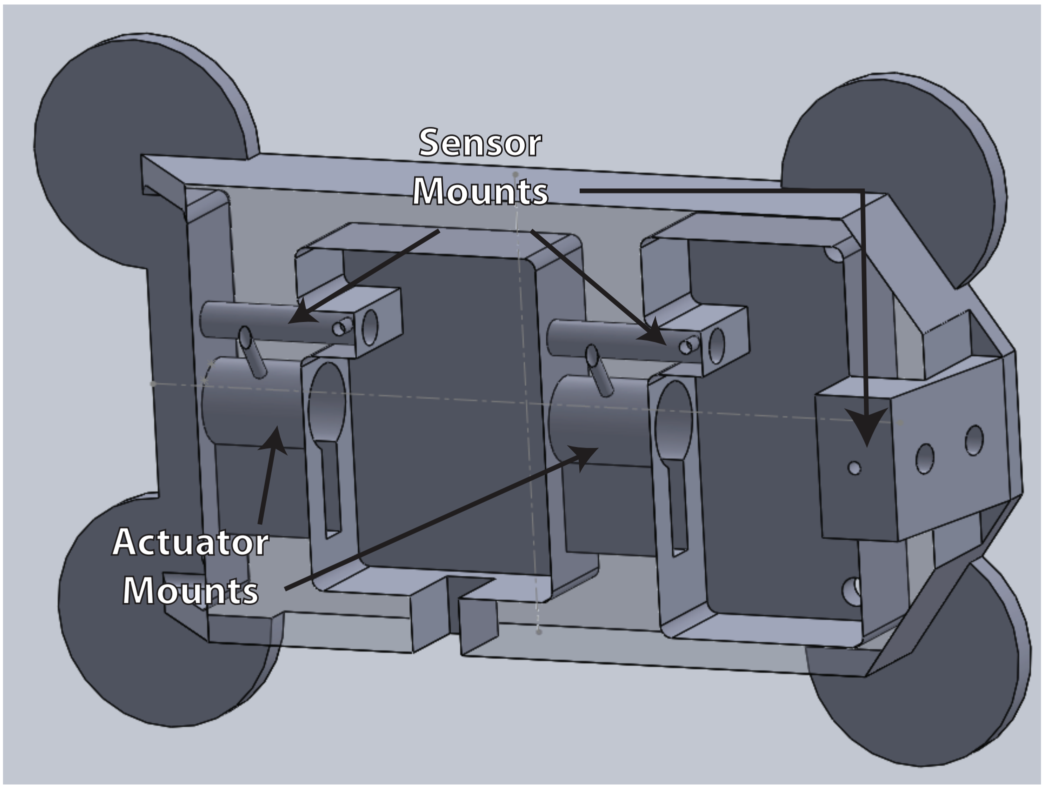

Figure C.3: CAD representation of the second stepper system design.

C.2.1 Effect of Stage Leveling

With the stage velocity $\dot{y}_s$ slower than anticipated, external effects were investigated. If the stepper system and stage are not level, the dynamics of the stage can be altered. By introducing a non-level stage, the dynamics become

$$\ddot{y}_s(t) = -\mu_k \frac{P_1}{M}\ sign\left[\dot{y}_s(t) - \dot{y}_1(t)\right] - \mu_k \frac{P_2}{M}\ sign\left[\dot{y}_s(t) - \dot{y}_2(t)\right] - (\mathbf{M_t g})\mathbf{sin}(\theta_{\mathbf{tilt}}) \qquad \text{(C.1)}$$

where θ_{tilt} is the angle at which the stage is tilted.

In Fig. C.9, it is shown that introducing small angles into the stepper system can change the steady-state velocity of the stage $\dot{y}_s$. To verify this experimentally, small amounts of mass were added to the isolation platform to introduce a small angle perturbation. The results of this experiment are shown in Fig. C.10 which shows that as the added mass was

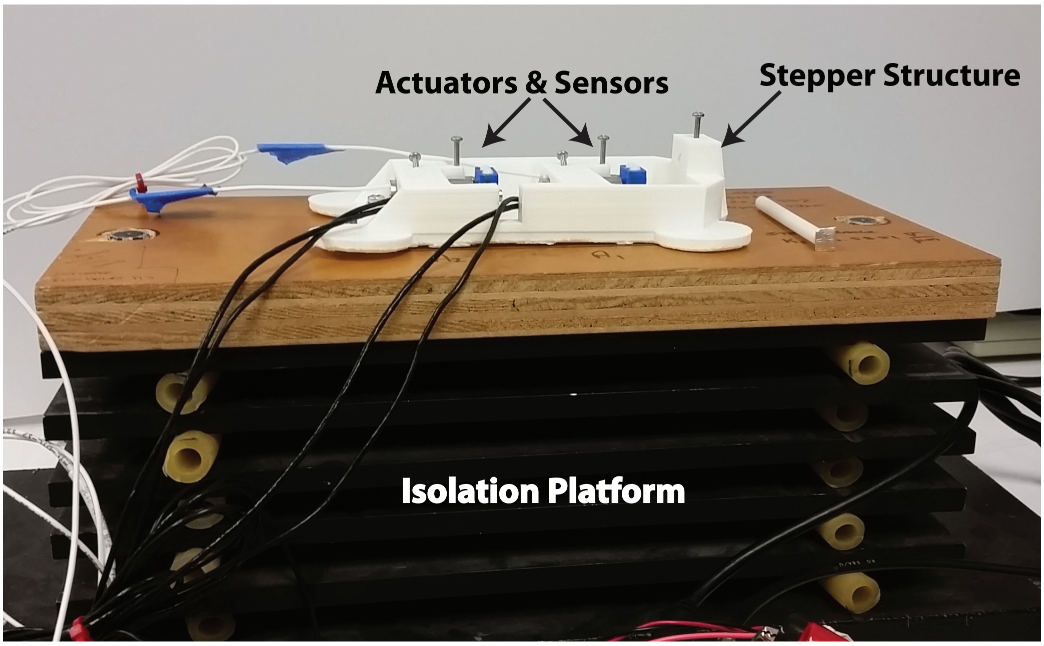

Figure C.4: Experimental Setup with the second design

increased, the steady-state velocity of the stepper slowly increased.

C.2.2 Wear on Sphere Surfaces

With the third stepper design (aluminum structure, see Chapter 5), the first set of dual mode results had oscillations that were larger than desired. An example of these results are shown in Fig. C.11. Looking at the direction of the oscillations, the oscillations always tended towards the motion of the second piezo $\dot{y}_2$. Therefore, it was hypothesized that the spheres were worn on the second piezo contact points.

By replacing the contact points on the second actuator, the resulting oscillations improved significantly and are presented at the end of Chapter 5.

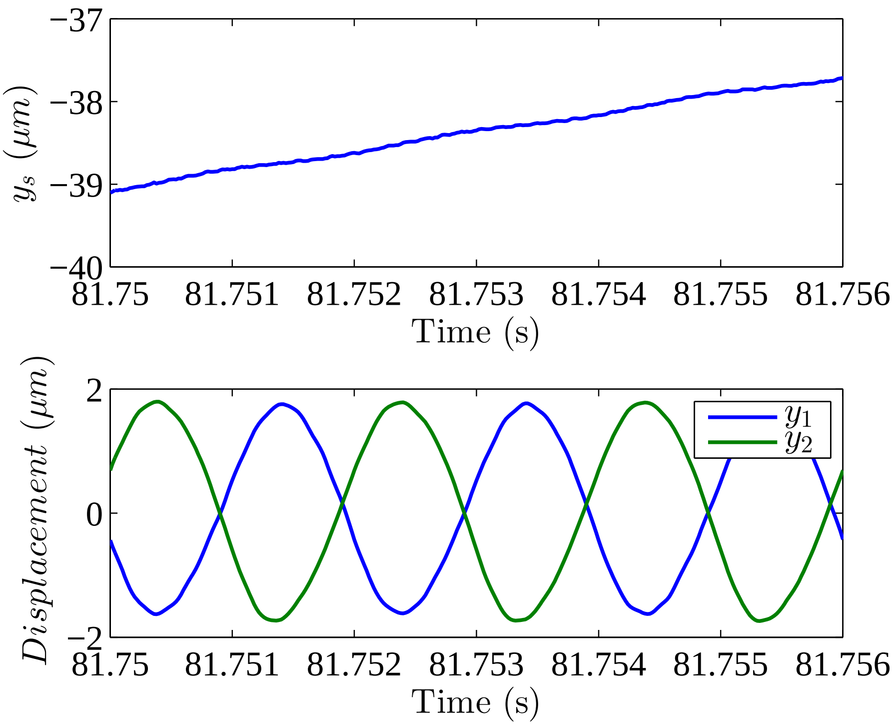

Figure C.5: (Top) The resulting stage motion y_s due to the periodic inputs $u_{opt,i}$ $(i = 1, 2)$ to the piezos. (Bottom) The resulting piezo-tip displacements due to the periodic inputs $u_{opt,i}$ $(i = 1, 2)$ to the piezos.

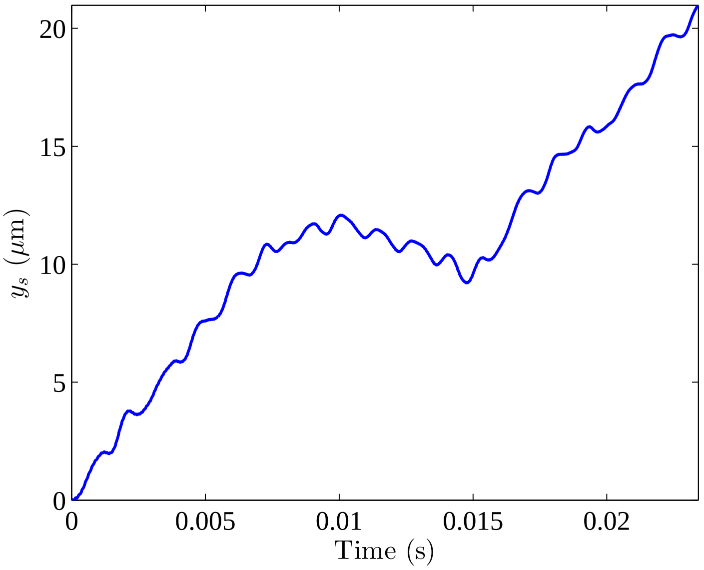

Figure C.6: Motion of the stage y_s due to the single mode inputs shown in Fig. 4.10. Note, when compared to Fig. 4.9, the oscillations are more pronounced.

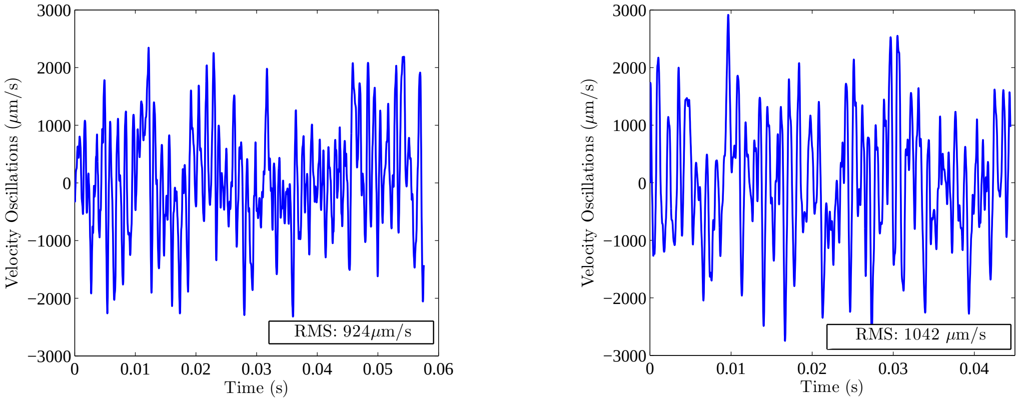

Figure C.7: Oscillations in the steady-state stage velocity $\dot{y}_s$ in the dual mode ($\phi = 1/2$).

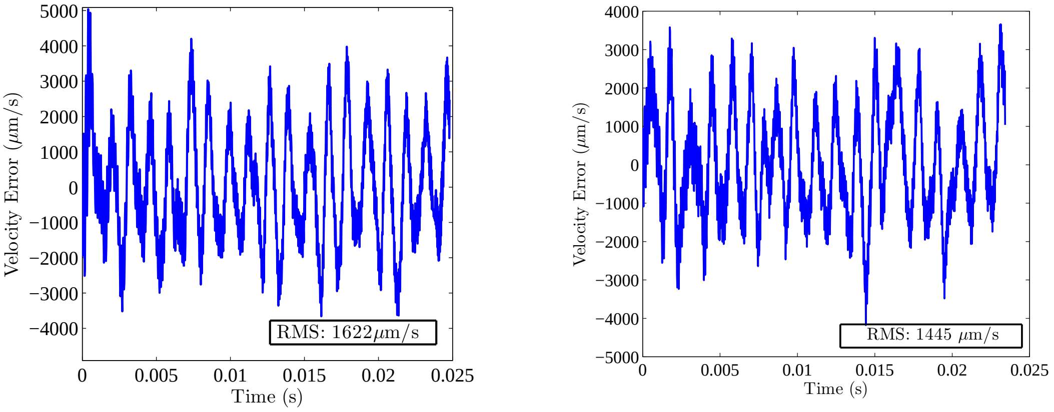

Figure C.8: Oscillations in the steady-state stage velocity $\dot{y}_s$ in the single mode ($\phi = 0$).

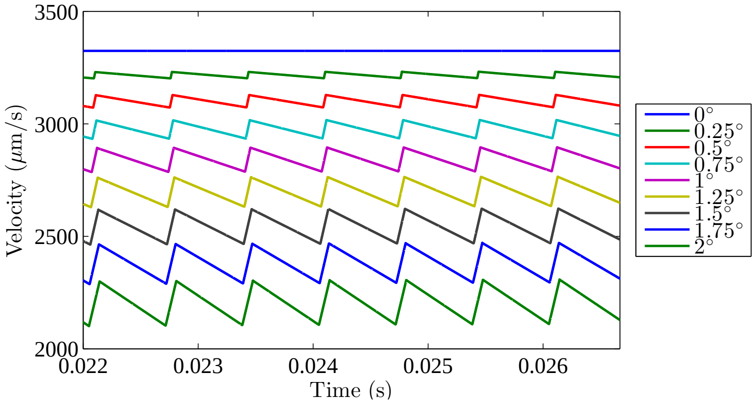

Figure C.9: Simulation results of introducing an small angle perturbation θ_{tilt} to the stage. As the angle is increased, the steady-state velocity of the stage $\dot{y}_s$ decrease as well as sees an increase in oscillation magnitude.

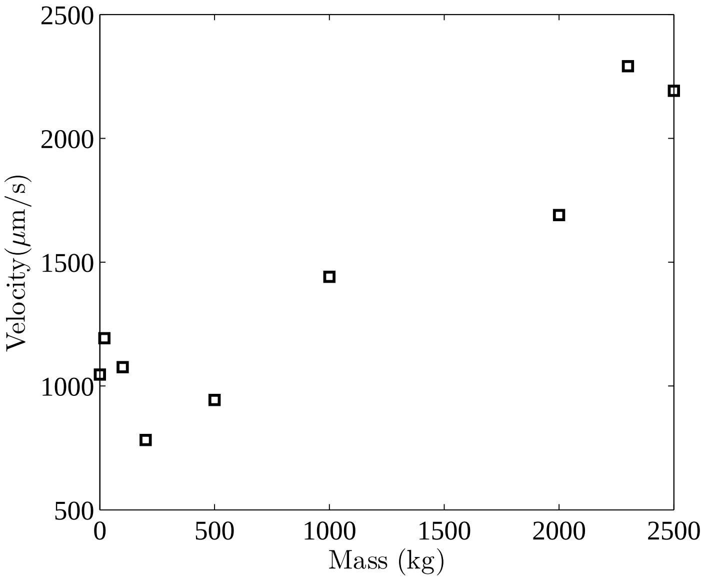

Figure C.10: Masses were used $(0-2500kg)$ to change the angle of the platform (θ_{tilt}) and thus change the angle of the stage. As the mass was increased (resulting in an decrease in the tilting angle θ_{tilt}), the stage velocity $\dot{y}_s$ increased.

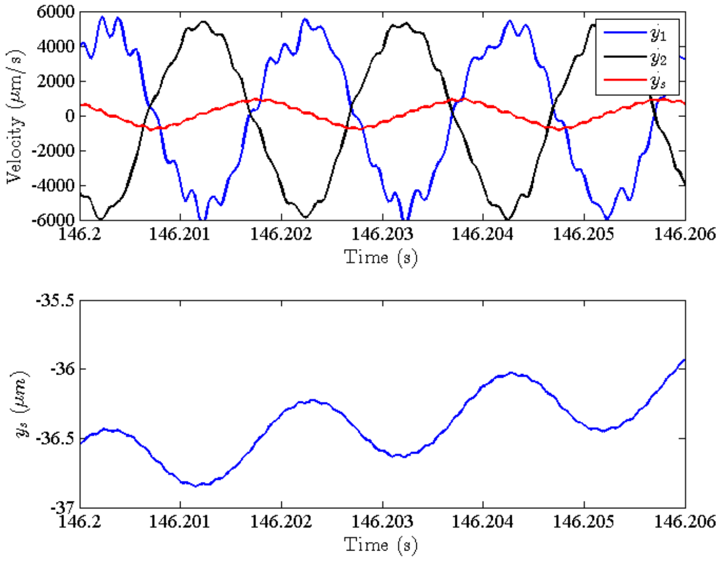

Figure C.11: Oscillations in the stage velocity $\dot{y}_s$ with the stepper in dual mode. The oscillations tend towards the second actuator velocity $\dot{y}_2$ which led to the hypothesis that the contact points were worn.

Appendix D

OPTIMAL INVERSE

D.1 *Dual Mode Optimal Inverse*

When generating the optimal inverse $u_{opt,i}$ ($i = 1, 2$), pre and post actuation was used to ensure transient behavior did not effect the inputs sent to the piezos. This was done by introducing a pre-actuation trajectory of zero displacement as well as a post-actuation trajectory of zero displacement. An example of this can be seen in Fig. D.1.

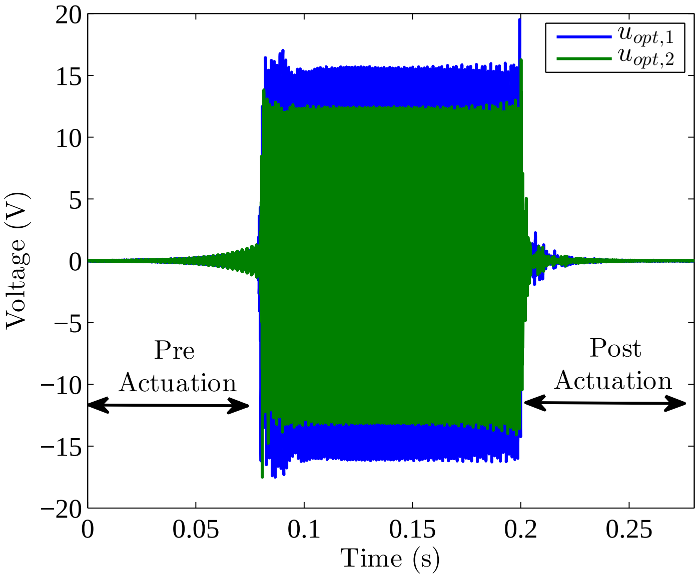

Figure D.1: Inputs generated using the optimal inverse (4.1) for the dual input mode including the pre and post actuation.

D.2 *Single Mode Optimal Inverse*

When generating the optimal inverse $u_{opt,i}$ ($i = 1, 2$), pre and post actuation was used to ensure transient behavior did not effect the inputs sent to the piezos. This was done by introducing a pre-actuation trajectory of zero displacement as well as a post-actuation trajectory of zero displacement. An example of this can be seen in Fig. D.2.

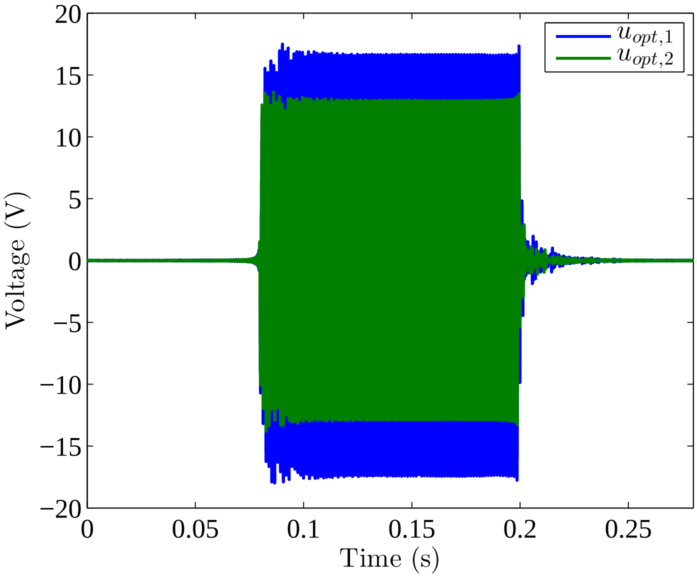

Figure D.2: Inputs generated using the optimal inverse (4.1) for the single input mode including the pre and post actuation.

VITA

Scott Wilcox is a Ph.D. student in the Department of Mechanical Engineering at the University of Washington, Seattle, Washington, USA.

He received his B.S. degree in Mechanical Engineering from the University of Washington in 2009. He received his M.S. degree in Mechanical Engineering from the University of Washington in 2011. In 2013, he was awarded the Teaching Assistant Award from the Mechanical Engineering Department. He received the Best Student Paper Award at the 2013 ASME Dynamic Systems and Control Conference. In 2014, he was a Research Scientist Intern at Amazon.com working on the Prime Air drone delivery service. He will be returning to the team as a Hardware Development Engineer in 2015.

Contact: `wilcos@uw.edu`